Modelling the photochemical properties of conjugated oligomers; understanding their application as photocatalysts

Pierre Guiglion

Primary Supervisor: Dr. Martijn Zwijnenburg

Secondary supervisor: Prof. Furio Corà

University College London

Department of Chemistry

Thesis submitted for the degree of Doctor of Philosophy

February 2017

I, Pierre Guiglion, confirm that the work presented in this thesis is my own. Where information has been derived from other sources, I confirm that this has been indicated in the thesis.

Pierre Guiglion
February 2017

Abstract

In this Ph.D. project, I introduce a new computational methodology, based on (time-dependent) Density Functional Theory ((TD-)DFT), in order to determine if a molecule, here a conjugated oligomer, has the required photochemical properties to drive thermodynamically one or both water splitting half-reactions. This new approach takes electronic excitations into account rather than only relying on a static HOMO-LUMO description of the electronic structure, and therefore provides a more rigorous prediction of relevant thermodynamic potentials than ground-state DFT alone; it offers a relatively quick way of consistently screening for new photocatalysts for solar-driven water splitting.

Using this computational framework, I investigate the optical properties of oligo(*p*-phenylene), one of the simplest conjugated oligomers imaginable, as well as its thermodynamic potentials, relevant to the splitting of water into molecular hydrogen and oxygen. I then validate the methodology by confronting it to experimental data, before applying it to a wide range of conjugated oligomers, to determine whether or not they could be promising photocatalysts for water splitting, be it for the production of molecular hydrogen, oxygen gas, or both. In particular, I expose the reasons for the experimental lack of overall water splitting usually observed, and more particularly, the inability of many materials to oxidise water.

Aside from purely photocatalytic considerations, I also discuss the optical properties of those oligomers and polymers, as they are tightly linked to their photocatalytic performance, with a particular emphasis on *p*-phenylene. I consistently study its three main isomers in order to shed some light into the relationship between their molecular structures and absorption/fluorescence spectra, and find the origin of the dramatic difference in the features exhibited by the latter, using a single computational approach, which, to the best of my knowledge, has never been done before.

Table of contents

List of abbreviations

2PPE: two-photon photoelectron spectroscopy

B3LYP: hybrid XC functional, which incorporates 20% of HF-like exchange

BHLYP: hybrid XC functional, which incorporates 50% of HF-like exchange

CAM-B3LYP: long range corrected B3LYP using the Coulomb-Attenuating Method (19% HF-like exchange at short range and 65% at long range)

CB: conduction band

CC: coupled-cluster

CC2: approximate coupled-clusters singles-and-doubles method

CGF: contracted Gaussian function

CMP: conjugated microporous polymer

CN: carbon nitride

COSMO: conductor-like screening model

CT: charge-transfer

CTF: covalent triazine framework

CV: cyclic voltammetry

Cz: carbazole moiety

DBT: dibenzothiophene

DBTsulf: dibenzothiophene sulfone

DCM: dichloromethane

DEA: diethylamine

def2-SVP: split-valence plus polarisation

def2-TZVP: triple zeta split-valence plus polarisation

DFT: density functional theory

DFT-D3 or **DFT+D:** DFT plus Grimme's dispersion correction

DZP: double zeta plus polarisation

EA: electron affinity

EA*: excited state electron affinity

EBE: exciton binding energy

ESSE: excited state stabilisation energy

Fl: fluorene moiety

GGA: generalised gradient approximation

GS: ground state

GSDE: ground state destabilisation energy

GTO: Gaussian-type orbitals

H/C: hydrogen-to-carbon ratio

HER: hydrogen evolution rate

HF: Hartree-Fock

HOMO: highest occupied molecular orbital

IP: ionisation potential

IP*: excited state ionisation potential

KS: Kohn-Sham

LCAO: linear combination of atomic orbitals

LDA: local density approximation

LUMO: lowest unoccupied molecular orbital

LVEE: lowest vertical excitation energy

OER: oxygen evolution rate

P3HT: poly(3-hexylthiophene)

PBC: periodic boundary conditions

PES: photoelectron spectroscopy

PF: polyfluorene

PFur: polyfuran

Ph: phenylene moiety

PPP: poly(*p*-phenylene), or more generally any *p*-phenylene chain including oligomers

PPV: poly(phenylene vinylene)

PPyra: polypyrazine

PPyri: polypyridine

PPyrim: polypyrimidine

PPyrr: polypyrrole

PT: polythiophene

S0: singlet ground state

S1: singlet first excited state

SCE: standard calomel electrode

SCF: self-consistent field

SEA: sacrificial electron acceptor

SED: sacrificial electron donor

SHE: standard hydrogen electrode

SHEAP: SHE absolute potential

STO: Slater-type orbitals

TD-DFT: time-dependent DFT

TDA: Tamm-Dancoff approximation

TEA: triethylamine

UV: ultraviolet

UV-Vis: ultraviolet-visible spectroscopy

VB: valence band

WS: water splitting

XC: exchange-correlation

List of figures

List of tables

List of publications

The following publications result from the work done during my Ph.D. project:

1. Guiglion P.; Butchosa C.; Zwijnenburg M. A., "Polymeric watersplitting photocatalysts; a computational perspective on the water oxidation conundrum", *J. Mat. Chem. A* **2014**, *2*, 11996-12004.

2. Butchosa C.; Guiglion P.; Zwijnenburg M. A., "Carbon Nitride Photocatalysts for Water Splitting: A Computational Perspective", *J. Phys. Chem. C* **2014**, *118*, 24833-2484.

3. Guiglion P.; Zwijnenburg M. A., "Contrasting the optical properties of the different isomers of oligophenylene", *Phys. Chem. Chem. Phys.* **2015**, *17*, 17854-17863.

4. Sprick R.S.; Jiang J.-X.; Bonillo B.; Ren S.; Ratvijitvech T.; Guiglion P.; Zwijnenburg M. A.; Adams D. J.; Cooper A. I., "Tunable Organic Photocatalysts for Visible Light-Driven Hydrogen Evolution", *J. Am. Chem. Soc.* **2015**, *137*, 3265-3270.

5. Sprick R. S.; Bonillo B.; Clowes R.; Guiglion P.; Brownbill N.J.; Slater B.J.; Blanc F.; Zwijnenburg M. A.; Adams D. J.; Cooper A. I., "Visible Light-Driven Water Splitting Using Planarized Conjugated Polymer Photocatalysts", *Angew. Chem. Int. Ed.* **2016**, *55*, 1792-1796.

6. Guiglion P.; Berardo E.; Butchosa C.; Wobbe M. C. C.; Zwijnenburg M. A., "Modelling materials for solar fuel synthesis by artificial photosynthesis; predicting the optical, electronic and redox properties of photocatalysts", *J. Phys.: Condens. Matter* **2016**, *28*, 074001.

7. Guiglion P.; Butchosa C.; Zwijnenburg M. A., "Polymer Photocatalysts for Water Splitting: Insights from Computational Modeling", *Macromol. Chem. Phys.* **2016**, *217*, 344-353.

8. Guiglion P.; Monti A.; Zwijnenburg M. A., "Validating a Density Functional Theory Approach for Predicting the Redox Potentials Associated with Charge Carriers and Excitons in Polymeric Photocatalysts", *J. Phys. Chem. C* **2017**, 121, 1498-1506.

9. Meier C. B.; Sprick R. S.; Monti A.; Guiglion P.; Zwijnenburg M. A.; Cooper A. I., "Structure-property relationships for covalent triazine-based frameworks: the effect of spacer length on photocatalytic hydrogen evolution from water", *s*ubmitted to *Polymer,* **2017**, DOI: 10.1016/j.polymer.2017.04.017

CHAPTER 1:

Introduction

In this chapter, I will introduce the concept of photocatalytic water splitting, and specify the constraints that this process imposes on a photocatalyst. I will then describe the general properties of inorganic photocatalysts, as well as those of conjugated polymers, and their advantages over inorganic semiconductors. Next, I will introduce and present the different polymeric materials studied throughout this project. Finally, I will sum up the main challenges and objectives of my project.

Some of the content of this chapter has been taken from part of the following published work:

Guiglion P.; Butchosa C.; Zwijnenburg M. A., "Polymeric watersplitting photocatalysts; a computational perspective on the water oxidation conundrum", *J. Mat. Chem. A* **2014**, *2*, 11996-12004.

1.1. Photocatalytic water splitting

Photocatalytic water splitting refers to the splitting of water into molecular oxygen (O_2) and hydrogen (H_2) using natural or artificial light. Solar-driven water splitting holds particular interest since it uses clean, renewable, inexpensive and readily available resources to produce molecular hydrogen, one of the key starting materials used in the chemical industry, as well as a potential automotive fuel (fuel cells).

Currently, fossil fuels amount to about 90% of energy worldwide, leading to the emission of greenhouse gases including carbon dioxide, which is a top-priority global issue. There are several alternative energy sources, among which hydrogen, an advantageous fuel due to its availability from various sustainable sources, high energy yield, environmental friendliness, and high storage capacity.[1] However, using hydrogen as an alternative source of energy has some drawbacks, e.g. the extra costs associated with compressing it before storage, the dangers associated with the concurrent production of hydrogen and oxygen gases and the costs of separating those two gases, and the limited infrastructure available for the widespread distribution of hydrogen fuel.

Theoretically, only water, solar energy (renewable, free, and virtually unlimited) and a photocatalyst are needed, as described below. In practice however, the use of co-catalysts and/or sacrificial reagents is almost always required experimentally.

In a naive picture, when light irradiates a photocatalytic molecule or particle, a photon of sufficient energy can promote an electron from the highest occupied molecular orbital (HOMO, in the case of molecules, or top of the valence band (VB) in the case of materials) to the lowest unoccupied orbital (LUMO for molecules, or bottom of the conduction band (CB) for materials). It creates an electron-hole pair that can either recombine or take part in the water splitting half-reactions (see Figure 1.1).

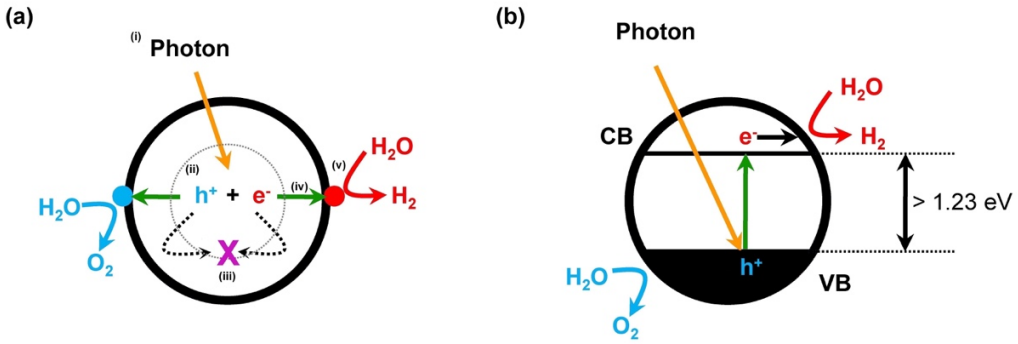

Figure 1.1: (a) Main processes in photocatalytic water splitting[2]: (i) photon absorption, (ii) electron-hole pair creation, (iii) undesirable recombination, (iv) migration to reaction sites, and (v) surface redox reactions. (b) Excitation of an electron from a material's valence band (VB) to its conduction band (CB).

Note: this scheme shows a naive picture of the photocatalytic processes involved in water splitting; in reality, as will be discussed in Chapter 3, it is much more complicated.

The electron (e^-) and the hole (h^+) respectively take part in two half-reactions: the reduction of protons into molecular hydrogen, and the oxidation of water into molecular oxygen.

$$2H^+_{(aq)} + 2e^- \rightleftarrows H_{2(g)} \qquad \text{(A)}$$

$$O_{2(g)} + 4H^+_{(aq)} + 4e^- \rightleftarrows 2H_2O_{(l)} \qquad \text{(B)}$$

In practice however, as will be discussed later, the use of co-catalysts (typically platinum, palladium or ruthenium) is needed to aid the reduction of protons into molecular hydrogen and the oxidation of water into molecular oxygen, at the photocatalytically active sites. In addition, since it is notoriously difficult to achieve overall water splitting (*i.e.* drive both the hydrogen and oxygen producing reactions concurrently), one usually focusses on only one of these half-reactions; sacrificial electron donors (SED, *i.e.* hole acceptors that will be oxidised instead of water, such as methanol or triethylamine) are typically used to trigger hydrogen production, and sacrificial electron acceptors (SEA, *i.e.* hole donors, that will be reduced instead of protons, *e.g.* Ag^+ or Ce^{4+} salts) to trigger the oxygen production.

The experimental potentials of proton reduction and water oxidation relative to the standard hydrogen electrode are respectively 0 eV and -1.23 eV under standard conditions. For these reactions to occur successfully, there are several constraints

on the photocatalyst. The conjugated polymer must have: (i) a fundamental gap[3] larger than 1.23 eV, which corresponds to the difference in energy between the proton reduction and water oxidation potentials, (ii) an optical gap[3] smaller than approximately 3.5 eV, so that it can absorb visible photons (at wavelengths larger than approximately 350 nm), and (iii) HOMO/LUMO levels (in the molecular case, or VB/CB positions when considering materials) that "straddle" the potentials of proton reduction and water oxidation (see Figure 1.15).

Additionally, the photocatalyst should allow for facile exciton dissociation and electron-hole separation, have a low overpotential for the desired redox reactions, and be stable under illumination and redox conditions.

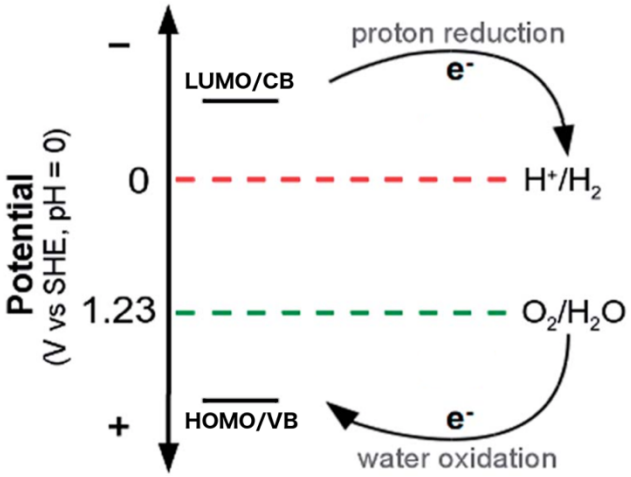

Figure 1.2: Scheme outlining the required properties that a photocatalyst must have to drive water splitting.

In other words, the energy of the electron-donating excited state must be above the hydrogen-producing half-reaction potential, while the electron-accepting ground state must be below the oxygen-producing half-reaction potential. More details about the photocatalyst's optical gap, fundamental gap, and standard reduction potentials (intuitively similar to the HOMO/LUMO and VB/CB notions) will be given in the following chapters, especially in Chapter 3.

Experimentally, the electrolysis of pure water also requires excess energy in the form of overpotential to overcome various activation barriers; without this, the splitting would occur very slowly or not at all. This is in part due to the limited self-ionisation,

and the very low conductivity of pure water. The required overpotential for the oxidation of water is expected to be slightly larger than the overpotential for proton reduction, due to the fact that the former reaction involves the transfer of 4 electrons through several steps, whereas the latter is a more straightforward, 2-electron reaction. In practice, a promising photocatalyst will have a LUMO/CB level at least 0.5-0.7V above (more negative) than the proton reduction level, and a HOMO/VB level at least 0.8-1.2V below (more positive) than the water oxidation level.

1.2. Inorganic photocatalysts

Inorganic photocatalysts are semiconductor materials, i.e. which electrical conductivity lies between that of an insulator and of a conductor. Their conducting properties can be altered *via* the controlled introduction of small amounts of impurities or defects (doping), making them either electron-rich (n-type) or electron-poor (p-type), or by applying an electrical field, or light. Their introduction revolutionised the field of electronics in the late 1940s (e.g. diodes, transistors), and more recently, they found applications an photocatalysts.

To achieve water splitting, inorganic photocatalysts such as metal oxides, sulphides, and nitrides have been employed, in which high crystallinity and small particle size are desired to minimize the recombination of photo-generated electrons and holes.[1] Indeed, following the discovery by Fujishima, Honda and co-workers, in 1969, that a TiO_2 photoanode (that uses a combination of light and electrical bias) could catalyse the splitting of water,[4] the search for water splitting catalysts focussed primarily upon inorganic systems[5-7] (*e.g.* besides TiO_2; $Zn_{1.44}GeN_{2.08}O_{0.38}$ (ref. [8]) and TaON[9]). Many of those systems show promising alignment of their conduction and valence bands with respect to the two water-splitting half-reactions (see Figure 1.3).

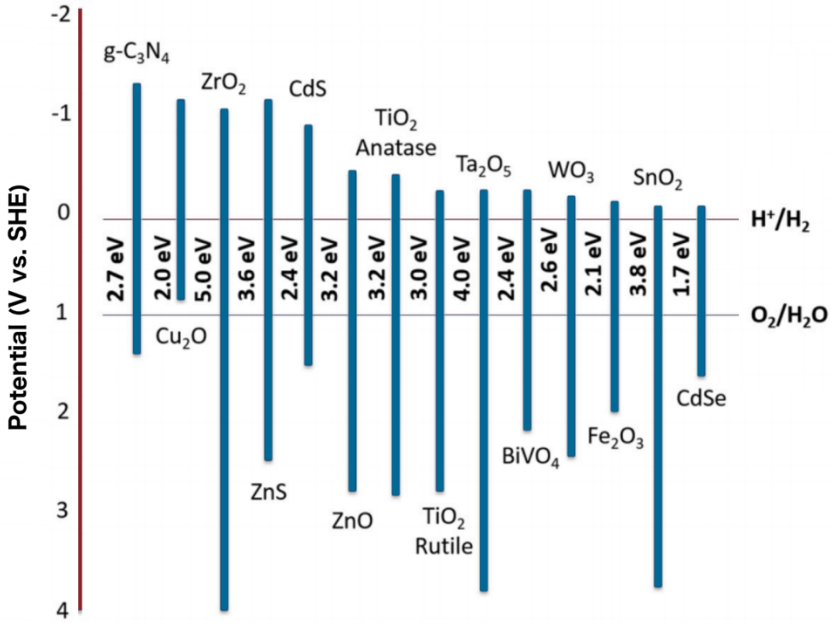

Figure 1.3: Alignment of the band positions of various semiconductors with respect to the redox potentials of water splitting. Figure adapted from Ong et al. work.[10]

To minimize the band gap in order to absorb visible light, while maintaining suitable band positions, several methods have been attempted. Several possible dopants have been studied by first principles computations. For instance, doping with cations of elements such as V,[11] Mn,[12] Fe,[12] and Co,[13] or with anions of C,[14] N[15-16], P,[17], and S,[17] as well as co-doping strategies have been studied by Density Functional Theory (DFT) for TiO_2. Similar investigations have also been carried out for other photocatalysts, e.g. ZnO,[18-19] WO_3,[20] and $SrTiO_3$.[21] Anion doping or co-doping have been shown to reduce the band gap, sometimes significantly (although anion doping into oxides is challenging in practice), while cation doping exhibits very limited band gap reduction.

One of the main strengths of inorganic photocatalysts is their typically low exciton binding energies, and the possibility to achieve high charge carrier mobility, allowing for facile bulk charge separation and transport.

1.3. Conjugated oligomers and polymers

Organic conjugated polymers and oligomers are mostly semiconductors, where conductivity is achieved by the movement of charge carriers: π electrons, and holes (absence of electrons). In such polymers, the molecular backbone is constituted of sp^2 hybridised atoms, with alternating single and multiple bonds. The electrons are assumed to be delocalised and to relatively freely "circulate" *via* the overlap of π orbitals.

In most organic semiconductors, the intermolecular forces are too weak to form 3D crystal lattices, which is fundamentally different to crystalline inorganic semiconductors, where the individual LUMOs and HOMOs form a CB and a VB throughout the material. Consequently, in conjugated oligomers and polymers, the molecular LUMOs and HOMOs do not interact strongly enough to form a CB and VB. Thus charge transport proceeds by hopping between localised states, rather than transport within a band. This means that charge carrier mobility in organic and polymeric semiconductors are generally low compared to inorganic semiconductors. Also, charge separation is more difficult in organic semiconductors due to the low dielectric constant. In many inorganic semiconductors, photon absorption produces a free electron and a free hole, whereas the excited electron is bound to the hole (at room temperature) in organic semiconductors.

Conjugated polymers are a fascinating class of materials. They are lightweight and can absorb light. Their main advantages over inorganic semiconductors are their flexibility and transparency, since they are usually amorphous (which gives them great potential for new display technologies[22]), ease of manufacture (e.g. roll printing on large surfaces), disposability, environmental friendliness (based on earth-abundant elements), and low cost. Moreover, conjugated polymers offer a diverse synthetic modularity, which allows their electronic and structural properties to be tailored without doping, although doping can be a viable strategy. They can be produced over a continuous range of monomer compositions, thus achieving systematic control over physical properties. Organic conjugated polymers

thus offer the long-term vista of solution-processable photocatalysts that can be optimised through exploiting the unrivalled synthetic versatility offered by organic chemistry.

Those materials are found in a wide variety of applications, ranging from photocatalysis to organic light-emitting diodes, organic solar cells, and supercapacitors. In this project, the focus will be on their application as photocatalysts for solar water splitting.

Organic semiconductors have received much attention since 1985, when Yanagida and co-workers[23] demonstrated that an organic conjugated polymer, poly(*p*-phenylene), could successfully catalyse the proton reduction half-reaction (see section 1.1, reaction (A)) under ultraviolet light, like many inorganic semiconductors reported before, greatly widening the scope of possible photocatalysts. However, until recently, the progress of research into polymeric water splitting catalysts was very slow compared with that of their inorganic analogues, possibly due to perceived stability issues. This all changed in 2008 with the discovery by Antonietti and co-workers[24] that carbon nitride polymers could act as a photocatalyst for both the proton reduction and water oxidation half-reactions (see next section), although, until very recently[25-26], not concurrently. Since this report, there has been a steady stream of publications on polymer systems for photocatalytic water splitting, including (doped) carbon nitrides,[27-34] poly(azomethine),[35] polyimides,[36] and polymeric disulfides.[37]

1.3.1. Linear conjugated polymers

This project will mainly focus on linear conjugated polymers. Specifically, I will first investigate the optical properties and the water splitting potential of poly(p-phenylene) (PPP, see Figure 1.1) and other related polymers. PPP, also known as poly(1,4-phenylene), is recognised as a useful high-performance polymer due to its thermal and chemical stability and its electrical and optoelectronic properties; it is used in light-emitting devices[38-39] and was one of the first polymers to be reported

to catalyse the reduction of protons into molecular hydrogen, under ultraviolet light irradiation.[23, 40]

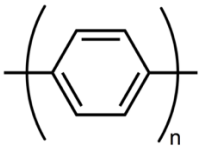

Figure 1.4: Molecular structure of PPP.

Other simple linear conjugated polymers can be created by replacing carbon atoms by heteroatoms in the aromatic ring of PPP. I will focus on some nitrogen, oxygen, and sulphur-containing polymers (see Figure 1.2) that are widely described in the literature, for applications in photocatalysis, but also in organic photovoltaic or display technologies.

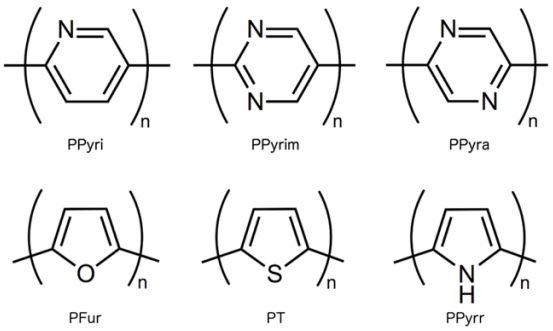

Figure 1.5: Molecular structures of polypyridine (PPyri), polypyrimidine (PPyrim), polypyrazine (PPyra), polyfuran (PFur), polythiophene (PT) and polypyrrole (PPyrr).

Most molecular chains presented above are not planar. For example, in the case of PPP, two consecutive phenylene building blocks form a dihedral angle of approximately 30 to 40 degrees, in its electronic ground state, according to DFT calculations. Some others, however, are overall flatter, since they comprise fewer hydrogen atoms on their aromatic rings, hence decreasing the steric hindrance and favouring planarity (*e.g.* some pyrimidine and pyrazine polymers).

In addition, in Chapter 5, I will study the effect of purposefully[41] planarising and rigidifying some phenylene-containing linear chains. In the case of PPP, rigidity and planarity can be increased by introducing a phenylene linker between every other phenylene unit, resulting in the creation of fluorene motifs (see Figure 1.3 for the structure of polyfluorene). In this project, fluorene-*co*-phenylene chains (hereafter

referred to as *Fl-Ph*), as well as other fluorene-type copolymers (obtained by planarisation *via* the introduction of other linkers, such as heteroatoms, *e.g.* sulphur, or functional groups, *e.g.* amino or sulfone) will be investigated (see Figure 1.4 for the 3D structures of selected "planarised" oligomers, and Figure 1.5 for details about the chosen nomenclature).

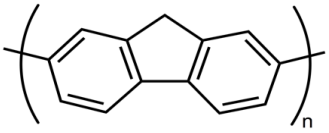

Figure 1.6: Molecular structure of polyfluorene (PF).

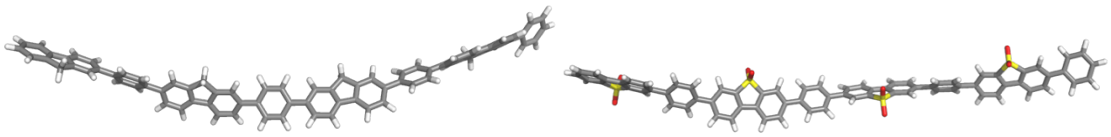

Figure 1.7: B3LYP optimised ground state structures of Fl-Ph-12 (left side) and DBTsulf-Ph-12 (right side), both containing 12 phenylene moiety equivalents.

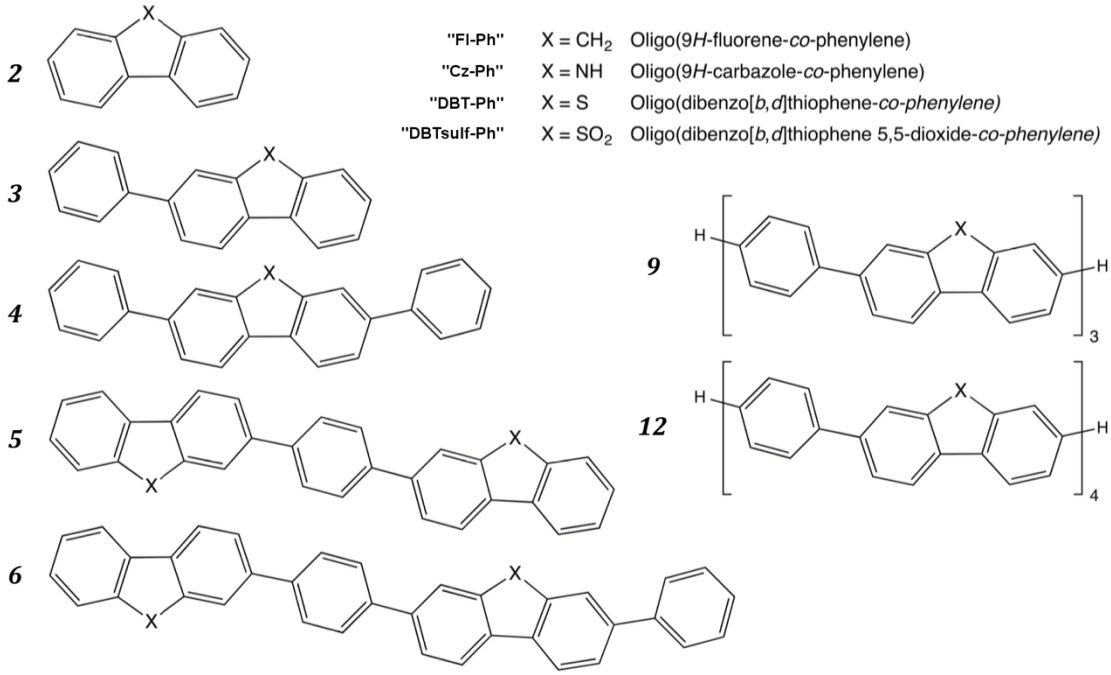

Figure 1.8: Structures of the planarised fluorene-type oligomers studied. For simplicity, the oligomers or polymers corresponding to X = CH_2, NH, S and SO_2 will be referred to as Fl-Ph, Cz-Ph, DBT-Ph and DBTsulf-Ph respectively. The numbers in bold correspond to the number of phenylene moiety equivalents.

1.3.2. Carbon nitride materials

Aside from simple linear conjugated polymers, I will also introduce some larger linear or 2D polymeric materials based on carbon nitride. Carbon nitrides, with general formula $(C_3N_3H)_n$ were first reported by Berzelius in 1830, and named *melon* (see Figure 1.6) a few years later by von Liebig, in 1834.[42] Since then, many related materials have been synthesised, including melem (see Figure 1.6) and high molecular weight polymers.

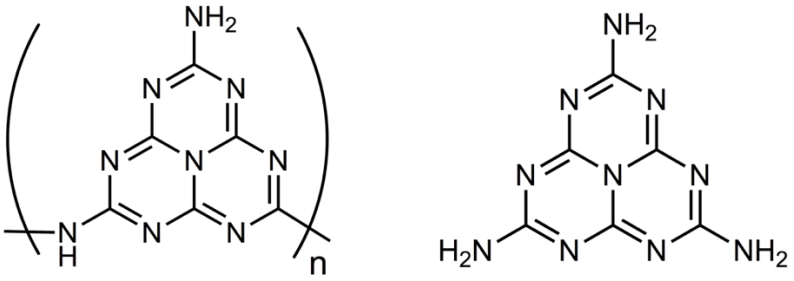

Figure 1.9: Molecular structures of melon (left side) and melem (right side).

This class of materials sparked a surge of interest in the late 2000s, when Antonietti and co-workers[24] reported that carbon nitride polymers could act as photocatalysts, under certain conditions, for the reduction of protons and the oxidation of water. Since then, a steady stream of publications have appeared, recently culminating in the report of two extremely promising carbon nitride materials[25-26] that can catalyse the overall splitting of water.

However, the exact structure of carbon nitride is still poorly understood. While the structures of low-molecular-weight carbon nitride were elucidated (relatively recently[43]), it is not the case for their polymeric counterparts. Those high-molecular versions of carbon nitride, structurally very complex, might be based on triazine or heptazine motifs (see Figure 1.7), linked together in various proportions through -NH- bridges to form linear chains, through single 3-coordinated nitrogen atoms to form flakes with a structure resembling graphite (graphitic carbon nitride, or g-CN) or a mix of the two[44] (see Figure 5.16 in Chapter 5). Moreover, high-molecular-weight carbon nitride is notoriously difficult to characterise; it is often amorphous

or poorly crystallised, and adsorbs water, making characterisation *via* X-ray diffraction and elemental H/C content analysis, respectively, very challenging.

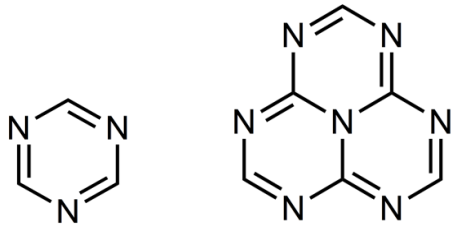

Figure 1.10: Molecular structures of triazine (left side) and heptazine, or tri-s-triazine (right side).

Since the exact atomic structure of the amorphous/semi-crystalline carbon nitride samples used in water splitting are poorly known, calculations are hence performed on cluster models representative of different possible material structures. Carbon nitride oligomers are modelled as single molecular clusters (as opposed to periodic materials), as are the PPP oligomers presented in the previous section. Such clusters are made of linear arrangements of either triazine or heptazine motifs (*i.e.* fragments of melon in the latter case, see Figure 1.8), or built as single, relatively small flakes of graphitic carbon nitride (see Figure 1.9).

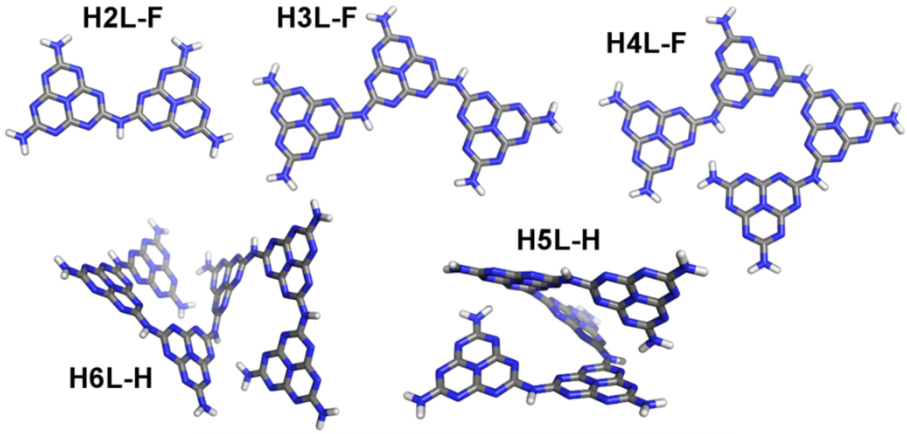

Figure 1.11: DFT optimised 3D structures of selected linear heptazine chains.[44] F or H refer to the "flat" or "helical" shape of the structures.

Figure 1.12: DFT optimised 3D structures of selected graphitic carbon nitride "flakes" composed of heptazine motifs.[44]

The validity of such models was jointly assessed in previous work from the Zwijnenburg group by Butchosa and co-workers, [44] who used a TD-DFT-based approach to predict the optical properties (absorption spectra and absorption onsets) of carbon nitride oligomeric clusters, before comparing them to experimental data. Our group's effort to investigate optical properties in order to shed some light on those materials' molecular structure was motivated by the observation[24] that, during polymer synthesis, changing the temperature (and thus, the final structure of the polymer) affects UV-Vis absorption spectra. Overall, experimental results have been successfully reproduced, which suggests the validity of those models, except for graphitic triazine-based frameworks, whose result discrepancy has been attributed to the presence of nitrogen vacancies in the experimental samples.[44]

1.3.3. Conjugated Microporous Polymers

Conjugated microporous polymers (CMPs) are a fascinating class of materials. They combine the features and properties of both microporous materials (high porosity and surface area) and conjugated polymers (light absorption, photoluminescence, photocatalysis). CMPs present very valuable features: their pore size and gas sorption properties can be tuned, and their fluorescence energy and optical gap can be varied to a large extent by statistical copolymerization[45]. Several types of CMPs, including phenylene[45-50], pyrene[45, 51] (see Figure 1.10), and carbon nitride based

materials[32, 37, 52], have been successfully synthesised, and have been shown to exhibit visible light absorption and fluorescence properties.

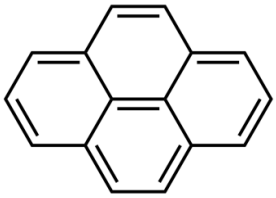

Figure 1.13: Molecular structure of pyrene.

Phenylene- and pyrene-based CMPs are mainly synthesised *via* metal-catalysed coupling reactions (Yamamoto[53], Sonogashira-Hagihara[54], or Suzuki[55]), using only one (the resulting material is a homopolymer) or several distinct monomers (copolymer). In this project, the CMPs of interest will be modelled as ring clusters, comprising several "corners" or vertices, consisting of phenylene or pyrene moieties, attached together through phenylene bridges or "linkers". The monomers used for synthesis typically consist of *1,2,4,5*-tetrabromobenzene and *1,3,6,8*-tetrabromopyrene for the two possible vertex types, and of *1,4*-benzenediboronic acid for the linkers[45, 51] (see Figure 1.11). They yield a wide range of CMPs (phenylene homopolymers or pyrene-phenylene copolymers) with *ortho*- or *para*-substituted phenylene units, and *1,3*- or *1,8*-substituted pyrene units. Those materials are typically amorphous. Because they can comprise small rings, dendrimers, or extended three-dimensional networks, characterising them can be challenging, hence the need to take such structural features (strained rings) into account in the models.

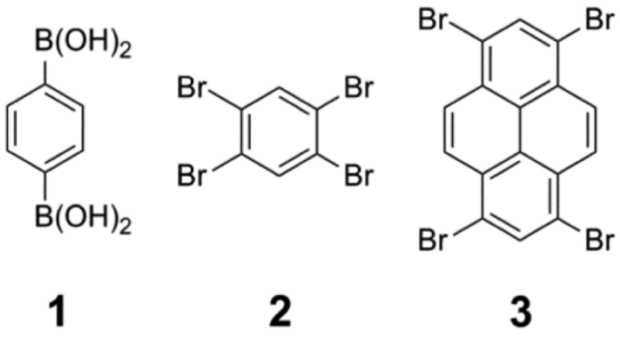

*Figure 1.14: Monomer structures: 1,4-benzenediboronic acid (**1**), 1,2,4,5-tetrabromobenzene (**2**) and 1,3,6,8-tetrabromopyrene (**3**).*

In line with the pyrene models used in M. A. Zwijnenburg's study[51], and in order to be consistent with the monomers used during synthesis, phenylene and pyrene-phenylene CMPs will be modelled as clusters of ring-sizes 4 to 6 (containing respectively 4 to 6 phenylene or pyrene vertices, and 4 to 6 phenylene linkers). Two different isomers will be taken into account (referred to as "short" when phenylene and pyrene corners are linked through the *1,2* and *1,3* positions, respectively, and "long" when phenylene and pyrene corners are linked through the *1,3* and *1,8* positions, respectively, see Figure 1.12). Additionally, across a range of possible conformers, the ones with lowest energy will be considered. The cluster models will therefore be either entirely composed of phenylene units, or in the case of pyrene-phenylene, comprise 50% phenylene (all linkers) and 50% pyrene (all vertices).

Previous research by M. A. Zwijnenburg[51] showed that pyrene oligomers and polymers display in practice a much smaller absorption and fluorescence shift with chain length than other conjugated polymers such as *para*- and *ortho*-polyphenylenes. In later investigations, Zwijnenburg and co-workers[56] rationalised the difference in absorption and fluorescence spectra, between insoluble pyrene CMPs and their linear or branched soluble counterparts, by the presence of strained closed rings in the network. This allows one to link the absorption and fluorescence spectra of polymers with information about their underlying molecular topology, and justifies our group's choice to model those CMPs as ring clusters.

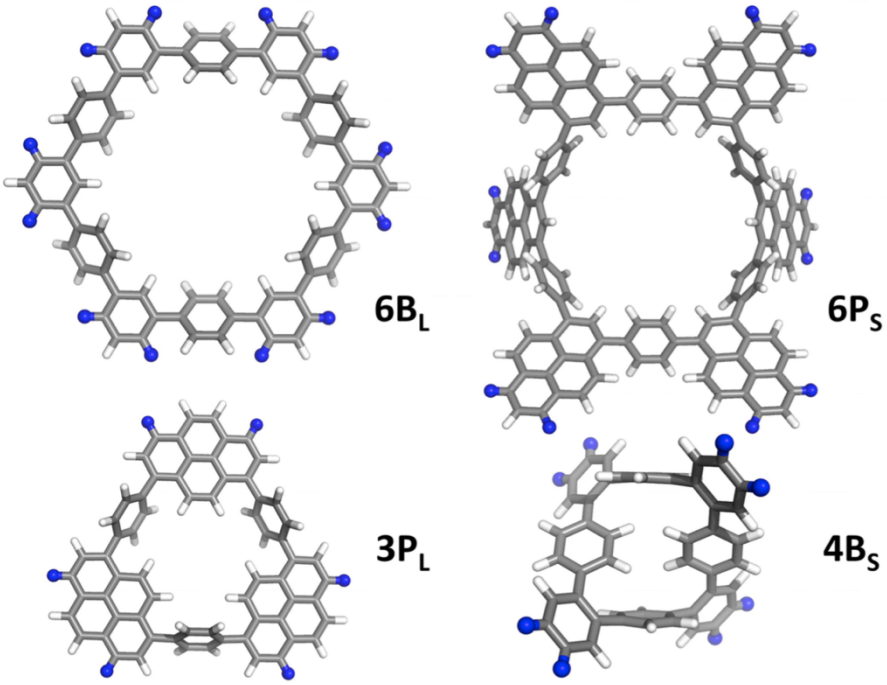

Figure 1.15: DFT optimised 3D structures of the lowest-energy conformers for selected ring clusters. Atoms represented as blue spheres indicate where the rings would connect to the rest of the amorphous CMP network. "B" stands for phenylene vertices, "P" for pyrene vertices. The "L" and "S" subscripts respectively indicate long and short orientation of the vertices.

Another type of related materials, halfway between CMPs and carbon nitrides, will also be studied: covalent triazine frameworks (CTFs). CTFs are particularly relevant to water splitting thanks to their unique properties, as they combine typically high surface areas, being microporous, and promising photochemical properties[29, 57-58], being fluorescent. Moreover, like many other polymers, they possess a high synthetic versatility, as their chain length, molecular weight, pore size and chemical structure can be tuned to achieve target (photocatalytic) properties. Besides ring-containing CTFs, already well described in the literature (*e.g.* CTF-0, CTF-1, and CTF-2)[59-60] other planar CTF clusters will be modelled (see Figure 1.13), built with alternating triazine and phenylene motifs, in a dendrimeric fashion.

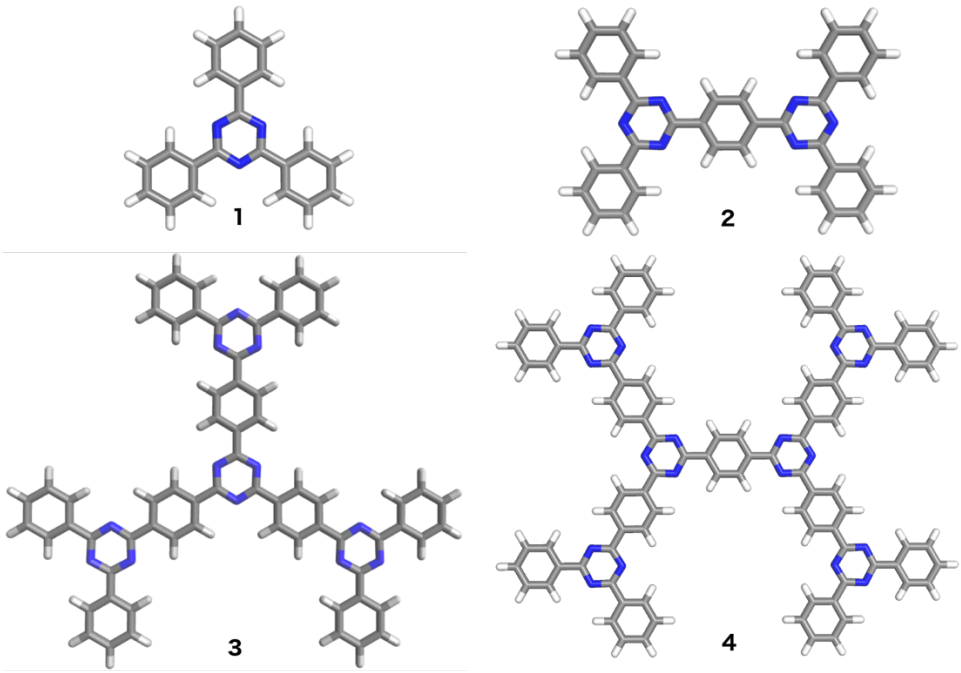

*Figure 1.16: DFT optimised 3D structures of selected CTF clusters: TP3 (**1**), PT2P4 (**2**), TP3T3P6 (**3**) and PT2P4T4P8 (**4**). The nomenclature reflects the dendrimeric nature of the molecules: T and P stand for triazine and phenylene, respectively.*

1.4. Objectives of this Ph.D. project

This project focusses on the application of quantum chemical methods to model excited state processes in conjugated oligomers and polymers. It aims at understanding and optimising those properties of conjugated polymers that underlie their use in solar cells and as photocatalysts for renewable hydrogen and oxygen production, by photocatalytic water splitting.

The main goal of this Ph.D. project is to develop a robust computational methodology to calculate target properties of polymeric photocatalysts, and then use this methodology to screen for promising candidate photocatalysts for water splitting, *i.e.* either find which materials are theoretically the most adequate, or eliminate the ones that are predicted to be ineffective. Those predictions will be confronted to experimental data from the literature, and to the experimental results of our close collaborators at the University of Liverpool (the group of Prof. Andy Cooper[61]).

By combining theoretical calculations using (time-dependent) Density Functional Theory[62-64] and other excited-state methods, with spectroscopic and catalytic experiments carried out by our collaborators, one can explore the relationship between the structure and properties of conjugated polymers. The use of theoretical methods to predict the optical properties of conjugated polymers will enable us to extract information unattainable by experiment alone, and to suggest new polymers for experimental screening. Indeed, the use of a computational approach is mainly motivated by the fact the materials of interest are relatively straightforward to synthesise, although the same does not necessarily hold for the precursors, but notoriously challenging to characterise. Indeed, the properties of polymers synthesised in different batches may vary, which, coupled to delicate characterisation, can result in a lack of meaningful and repeatable results.

In the next chapter, I will lay the theoretical foundations by introducing (TD-)DFT and all other methods or frameworks used. In Chapter 3, I will describe the

computational method used throughout this project, and apply it to poly(p-phenylene). In Chapter 4, I will validate this methodology by comparing the yielded results to experimental data, before applying it, in Chapter 5, to a wide range of polymeric systems, and examining their relative photocatalytic performances. Then, in Chapter 6, I will come back to our original polymer, PPP, and discuss the origin of the dramatic difference in optical properties by exploring the structure of its different isomers. Finally, Chapter 7 will summarise my results and findings, and offer a perspective on the use of theoretical tools to model the use of polymeric materials for photocatalytic water splitting.

1.5. References

1. Jafari, T.; Moharreri, E.; Amin, A.; Miao, R.; Song, W.; Suib, S., "Photocatalytic Water Splitting—The Untamed Dream: A Review of Recent Advances", *Molecules* **2016**, *21*, 900.
2. Payne, D. J. http://payneresearch.org/research/photo-electrochemical-pec-water-splitting/.
3. Brédas, J.-L., "Mind the gap!", *Materials Horizons* **2014**, *1*, 17-19.
4. Fujishima, A.; Honda, K.; Kikuchi, S., "Photosensitized electrolytic oxidation on semiconducting n-type TiO2 electrode", *Kogyo Kagaku Zasshi* **1969**, *72*, 108-113.
5. Kudo, A.; Miseki, Y., "Heterogeneous photocatalyst materials for water splitting", *Chemical Society Reviews* **2009**, *38*, 253-278.
6. Maeda, K.; Domen, K., "Photocatalytic Water Splitting: Recent Progress and Future Challenges", *The Journal of Physical Chemistry Letters* **2010**, *1*, 2655-2661.
7. Hisatomi, T.; Kubota, J.; Domen, K., "Recent advances in semiconductors for photocatalytic and photoelectrochemical water splitting", *Chemical Society Reviews* **2014**,
8. Lee, Y.; Terashima, H.; Shimodaira, Y.; Teramura, K.; Hara, M.; Kobayashi, H.; Domen, K.; Yashima, M., "Zinc Germanium Oxynitride as a Photocatalyst for Overall Water Splitting under Visible Light", *The Journal of Physical Chemistry C* **2007**, *111*, 1042-1048.
9. Wang, Z.; Hou, J.; Yang, C.; Jiao, S.; Huang, K.; Zhu, H., "Hierarchical metastable [gamma]-TaON hollow structures for efficient visible-light water splitting", *Energy & Environmental Science* **2013**, *6*, 2134-2144.
10. Ong, W.-J.; Tan, L.-L.; Ng, Y. H.; Yong, S.-T.; Chai, S.-P., "Graphitic Carbon Nitride (g-C3N4)-Based Photocatalysts for Artificial Photosynthesis and Environmental Remediation: Are We a Step Closer To Achieving Sustainability?", *Chemical reviews* **2016**, *116*, 7159-7329.
11. Du, X.; Li, Q.; Su, H.; Yang, J., "Electronic and magnetic properties of V-doped anatase $\mathrm{Ti}{\mathrm{O}}_{2}$ from first principles", *Physical Review B* **2006**, *74*, 233201.
12. Shao, G., "Red Shift in Manganese- and Iron-Doped TiO2: A DFT+U Analysis", *The Journal of Physical Chemistry C* **2009**, *113*, 6800-6808.
13. Weng, H.; Yang, X.; Dong, J.; Mizuseki, H.; Kawasaki, M.; Kawazoe, Y., "Electronic structure and optical properties of the Co-doped anatase ${\mathrm{TiO}}_{2}$ studied from first principles", *Physical Review B* **2004**, *69*, 125219.
14. Gai, Y.; Li, J.; Li, S.-S.; Xia, J.-B.; Wei, S.-H., "Design of Narrow-Gap ${\mathrm{TiO}}_{2}$: A Passivated Codoping Approach for Enhanced Photoelectrochemical Activity", *Physical Review Letters* **2009**, *102*, 036402.
15. Yang, K.; Dai, Y.; Huang, B., "Study of the Nitrogen Concentration Influence on N-Doped TiO2 Anatase from First-Principles Calculations", *The Journal of Physical Chemistry C* **2007**, *111*, 12086-12090.
16. Di Valentin, C.; Pacchioni, G.; Selloni, A.; Livraghi, S.; Giamello, E., "Characterization of Paramagnetic Species in N-Doped TiO2 Powders by EPR

Spectroscopy and DFT Calculations", *The Journal of Physical Chemistry B* **2005**, *109*, 11414-11419.

17. Yang, K.; Dai, Y.; Huang, B., "Understanding Photocatalytic Activity of S- and P-Doped TiO2 under Visible Light from First-Principles", *The Journal of Physical Chemistry C* **2007**, *111*, 18985-18994.
18. Ji, G.; Gu, Z.; Lu, M.; Zhou, J.; Zhang, S.; Chen, Y., "First principles calculations of N:H co-doping effect on energy gap narrowing ofZnO", *Physica B: Physics of Condensed Matter* **2010**, *405*, 4948-4950.
19. Xu, Z.; Zheng, Q.-R.; Su, G., "Charged states and band-gap narrowing in codoped ZnO nanowires for enhanced photoelectrochemical responses: Density functional first-principles calculations", *Physical Review B* **2012**, *85*, 075402.
20. Wang, F.; Di Valentin, C.; Pacchioni, G., "Doping of WO3 for Photocatalytic Water Splitting: Hints from Density Functional Theory", *The Journal of Physical Chemistry C* **2012**, *116*, 8901-8909.
21. Wei, W.; Dai, Y.; Guo, M.; Yu, L.; Jin, H.; Han, S.; Huang, B., "Codoping synergistic effects in N-doped SrTiO3 for higher energy conversion efficiency", *Physical Chemistry Chemical Physics* **2010**, *12*, 7612-7619.
22. Ryu, G. S.; Kim, J. S.; Jeong, S. H.; Song, C. K., "A printed OTFT-backplane for AMOLED display", *Org. Electron.* **2013**, *14*, 1218-1224.
23. Yanagida, S.; Kabumoto, A.; Mizumoto, K.; Pac, C.; Yoshino, K., "Poly(p-phenylene)-catalysed photoreduction of water to hydrogen", *Journal of the Chemical Society, Chemical Communications* **1985**, 474-475.
24. Wang, X. C.; Maeda, K.; Thomas, A.; Takanabe, K.; Xin, G.; Carlsson, J. M.; Domen, K.; Antonietti, M., "A metal-free polymeric photocatalyst for hydrogen production from water under visible light", *Nature Materials* **2009**, *8*, 76-80.
25. Liu, J.; Liu, Y.; Liu, N.; Han, Y.; Zhang, X.; Huang, H.; Lifshitz, Y.; Lee, S.-T.; Zhong, J.; Kang, Z., "Metal-free efficient photocatalyst for stable visible water splitting via a two-electron pathway", *Science* **2015**, *347*, 970.
26. Zhang, G.; Lan, Z.-A.; Lin, L.; Lin, S.; Wang, X., "Overall water splitting by Pt/g-C3N4 photocatalysts without using sacrificial agents", *Chemical Science* **2016**, *7*, 3062-3066.
27. Zhang, J.; Zhang, G.; Chen, X.; Lin, S.; Möhlmann, L.; Dołęga, G.; Lipner, G.; Antonietti, M.; Blechert, S.; Wang, X., "Co-Monomer Control of Carbon Nitride Semiconductors to Optimize Hydrogen Evolution with Visible Light", *Angewandte Chemie International Edition* **2012**, *51*, 3183-3187.
28. Jorge, A. B.; Martin, D. J.; Dhanoa, M. T. S.; Rahman, A. S.; Makwana, N.; Tang, J. W.; Sella, A.; Cora, F.; Firth, S.; Darr, J. A.; McMillan, P. F., "H-2 and O-2 Evolution from Water Half-Splitting Reactions by Graphitic Carbon Nitride Materials", *Journal of Physical Chemistry C* **2013**, *117*, 7178-7185.
29. Schwinghammer, K.; Tuffy, B.; Mesch, M. B.; Wirnhier, E.; Martineau, C.; Taulelle, F.; Schnick, W.; Senker, J.; Lotsch, B. V., "Triazine-based carbon nitrides for visible-light-driven hydrogen evolution", *Angewandte Chemie International Edition in English* **2013**, *52*, 2435-9.
30. Ge, L.; Han, C.; Xiao, X.; Guo, L.; Li, Y., "Enhanced visible light photocatalytic hydrogen evolution of sulfur-doped polymeric g-C3N4 photocatalysts", *Materials Research Bulletin* **2013**, *48*, 3919-3925.

31. Sui, Y.; Liu, J.; Zhang, Y.; Tian, X.; Chen, W., "Dispersed conductive polymer nanoparticles on graphitic carbon nitride for enhanced solar-driven hydrogen evolution from pure water", *Nanoscale* **2013**, *5*, 9150-9155.
32. Hong, Z.; Shen, B.; Chen, Y.; Lin, B.; Gao, B., "Enhancement of photocatalytic H2 evolution over nitrogen-deficient graphitic carbon nitride", *Journal of Materials Chemistry A* **2013**, *1*, 11754-11761.
33. Chu, S.; Wang, Y.; Guo, Y.; Feng, J.; Wang, C.; Luo, W.; Fan, X.; Zou, Z., "Band Structure Engineering of Carbon Nitride: In Search of a Polymer Photocatalyst with High Photooxidation Property", *ACS Catalysis* **2013**, *3*, 912-919.
34. Kailasam, K.; Schmidt, J.; Bildirir, H.; Zhang, G.; Blechert, S.; Wang, X.; Thomas, A., "Room Temperature Synthesis of Heptazine-Based Microporous Polymer Networks as Photocatalysts for Hydrogen Evolution", *Macromolecular Rapid Communications* **2013**, *34*, 1008-1013.
35. Schwab, M. G.; Hamburger, M.; Feng, X.; Shu, J.; Spiess, H. W.; Wang, X.; Antonietti, M.; Müllen, K., "Photocatalytic hydrogen evolution through fully conjugated poly(azomethine) networks", *Chemical Communications* **2010**, *46*, 8932-8934.
36. Chu, S.; Wang, Y.; Guo, Y.; Zhou, P.; Yu, H.; Luo, L.; Kong, F.; Zou, Z., "Facile green synthesis of crystalline polyimide photocatalyst for hydrogen generation from water", *Journal of Materials Chemistry* **2012**, *22*, 15519-15521.
37. Zhang, Z.; Long, J.; Yang, L.; Chen, W.; Dai, W.; Fu, X.; Wang, X., "Organic semiconductor for artificial photosynthesis: water splitting into hydrogen by a bioinspired C3N3S3 polymer under visible light irradiation", *Chemical Science* **2011**, *2*, 1826-1830.
38. Grem, G.; Leditzky, G.; Ullrich, B.; Leising, G., "Realization of a blue-light-emitting device using poly(p-phenylene)", *Advanced Materials* **1992**, *4*, 36-37.
39. Grem, G.; Leditzky, G.; Ullrich, B.; Leising, G., "Blue electroluminescent device based on a conjugated polymer", *Synthetic Metals* **1992**, *51*, 383-389.
40. Shibata, T.; Kabumoto, A.; Shiragami, T.; Ishitani, O.; Pac, C.; Yanagida, S., "Novel visible-light-driven photocatalyst. Poly(p-phenylene)-catalyzed photoreductions of water, carbonyl compounds, and olefins", *Journal of Physical Chemistry* **1990**, *94*, 2068-2076.
41. Sprick, R. S.; Bonillo, B.; Clowes, R.; Guiglion, P.; Brownbill, N. J.; Slater, B. J.; Blanc, F.; Zwijnenburg, M. A.; Adams, D. J.; Cooper, A. I., "Visible Light-Driven Water Splitting Using Planarized Conjugated Polymer Photocatalysts", *Angewandte Chemie International Edition* **2016**, *55*, 1792-1796.
42. Liebig, J., "Uber einige Stickstoff - Verbindungen", *Annalen der Pharmacie* **1834**, *10*, 1-47.
43. Jürgens, B.; Irran, E.; Senker, J.; Kroll, P.; Müller, H.; Schnick, W., "Melem (2,5,8-Triamino-tri-s-triazine), an Important Intermediate during Condensation of Melamine Rings to Graphitic Carbon Nitride: Synthesis, Structure Determination by X-ray Powder Diffractometry, Solid-State NMR, and Theoretical Studies", *Journal of the American Chemical Society* **2003**, *125*, 10288-10300.

44. Butchosa, C.; Guiglion, P.; Zwijnenburg, M. A., "Carbon Nitride Photocatalysts for Water Splitting: A Computational Perspective", *The Journal of Physical Chemistry C* **2014**, *118*, 24833-24842.
45. Sprick, R. S.; Jiang, J.-X.; Bonillo, B.; Ren, S.; Ratvijitvech, T.; Guiglion, P.; Zwijnenburg, M. A.; Adams, D. J.; Cooper, A. I., "Tunable Organic Photocatalysts for Visible Light-Driven Hydrogen Evolution", *Journal of the American Chemical Society* **2015**, *137*, 3265-3270.
46. Lukeš, V.; Aquino, A. J. A.; Lischka, H.; Kauffmann, H.-F., "Dependence of Optical Properties of Oligo-para-phenylenes on Torsional Modes and Chain Length", *The Journal of Physical Chemistry B* **2007**, *111*, 7954-7962.
47. Chen, L.; Honsho, Y.; Seki, S.; Jiang, D., "Light-Harvesting Conjugated Microporous Polymers: Rapid and Highly Efficient Flow of Light Energy with a Porous Polyphenylene Framework as Antenna", *Journal of the American Chemical Society* **2010**, *132*, 6742-6748.
48. He, J.; Crase, J. L.; Wadumethrige, S. H.; Thakur, K.; Dai, L.; Zou, S.; Rathore, R.; Hartley, C. S., "ortho-Phenylenes: Unusual Conjugated Oligomers with a Surprisingly Long Effective Conjugation Length", *Journal of the American Chemical Society* **2010**, *132*, 13848-13857.
49. Hartley, C. S., "Excited-state behavior of ortho-phenylenes", *J Org Chem* **2011**, *76*, 9188-91.
50. Xu, Y.; Jiang, D., "Structural Insights into the Functional Origin of Conjugated Microporous Polymers: Geometr Management of Porosity and Electronic Properties", *Chemical Communications* **2014**,
51. Zwijnenburg, M. A., "Elucidating the Microscopic Origin of the Unique Optical Properties of Polypyrene", *The Journal of Physical Chemistry C* **2012**, *116*, 20191-20198.
52. Wang, X.; Maeda, K.; Thomas, A.; Takanabe, K.; Xin, G.; Carlsson, J. M.; Domen, K.; Antonietti, M., "A metal-free polymeric photocatalyst for hydrogen production from water under visible light", *Nat Mater* **2009**, *8*, 76-80.
53. Jiang, J.-X.; Trewin, A.; Adams, D. J.; Cooper, A. I., "Band gap engineering in fluorescent conjugated microporous polymers", *Chemical Science* **2011**, *2*, 1777-1781.
54. Ren, S.; Dawson, R.; Laybourn, A.; Jiang, J.-x.; Khimyak, Y.; Adams, D. J.; Cooper, A. I., "Functional conjugated microporous polymers: from 1,3,5-benzene to 1,3,5-triazine", *Polymer Chemistry* **2012**, *3*, 928-934.
55. Cheng, G.; Hasell, T.; Trewin, A.; Adams, D. J.; Cooper, A. I., "Soluble Conjugated Microporous Polymers", *Angewandte Chemie International Edition* **2012**, *51*, 12727-12731.
56. Zwijnenburg, M. A.; Cheng, G.; McDonald, T. O.; Jelfs, K. E.; Jiang, J. X.; Ren, S. J.; Hasell, T.; Blanc, F.; Cooper, A. I.; Adams, D. J., "Shedding Light on Structure-Property Relationships for Conjugated Microporous Polymers: The Importance of Rings and Strain", *Macromolecules* **2013**, *46*, 7696-7704.
57. Lau, V. W.-h.; Mesch, M. B.; Duppel, V.; Blum, V.; Senker, J.; Lotsch, B. V., "Low-Molecular-Weight Carbon Nitrides for Solar Hydrogen Evolution", *Journal of the American Chemical Society* **2015**, *137*, 1064-1072.
58. Schwinghammer, K.; Hug, S.; Mesch, M. B.; Senker, J.; Lotsch, B. V., "Phenyl-triazine oligomers for light-driven hydrogen evolution", *Energy & Environmental Science* **2015**, DOI: 10.1039/C5EE02574E.

59. Butchosa, C.; McDonald, T. O.; Cooper, A. I.; Adams, D. J.; Zwijnenburg, M. A., "Shining a Light on s-Triazine-Based Polymers", *The Journal of Physical Chemistry C* **2014**, *118*, 4314-4324.
60. Jiang, X.; Wang, P.; Zhao, J., "2D covalent triazine framework: a new class of organic photocatalyst for water splitting", *Journal of Materials Chemistry A* **2015**, *3*, 7750-7758.
61. Cooper, A. http://www.liv.ac.uk/cooper-group/.
62. Hohenberg, P.; Kohn, W., "Inhomogeneous Electron Gas", *Physical Review* **1964**, *136*, 864-871.
63. Kohn, W.; Sham, L. J., "Self-Consistent Equations Including Exchange and Correlation Effects", *Physical Review* **1965**, *140*, 1133-1138.
64. Runge, E.; Gross, E. K. U., "Density-Functional Theory for Time-Dependent Systems", *Physical Review Letters* **1984**, *52*, 997-1000.

CHAPTER 2:

Theoretical foundations

In this chapter, I will lay the foundations of the thesis by introducing the theoretical frameworks used throughout my project. I will first present Density Functional Theory (DFT), the main computational quantum mechanical modelling method of choice here, that is particularly valuable to investigate the electronic structure of atoms and molecules. I will explain how the theory was constructed over time, and how several key insights led it to become one of the most powerful and routinely used computational methods. I will then outline the functionals and basis-sets needed within its framework. Second, I will describe time-dependent DFT (TD-DFT), a crucial extension of DFT that enables one, among other things, to calculate the electronic structure of atoms and molecules in their excited state. Third, I will briefly outline an additional computational method, coupled-cluster, or more precisely the approximate coupled-clusters singles-and-doubles method (CC2), that involves a completely different approach to modelling the electronic structure, and is hence very complementary to (TD-)DFT. Fourth, I will discuss the conductor-like screening model (COSMO), a solvation model that that will be particularly useful to model the effect of the chemical environment. Finally, I will explain the methodology used to carry out conformational searches, which is crucial in order to find the molecular structures of relevant conformers before DFT optimisation.

2.1. Density Functional Theory (DFT)

The ultimate goal of most quantum chemical approaches is to find the ground-state energy of non-relativistic electrons for arbitrary positions of nuclei, within the Born-Oppenheimer approximation[1]. The direct approach to treat this problem is to solve the time-independent, non-relativistic electronic Schrödinger equation:

$$\hat{\mathrm{H}}_{elec}\Psi_{elec}\left(\vec{x_1},\vec{x_2},...,\vec{x_n}\right)=\mathrm{E}_{elec}\Psi_{elec}\left(\vec{x_1},\vec{x_2},...,\vec{x_n}\right) \quad (1)$$

where:

- Ψ_{elec} is the many-body wavefunction describing the electronic state of the system, depending on 3N spatial coordinates $\left\{\vec{\mathrm{r}}_i\right\}$ and N spin coordinates $\left\{\mathrm{s}_i\right\}$, which are collectively termed $\vec{x_i}$ (with $\vec{x_i}=\vec{\mathrm{r}}_i\cdot\mathrm{s}_i$),
- $\hat{\mathrm{H}}_{elec}=\hat{T}+\hat{V}_{Ne}+\hat{V}_{ee}$ is the electronic Hamiltonian, containing the total energy of the electrons ($\hat{\mathrm{T}}$ denotes the kinetic energy operator, $\hat{\mathrm{V}}_{Ne}$ and $\hat{\mathrm{V}}_{ee}$ the potential energy operators, respectively for the nuclear-electron attraction, and the electron-electron repulsion).

Solving this equation is an exceedingly difficult task, whose computational cost scales exponentially with the number of electrons. For instance, just to store the ground state of the oxygen atom, Ψ_{elec} would depend on 24 coordinates, three for each of the eight electrons, disregarding spin. Considering only ten grid-points for each coordinate, one would need 10^{24} numbers to represent this wavefunction[2]. Therefore, a method such as Density Functional Theory that can yield interesting quantities, namely the ground state energy of a system, bypassing the need to calculate Ψ, is extremely attractive. In DFT, one writes the ground state energy in terms of the electron density $\rho(\vec{\mathrm{r}})$ (defined by the probability of finding any electron in the volume $d^3\vec{\mathrm{r}}$ around $\vec{\mathrm{r}}$) instead of the wavefunction Ψ.

2.1.1. Thomas-Fermi model

The first attempts to employ the electron density rather than the wavefunction date back to 1927, with the work of Thomas[3] and Fermi[4]. Their approach was based on approximating the kinetic energy T^{TF} using a quantum statistical (fictitious) model of a uniform, non-interacting, spin-unpolarised N-electron gas of density $\rho(\vec{r})$, while treating the other two contributions to the total energy, E_{Ne} and E_{ee}, in a purely classical way:

$$T^{TF}\left[\rho(\vec{r})\right] = \frac{3}{10}\left(3\pi^2\right)^{2/3}\int \rho^{5/3}(\vec{r})\,d\vec{r} \tag{2}$$

$$E_{Ne}\left[\rho(\vec{r})\right] = -Z\int \frac{\rho(\vec{r})}{|\vec{r}|}d\vec{r} \tag{3}$$

$$E_{ee}\left[\rho(\vec{r})\right] = \frac{1}{2}\iint \frac{\rho(\vec{r_1})\rho(\vec{r_2})}{|\vec{r_1}-\vec{r_2}|}d\vec{r_1}d\vec{r_2} \tag{4}$$

$E_{ee}\left[\rho(\vec{r})\right]$ is then minimised under the constraints that the electron density must be positive and integrate to N:

$$\rho(\vec{r}) \geq 0 \quad \text{and} \quad \int \rho(\vec{r})\,d\vec{r} = N \tag{5}$$

This extremely crude approximation gives roughly correct energies (errors about 10% for many systems[5]) but is not nearly good enough for most properties of interest (for instance, molecules do not bind in this model[6]). However, it provides for the first time a way of mapping the electron density to the energy, without any other information required. The Thomas-Fermi energy is the first example of a genuine density functional, as $E^{TF}\left[\rho(\vec{r})\right]$ is a functional of the density $\rho(\vec{r})$.

2.1.2. Hohenberg-Kohn theorems

It is only in 1964, nearly 40 years later, that Hohenberg and Kohn[7] gave a rigorous proof that such a mapping between the electron density and the ground state energy of the electrons was physically justified. They showed that the solution of the many-body problem could be found, in principle, from a density functional.

The first Hohenberg theorem states that the ground-state density $\rho(\vec{r})$ uniquely determines the external potential $V_{ext}(\vec{r})$ (which includes $V_{Ne}(\vec{r})$ and hypothetical external electromagnetic fields) felt by the electrons, up to an arbitrary constant. It follows that the density completely and uniquely determines the Hamiltonian, which in turn defines the ground state energy, and *all* other properties of the system.

In the absence of additional external electromagnetic field, the external potential is fully defined by the attraction to the nuclei. Since the ground state energy E_0 is a functional of the ground state density ρ_0, so are its individual constituents, and it follows that:

$$E_0[\rho_0] = \int \rho_0(\vec{r}) V_{Ne}(\vec{r}) d\vec{r} + T[\rho_0] + E_{ee}(\rho_0) \qquad (6)$$

where the first integral is the only system-dependent part, and the second part, $T[\rho_0] + E_{ee}(\rho_0)$, also called $F^{HK}[\rho_0]$ is the *Hohenberg-Kohn functional*, a universal functional (*i.e.* unique and valid for any possible system).

If this universal functional (also known as the "holy grail" of DFT) was known formally, one would be able to solve the Schrödinger equation *exactly*, for *any* system. Unfortunately, it is not the case, as it contains the functional for the kinetic energy and for the electron-electron interaction, which are completely unknown due to instantaneous electron correlations (*Coulomb* and *exchange*) that can't be described in a classical way.

The second Hohenberg-Kohn theorem, using the variational principle, states that $\mathrm{F}^{HK}\left[\rho_0\right]$ delivers the ground state (lowest) energy of the system if and only if the input density is ρ_0, the true ground state density of the system.

2.1.3. Kohn-Sham approach

It has to be noted at this point that for all practical purposes, there is no wavefunction in density functional theory (there is no way in practice to go back to the true wavefunction of a system, even with its exact ground state energy or density). However, as we will see in this section, it is possible to build fictitious orbitals (and hence a fictitious wavefunction) that will help us describe the system of interest and approximate its ground state energy.

Shortly after the Hohenberg-Kohn theorems, in 1965, Kohn and Sham[8] made a very clever observation: they found that a major flaw in most density functional approaches (as the Thomas-Fermi one) was the way kinetic energy was treated. Indeed, due to electron correlations, the positions and velocities of electrons are unknown, and the term $-\frac{1}{2}\sum_{i}^{N}\left(\nabla_i^2\right)$ can't be written explicitly in the Hamiltonian. Kohn and Sham realised that another method performed much better in this respect[9]: the Hartree-Fock method.

The Hartree-Fock method, in order to solve the Schrödinger equation, approximates the full many-body wavefunction to a N-electron single Slater determinant (*i.e.* an antisymmetric product of N one-electron orbitals). This approach treats all electrons as non-interacting particles. Instead, each single electron evolves independently in the mean field created by the N-1 others (the Coulomb repulsion is only described in an average, classical way, and the remaining instantaneous electron-electron correlation is completely neglected). However, by construction, such a wavefunction must satisfy the condition that two electrons of anti-parallel spins cannot be found

at the same position in space (Pauli exclusion principle). The electrons therefore feel an additional repulsion, known as the *exchange*, or *Fermi* correlation.

The game-changing idea of Kohn and Sham, in order to capture as much kinetic energy as possible, was to treat the electrons as non-interacting particles, like in Hartree-Fock. Considering such a non-interacting reference system, they built an effective Hamiltonian with an effective, one-electron potential $\mathrm{V}_{eff}(\vec{\mathrm{r}})$, containing the average electron-electron repulsion and the nuclear-electron repulsion:

$$\hat{\mathrm{H}}_{eff} = -\frac{1}{2}\sum_{i}^{N}\left(\nabla_i^2\right) + \sum_{i}^{N}\mathrm{V}_{eff}\left(\vec{\mathrm{r}}_i\right) = \sum_{i}^{N}\left\{-\frac{1}{2}\nabla_i^2 + \mathrm{V}_{eff}\left(\vec{\mathrm{r}}_i\right)\right\} \tag{7}$$

$$\hat{\mathrm{H}}_{eff} = \sum_{i}^{N}\hat{\mathrm{h}}\left(\vec{\mathrm{r}}_i\right) \tag{8}$$

Finding much inspiration in the Hartree-Fock method, they built a "Kohn-Sham" wavefunction Φ^{KS} for this reference system, defined as a Slater determinant of N non-interacting one-electron "Kohn-Sham" orbitals φ_i^{KS}. These orbitals are determined by solving N one-electron Schrödinger equations:

$$\hat{\mathrm{h}}\varphi_i^{KS} = \varepsilon_i\varphi_i^{KS} \tag{9}$$

The Kohn-Sham electron density is then retrieved, by definition, by summing the squared moduli of these orbitals. Kohn and Sham then introduced a crucial condition: the effective potential V_{eff} must be chosen such that *the electron density of this fictitious system,* $\rho_S(\vec{\mathrm{r}})$*, exactly equals the ground state density of the real system*, composed of fully interacting electrons.

$$\rho_S \equiv \rho_0 = \sum_{i}^{N}\left|\varphi_i^{KS}\right|^2 \tag{10}$$

Having an expression for the density, all terms included in the total electronic energy can now be expressed as a functional of ρ_0, except the kinetic energy that still needs to be written in terms of orbitals, as in the Hartree-Fock scheme.

$$\mathrm{E}[\rho] = \mathrm{T}[\rho] + \mathrm{E}_{ee}[\rho] + \mathrm{E}_{Ne}[\rho] \tag{11}$$

$$\mathrm{E}[\rho] = \mathrm{T}^{KS}[\rho] + \mathrm{E}_{ee,Coul}[\rho] + \mathrm{E}_{Ne}[\rho] + \left\{T[\rho] - \mathrm{T}^{KS}[\rho]\right\} + \left\{\mathrm{E}_{ee}[\rho] - \mathrm{E}_{ee,Coul}[\rho]\right\} \tag{12}$$

$$\mathrm{E}[\rho] = \mathrm{T}^{KS}[\rho] + \mathrm{E}_{ee,Coul}[\rho] + \mathrm{E}_{Ne}[\rho] + \mathrm{E}_{XC}[\rho] \tag{13}$$

$$\mathrm{E}[\rho] = -\frac{1}{2}\sum_{i}^{N}\left\langle \varphi_i^{KS}\middle|\nabla^2\middle|\varphi_i^{KS}\right\rangle + \frac{1}{2}\iint \frac{\rho(\vec{\mathrm{r}}_1)\rho(\vec{\mathrm{r}}_2)}{\left|\vec{\mathrm{r}}_1 - \vec{\mathrm{r}}_2\right|} d\vec{\mathrm{r}}_1 d\vec{\mathrm{r}}_2 - \int \frac{Z\rho(\vec{\mathrm{r}})}{|\vec{\mathrm{r}}|} d\vec{\mathrm{r}} + \mathrm{E}_{XC}[\rho] \tag{14}$$

In this approach, all known energies (namely the non-interacting kinetic energy, the classical (average) Coulomb electron-electron repulsion, and the classical nuclear-electron attraction) are described explicitly *via* the Kohn-Sham Hamiltonian, while all remaining corrections needed to reach the *exact* ground state energy of the real interacting system (namely the missing part of the kinetic energy, the *Coulomb* correlation, the *exchange* correlation, and the electron self-interaction correction) are gathered in an additional term, the so-called *exchange-correlation* energy $\mathrm{E}_{XC}\left[\rho(\vec{\mathrm{r}})\right]$.

As V_{eff}, which is needed to build the orbitals and compute the electron density, depends itself on the electron density, this is a self-consistent equation that must be solved iteratively, by looping through:

- Guessing an initial effective potential V_{eff},
- Building the effective one-electron Hamiltonians,
- Solving the one-electron Schrödinger equations to build the Kohn-Sham orbitals,
- Computing the electron density, and the total electronic energy,
- Recalculating V_{eff} from the density, and so on…

One can also start by guessing initial orbitals, and then compute the density, calculate V_{eff}, build $\hat{\mathrm{H}}_{eff}$ and solve the Schrödinger equation, to finally find the orbitals, and repeat till convergence.

2.1.4. Functionals

We just saw that the exchange-correlation (XC) functional $E_{XC}[\rho]$ plays a crucial role in DFT. It is the only remaining part that needs to be approximated, in order to get closer to chemical accuracy. Many different types of XC functionals have been developed over the years, and fall in three main categories: LDA, GGA, or hybrid functionals.

The simplest approximation to the XC potential is the local density approximation (LDA), where the density $\rho(\vec{r})$ is treated locally as a uniform electron gas. This model is rather far from any realistic situation for atoms or molecules, which are usually characterised by rapidly varying densities. However, it does give rather accurate results in many cases, due to serendipitous error cancellation. The generalised gradient approximation (GGA) was then introduced to account for the non-homogeneity of the real electron density, by adding information about the gradient of the charge density, $\nabla\rho(\vec{r})$.

As it has been known from the HF theory that the exact exchange energy can be computed from a slater determinant, it then seemed appropriate to introduce some "exact" Hartree-Fock exchange in the XC term, instead of relying on density functionals. However, only some fraction of this "HF-like" exchange energy can be used to good accuracy, since this is now built from Kohn-Sham orbitals, instead of the true orbitals of the real, interacting system. This is the concept behind hybrid functionals. For example, the B3LYP[10-13] hybrid functional, which is one of the most popular for chemical applications, contains 20% of HF-like exchange. In this project, unless stated otherwise, I will use the B3LYP functional, one of the most successful and widely used functionals in the literature, that is overall well-balanced; it gives accurate predictions for many properties over a wide range of chemical systems. However, the B3LYP functional has well-known shortcomings: among others, it fails at predicting charge-transfer (CT) excitations, Rydberg states, and other long-range interactions such as van der Waals forces and hydrogen bonding. To address those issues, the BHLYP (50% HF-like exchange) and the CAM-B3LYP[14] (Coulomb-

attenuated, with a distance-dependent HF-like exchange percentage) functionals will also be used. CAM-B3LYP is a range-separated exchange-correlation that combines the hybrid qualities of B3LYP and the long-range correction presented by Tawada et al.[15] The CAM-B3LYP functional comprises 19% HF-like exchange interaction at short-range, and 65% HF-like at long-range, which makes it performs well for CT excitations, which B3LYP underestimates enormously.

2.1.5. Basis sets

In DFT, the complex system of coupled equations introduced by the Kohn-Sham scheme needs to be solved in a computationally efficient way. Procedures that expand the orbitals on a grid can be employed, but are too much demanding for routine applications, and other techniques are required. For most applications, linear combinations of atomic orbitals (LCAO) are used to linearly expand the Kohn-Sham orbitals in a set of basis functions $\{\theta_\mu\}$, as introduced by Roothaan in the HF framework:

$$\varphi_i^{KS} = \sum_{\mu}^{L} c_{\mu i}\, \theta_\mu \tag{15}$$

If the basis was complete ($L \to \infty$), every orbital φ_i^{KS} could be expressed exactly. However, this is not possible in real applications, and finite sets of L basis functions are used. The basis should be designed in a way that allows for an orderly and systematic extension towards completeness, rapid convergence to any atomic or molecular electronic state (requiring just a few terms for an accurate description of the electronic distribution) and the functions $\theta_\mu(\vec{r})$ should have an analytical form allowing for simple manipulation[16].

One of the most accurate ways to describe atomic orbitals, from a physical point of view, is to use Slater-type Orbitals (STOs): indeed, they decay exponentially with distance from the nuclei, and reach a maximum at zero, accurately describing the long-range overlap between atoms and the charge and spin at the nucleus. However, STOs are computationally demanding. In molecular calculations, the most widely

used type of basis functions is Gaussian-type Orbitals (GTOs): they combine reasonably short expansions with a fast integral evaluation, and relatively high computational efficiency. Therefore, GTOs are used almost universally as basis functions in molecular calculations and they are centred at the nuclei of the atoms. They can be expressed in Cartesian form, as:

$$\theta_{\zeta,l_x,l_y,l_z}(x,y,z)^{GTO} = \mathrm{N}\, x^{l_x} y^{l_y} z^{l_z} e^{-\zeta r^2} \tag{16}$$

where ζ is the orbital exponent which translates how compact (large ζ) or diffuse (small ζ) the resulting function is, and $l_x + l_y + l_z$ determines the type of orbital (*e.g.* $l_x + l_y + l_z = 0$ or 1, respectively for a *s* or a *p* orbital).

Nowadays, most molecular quantum chemistry codes relying on the Kohn-Sham approach employ the so-called *contracted* Gaussian functions (CGFs), where the basis functions are designed as linear combinations of primitive GTOs, with coefficients chosen in such a way that they resemble as much as possible a single STO function.

The number of primitive functions used for the expansion of the electron density defines the quality of the CGF basis set. The simplest expansion utilises only enough functions to contain all the electrons of the neutral atoms and it is called the *minimal* basis set. The next level of accuracy is obtained with the *double-zeta* basis sets, where the term ζ refers to the exponent of the primitive GTOs and *double* means that two contracted functions are employed for each atomic orbital. However, by considering that chemical reactivity is better described by the valence space, one can limit the use of CGFs to the valence orbitals, and describe the inert core electrons with the *minimal* set. This defines the *split-valence* basis sets. The next level of sophistication requires the use of polarisation functions, *i.e.* functions of higher angular momentum than those occupied in the atom, such as p-functions for hydrogen, which ensure that the orbitals can deform from their initial symmetry to better adapt to the molecular environment[9].

In this project, unless stated otherwise, I will mainly use the DZP (Double Zeta plus Polarisation) basis set, but the def-SVP (Split-Valence plus Polarisation), and the def2-TZVP(P) (Triple Zeta Split-Valence plus Polarisation) basis sets will also be employed in particular cases.

2.2. Time-Dependent Density Functional Theory

Nowadays, DFT is a widely used method to predict ground-state quantities (ground state energies and equilibrium geometries, binding energies, forces and electric constants, dipole moments, and static polarisabilities). However, to describe the behaviour of molecules that are not in their ground state, static DFT is not enough. Indeed, the inability of the latter method to describe excitations severely restricts its range of applications, since many crucial properties such as the band gap in semiconductors, or the optical/fundamental gaps in molecules, as well as their optical absorption and emission, are associated with excited states.

In such cases, time-dependent DFT is the method of choice. TD-DFT allows one to follow the dynamic response of systems out of equilibrium (*e.g.* molecules irradiated by an external electromagnetic field). In such a quantum system, when electronic transitions occur, TD-DFT can be used to compute excited state properties, such as excitation energies, excited-state geometries and electronic densities[17].

In this project, I will carry out linear-response TD-DFT calculations within the context of the adiabatic approximation (see below), to predict absorption and fluorescence energies, excited-state geometries, for selected conjugated oligomers, and calculate the standard reduction potentials associated with them, when they are involved in the photocatalysis of water splitting half-reactions.

2.2.1. Formalism

The most direct approach to calculating the behaviour of electrons in a time-dependent field would be to solve the time-dependent Schrödinger equation. However, this task can rapidly become extremely computationally expensive, and hence prohibitive, mainly due to the Coulomb repulsion between electrons. Instead, many aspects of TD-DFT build upon the ground state DFT framework. In DFT, the Hohenberg-Kohn theorem provides a one-to-one mapping between any time-

independent external potential and the resulting electronic density, up to a constant. In TD-DFT, its analogue, the Runge-Gross[18] theorem, provides a one-to-one mapping between any *time-dependent* external potential and the resulting *time-dependent* electronic density, up to a *time-dependent* constant. For a given initial state, the electronic density, a function of just three spatial variables plus time, determines all other properties of the interacting many-electron system[2].

An adaptation of the Kohn-Sham approach can then be used, as formally proven by van Leeuwen[19]. It guarantees that the time-dependent density $\rho(\vec{r},t)$ of an interacting system, evolving from an initial state Ψ_0 under the influence of a potential $v(\vec{r},t)$ can also be represented by a non-interacting system[17], evolving under the effective potential:

$$v_S[\rho,\Psi_0,\Phi_0](\vec{r},t) \tag{17}$$

which is a functional of the time-dependent density, the initial many-body state, and the initial state Φ_0 of the non-interacting system. However, if the system is initially (at t_0) in its ground state, the Hohenberg-Kohn theorems apply, and Ψ_0 and Φ_0 become functionals of the ground-state density, turning v_S into a functional of the density only, $v_S[\rho](\vec{r},t)$. The initial wavefunction Φ_0 is made up of the Kohn-Sham orbitals φ_i^{KS}, following a self-consistent solution of the static Kohn-Sham equation.

Immediately after t_0, the time-dependent potential kicks in: the system starts to evolve under its influence, and the time-dependent density is given by:

$$\rho_S(\vec{r},t) \equiv \rho(\vec{r},t) = \sum_j^N \left|\varphi_j^{KS}(\vec{r},t)\right|^2 \tag{18}$$

where the $\varphi_j^{KS}(\vec{r},t)$ follow from the time-dependent Kohn-Sham equation:

$$\left[-\frac{\nabla^2}{2} + v_S[\rho](\vec{r},t)\right]\varphi_j^{KS}(\vec{r},t) = i\frac{\partial}{\partial t}\varphi_j^{KS}(\vec{r},t) \tag{19}$$

which translates the time-propagation of the N initially occupied single-electron orbitals from a time t_0 (with the condition that $\varphi_j^{KS}(\vec{r}, t_0)$ is time-independent) to a time t. Like in static DFT, a formally unknown exchange-correlation potential is now defined as a time-dependent quantity, which as always needs to be approximated, in a quantum chemistry code, for "real" applications.

Currently, most applications of TD-DFT are in the so-called *linear* response regime (*i.e.* for external perturbations that are small, in the sense that they do not completely destroy the ground state structure of the system), and are based upon the *linear response* theory. Nevertheless, TD-DFT can also be used in the *non-linear* regime (*e.g.* when using strong laser fields).

2.2.2. Adiabatic approximation

As the time-dependent density evolves, the exchange-correlation potential exhibits a *history dependence*,[20] meaning that it is defined not solely by the present density $\rho(\vec{r}, t)$ but also by its history $\rho(\vec{r}, t')$ $0 \leq t' < t$. The adiabatic approximation, which is used in the vast majority of TD-DFT calculations in the literature, ignores all dependence on the past, and allows only a dependence on the instantaneous density of the system[21] (*i.e.* it approximates the density as being local in time, which is valid when the time-dependent potential changes slowly). In practice, it means that the (TD-)DFT functionals used throughout this project are in fact ground state functionals.

2.2.3. Strengths and limitations of (TD-)DFT

As seen previously, in DFT, the Kohn-Sham orbitals are a useful fictitious representation for the real, interacting system. As a result, some properties are poorly described by this approach. For example, the Kohn-Sham HOMO-LUMO gap is not the fundamental gap of the system (as explained in the previous section, see

also Chapter 3). For the Helium atom, the difference between the KS gap and the fundamental gap ranges up to 3.5 eV.

Time-dependent DFT generally yields accurate excited state properties, such as bond lengths, vibrational frequencies, forces and dipole moments, and it is well established that conventional GGA and hybrid functionals are accurate to within 0.1-0.5 eV in the description of local excitations[22-23]. In practice, adiabatic linear-response TD-DFT achieves remarkable balance between accuracy and efficiency, to calculate the excited state properties of molecular clusters.

However, it is known that TD-DFT usually fails to describe non-local excited state processes, such as charge-transfer and Rydberg excitations, or multiple excitations[24]. Although it doesn't fundamentally solve the issue (intrinsic to the way TD-DFT describes excitations), the range-separated CAM-B3LYP functional will be used, as mentioned earlier, in order to better approximate excitations for systems in which charge-transfer is likely to be problematic.

2.3. Coupled-cluster

Coupled-cluster (CC) methods[25-27], developed from the Hartree-Fock framework, are another way to tackle the many-body problem. Instead of relying on the electronic density, like (TD-)DFT does, they reformulate the electronic Schrödinger equation by expressing the ground state wavefunction Ψ_{CC} using an exponential excitation operator:

$$\left|\Psi_{CC}\right\rangle = e^{\hat{\mathrm{T}}}\left|\Phi_0\right\rangle = \left(1 + \frac{\hat{\mathrm{T}}^2}{2!} + \frac{\hat{\mathrm{T}}^3}{3!} + \cdots\right)\left|\Phi_0\right\rangle \tag{20}$$

$$\hat{\mathrm{T}} = \hat{\mathrm{T}}_1 + \hat{\mathrm{T}}_2 + \hat{\mathrm{T}}_3 + \cdots \tag{21}$$

where Φ_0 is a reference wavefunction (typically a Slater determinant), and $\hat{\mathrm{T}}$ is the cluster operator, which produces a combination of excited determinants from the reference wavefunction (where $\hat{\mathrm{T}}_1$ is the operator of all single excitations, $\hat{\mathrm{T}}_2$ is the operator of all double excitations and so forth).

CC methods allow for efficient, accurate, and size-extensive description of solutions of the Schrödinger equation, for weakly correlated systems (*i.e.* where a single-determinant HF solution already gives a good approximation to the sought ground-state wavefunction, leaving only a very small correlation energy unaccounted for). Depending on the level of approximation needed, the cluster operator $\hat{\mathrm{T}}$ can include single excitations only (CCS, where $\hat{\mathrm{T}} = \hat{\mathrm{T}}_1$, scaling as N^4, N being the number of orbitals), or also double excitations (CCSD, where $\hat{\mathrm{T}} = \hat{\mathrm{T}}_1 + \hat{\mathrm{T}}_2$, scaling as N^6) and triple excitations (CCSDT, where where $\hat{\mathrm{T}} = \hat{\mathrm{T}}_1 + \hat{\mathrm{T}}_2 + \hat{\mathrm{T}}_3$ scaling as N^8), and so on. Because of the high computational cost of fully treating many excitations, some of them can be estimated non-iteratively using Many-Body Perturbation Theory arguments (*e.g.* CCSD(T) includes a full treatment of *singles* and *doubles*, while approximating the contribution of *triples* using perturbation theory).

In this project, to complement (TD-)DFT calculations in specific cases, I will use CC2:[28] it is an approximation to CCSD that scales as N^5 instead of N^6, which makes it more computationally tractable. From the CC2 response functions, dynamic properties as well as excitation energies and transition moments can be obtained[28].

2.4. Conductor-like screening model

When using computation methods to study materials, especially when trying to model the properties of molecular clusters, taking into consideration the chemical environment of said molecular cluster is of utmost importance. Indeed, molecules are rarely isolated, and the presence of a solvent can have a strong influence on their electronic, electrostatic and geometric properties. This is especially relevant in the case of photocatalysis, where the photoexcitation of electrons leads to the creation of excitons, that can subsequently dissociate, usually at an interface (*e.g.* between a solid particle and the solution around it), and generate charge carriers that may drive chemical (half-)reactions. In order to correctly describe those phenomena, the inclusion of solvent models therefore becomes crucial.

One strategy would be to model solvent molecules explicitly, by adding those discrete molecules directly to the chemical system of interest. One would then simulate their behaviour and interactions, not only with respect to the chemical system of interest, but also between the solvent molecules themselves. For such an approach to be relevant, it should take into account both short and long-range solvent effects (*e.g.* hydrogen bonding, or the screening of charges due to solvent polarisation), which would require the inclusion of hundreds of solvent molecules, and can therefore rapidly become prohibitively expensive computationally.

Another strategy (the one used throughout this project), fundamentally different, is to describe the solvent molecules implicitly. The conductor-like screening model (COSMO)[29-30] is a solvation model in which the solvent is treated as a dielectric continuum, possessing a relative permittivity ε_r. It surrounds the solute molecules by this dielectric continuum outside of a cavity, constructed by an aggregation of atom-centred spheres, slightly larger than their Van der Waals radii.

In the context of a DFT calculation, for example, the COSMO model generates screening charges on the cavity surface, whose distribution polarises the solvent as a response. A three-dimensional cavity surface grid is constructed, and the

screening charges calculated. Then, the potential generated by those charges is included in each self-consistent field (SCF) step of the DFT calculation, which guarantees that both screening charges and molecular orbitals are constantly being updated and optimised while taking the solvent into account.

2.5. Conformational search

Some structurally simple molecules, such as methanol, benzene and ethane, have only one unique conformer, at room temperature in their electronic ground state. In that case, their measured properties can be obtained by considering the structure of this single conformer. This is not necessarily the case for systems that possess additional degrees of freedom (*e.g.* chemical groups that can rotate around single bonds, such as ethanol and butane), where several low-energy conformers may co-exist, which is likely to happen when modelling larger, more structurally complex molecules like oligomers and polymers. The presence of different conformers, even when structurally similar or close in relative energy, can dramatically alter the overall properties of a chemical system, hence the need to perform a conformer analysis before choosing a particular molecular structure as a basis to run simulations.

In my project, I will use a low-mode sampling algorithm[31] coupled with the OPLS-2005 forcefield[32]. Low-mode searching explores the low-frequency eigenvectors of the system to generate new conformations. Starting from a given input structure, the algorithm generates normal modes, then selects one of these modes, amplifies it and distorts the molecule along it (within a predetermined distance limit) to generate a very different structure. This distorted structure is then optimised *via* the forcefield, and if the resulting geometry is unique, and its total energy falls within a chosen energy window (typically a few hundreds of kJ/mol, *i.e.* a few eV) then the new structure is saved, and the whole process repeated using a different mode, until the maximum number of steps (typically several thousand) is reached. In summary, upon completion, the conformational search algorithm finds other molecular structures that are energy minima on the potential energy surface and ranks them according to their energies (the conformers with the lowest energy being the most abundant).

In the case of conjugated oligomers, modelled as molecular clusters, several low-energy conformers found *via* conformational search are systematically considered,

and then optimised using DFT. Their optimised structures and relative ground-state energies are then compared. In this project, for each oligomer studied, I typically selected the lowest-energy conformer found, as well as one higher-energy conformer, and all other conformers described in the literature, when relevant (*e.g.* see Chapter 6).

2.6. References

1. Born, M.; Oppenheimer, R., "Zur Quantentheorie der Molekeln", *Annalen der Physik* **1927**, *389*, 457-484.
2. Gross, E. K. U.; Maitra, N. T., Fundamentals of time-dependent density functional theory. Springer: 2012; Vol. 837.
3. Thomas, L. H., "The calculation of atomic fields", *Mathematical Proceedings of the Cambridge Philosophical Society* **1927**, *23*, 542-548.
4. Fermi, E., "Eine statistische Methode zur Bestimmung einiger Eigenschaften des Atoms und ihre Anwendung auf die Theorie des periodischen Systems der Elemente", *Zeitschrift für Physik* **1928**, *48*, 73-79.
5. Burke, K.; Wagner, L. O., "DFT in a nutshell", *International Journal of Quantum Chemistry* **2013**, *113*, 96-101.
6. Teller, E., "On the Stability of Molecules in the Thomas-Fermi Theory", *Reviews of Modern Physics* **1962**, *34*, 627-631.
7. Hohenberg, P.; Kohn, W., "Inhomogeneous Electron Gas", *Physical Review* **1964**, *136*, 864-871.
8. Kohn, W.; Sham, L. J., "Self-Consistent Equations Including Exchange and Correlation Effects", *Physical Review* **1965**, *140*, 1133-1138.
9. Koch, W.; Holthausen, M. C., Bibliography. In *A Chemist's Guide to Density Functional Theory*, Wiley-VCH Verlag GmbH: 2001; pp 265-293.
10. Vosko, S. H.; Wilk, L.; Nusair, M., "Accurate spin-dependent electron liquid correlation energies for local spin density calculations: a critical analysis", *Canadian Journal of Physics* **1980**, *58*, 1200-1211.
11. Lee, C.; Yang, W.; Parr, R. G., "Development of the Colle-Salvetti correlation-energy formula into a functional of the electron density", *Physical Review B* **1988**, *37*, 785-789.
12. Becke, A. D., "Density-functional thermochemistry. III. The role of exact exchange", *Journal of Chemical Physics* **1993**, *98*, 5648-5652.
13. Stephens, P. J.; Devlin, F. J.; Chabalowski, C. F.; Frisch, M. J., "Ab Initio Calculation of Vibrational Absorption and Circular Dichroism Spectra Using Density Functional Force Fields", *The Journal of Physical Chemistry* **1994**, *98*, 11623-11627.
14. Yanai, T.; Tew, D. P.; Handy, N. C., "A new hybrid exchange-correlation functional using the Coulomb-attenuating method (CAM-B3LYP)", *Chemical Physics Letters* **2004**, *393*, 51-57.
15. Tawada, Y.; Tsuneda, T.; Yanagisawa, S.; Yanai, T.; Hirao, K., "A long-range-corrected time-dependent density functional theory", *The Journal of Chemical Physics* **2004**, *120*, 8425-8433.
16. Helgaker, T.; Jørgensen, P.; Olsen, J., *Molecular electronic-structure theory*. Wiley: 2000.
17. Ullrich, C. A., *Time-Dependent Density-Functional Theory: Concepts and Applications*. OUP Oxford: 2012.
18. Runge, E.; Gross, E. K. U., "Density-Functional Theory for Time-Dependent Systems", *Physical Review Letters* **1984**, *52*, 997-1000.
19. van Leeuwen, R., "Mapping from Densities to Potentials in Time-Dependent Density-Functional Theory", *Physical Review Letters* **1999**, *82*, 3863-3866.

20. Maitra, N. T.; Burke, K.; Woodward, C., "Memory in Time-Dependent Density Functional Theory", *Physical Review Letters* **2002**, *89*, 023002.
21. Marques, M. A.; Maitra, N. T.; Nogueira, F. M.; Gross, E. K.; Rubio, A., *Fundamentals of time-dependent density functional theory*. Springer: 2012; Vol. 837.
22. Peach, M. J. G.; Benfield, P.; Helgaker, T.; Tozer, D. J., "Excitation energies in density functional theory: An evaluation and a diagnostic test", *The Journal of Chemical Physics* **2008**, *128*, -.
23. Elliott, P.; Furche, F.; Burke, K., Excited States from Time-Dependent Density Functional Theory. In *Reviews in Computational Chemistry*, John Wiley & Sons, Inc.: 2009; pp 91-165.
24. Burke, K., "Perspective on density functional theory", *The Journal of Chemical Physics* **2012**, *136*, -.
25. Čížek, J., "On the Correlation Problem in Atomic and Molecular Systems. Calculation of Wavefunction Components in Ursell-Type Expansion Using Quantum-Field Theoretical Methods", *The Journal of Chemical Physics* **1966**, *45*, 4256-4266.
26. Čižek, J.; Paldus, J., "Correlation problems in atomic and molecular systems III. Rederivation of the coupled-pair many-electron theory using the traditional quantum chemical methodst", *International Journal of Quantum Chemistry* **1971**, *5*, 359-379.
27. Čížek, J., On the Use of the Cluster Expansion and the Technique of Diagrams in Calculations of Correlation Effects in Atoms and Molecules. In *Advances in Chemical Physics*, John Wiley & Sons, Inc.: 2007; pp 35-89.
28. Christiansen, O.; Koch, H.; Jørgensen, P., "The second-order approximate coupled cluster singles and doubles model CC2", *Chemical Physics Letters* **1995**, *243*, 409-418.
29. Klamt, A.; Schüürmann, G., "COSMO: a new approach to dielectric screening in solvents with explicit expressions for the screening energy and its gradient", *Journal of the Chemical Society, Perkin Transactions 2* **1993**, 799-805.
30. Barone, V.; Cossi, M.; Tomasi, J., "Geometry optimization of molecular structures in solution by the polarizable continuum model", *Journal of Computational Chemistry* **1998**, *19*, 404-417.
31. Kolossváry, I.; Guida, W. C., "Low Mode Search. An Efficient, Automated Computational Method for Conformational Analysis: Application to Cyclic and Acyclic Alkanes and Cyclic Peptides", *Journal of the American Chemical Society* **1996**, *118*, 5011-5019.
32. Jorgensen, W. L.; Tirado-Rives, J., "The OPLS [optimized potentials for liquid simulations] potential functions for proteins, energy minimizations for crystals of cyclic peptides and crambin", *Journal of the American Chemical Society* **1988**, *110*, 1657-1666.

CHAPTER 3:

Predicting PPP's thermodynamic ability to split water

In this chapter, I will present a new computational methodology that was developed in order to model the thermodynamic ability of a molecule, in this case a conjugated polymer, poly(*para*-phenylene) (PPP), modelled as oligo(*p*-phenylene) clusters, to split water into molecular hydrogen and oxygen. More specifically, I will describe and investigate key photochemical properties of oligomers, such as their optical and fundamental gaps, exciton binding energy, ionisation potential and electron affinity, using phenylene as a starting point, that will then be used in the next chapter to consistently screen for new suitable water splitting photocatalysts. The chemical composition and environment of oligophenylenes, as well as their size and topology, will be taken into account.

The content of this chapter has been taken from part of the following published work:

Guiglion P.; Butchosa C.; Zwijnenburg M. A., "Polymeric watersplitting photocatalysts; a computational perspective on the water oxidation conundrum", *J. Mat. Chem. A* **2014**, *2*, 11996-12004.

Guiglion P.; Butchosa C.; Zwijnenburg M. A., "Polymer Photocatalysts for Water Splitting: Insights from Computational Modeling", *Macromol. Chem. Phys.* **2016**, 217, 344-353.

3.1. Motivation and Literature review

In this chapter I discuss a computational method of analysing the thermodynamic ability of materials to act as photocatalysts for water splitting, and apply it to a class of photocatalysts that have recently attracted great attention; organic conjugated polymers.

Chemically, the overall photocatalytic water splitting reaction is the combination of two half-reactions:[1-2]

$$2H^{+}_{(aq)} + 2e^{-} \rightleftarrows H_{2(g)} \quad \text{(A)}$$

$$O_{2(g)} + 4H^{+}_{(aq)} + 4e^{-} \rightleftarrows 2H_2O_{(l)} \quad \text{(B)}$$

As briefly described in Chapter 1, half-reaction (A) runs in the forward direction, the reduction of protons to hydrogen gas, and (B) backwards, the oxidation of water to oxygen gas and protons. In order for both of these half-reactions to take place, a photocatalyst will have to provide electrons for half-reaction (A), and accept electrons, or in other words donate holes, for half-reaction (B). Experimentally, half-reaction (A) has a standard reduction potential of 0 V relative to the Standard Hydrogen Electrode (SHE) and half reaction (B) a standard reduction potential of 1.23 V. A photocatalyst needs therefore to provide at least this amount of potential to split water. In practice, generally, a larger potential (*e.g.* 2 V) is required to overcome kinetic barriers and energetic losses, the difference between the effective and thermodynamic potentials being the overpotential. Another requirement for a successful water splitting photocatalyst is that the (standard) reduction potential of its charge-carriers (electrons, holes) straddle those of half-reactions (A) and (B). In other words, the (standard) reduction potential of its electrons should be more negative than that of the proton reduction half-reaction (A) and the potential of its holes more positive than that of water oxidation half-reaction (B) (see Figure. 3.1).

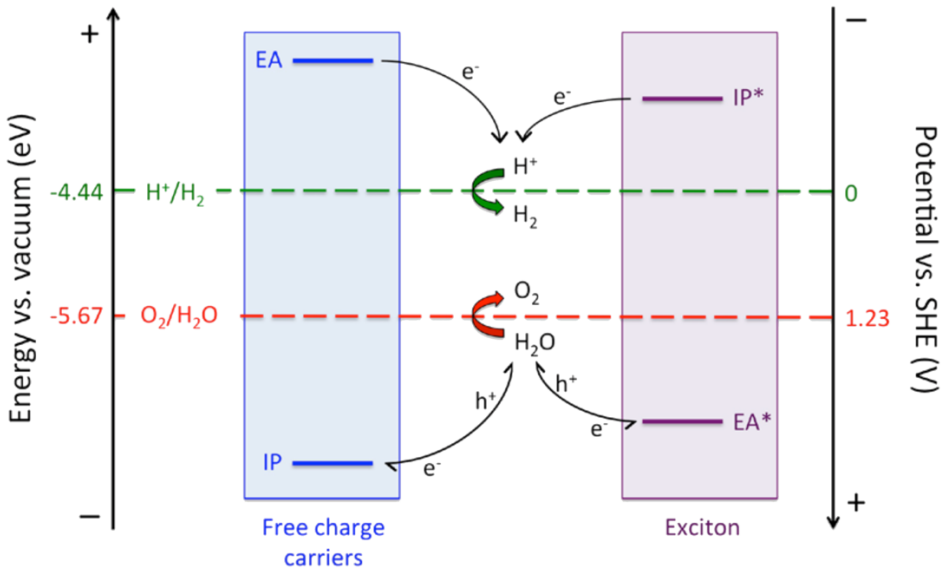

Figure 3.1: Scheme showing how the (standard) reduction potentials of the ideal photocatalyst straddle the proton reduction and water oxidation potentials.[3]

Experimental potential values are given relative to the Standard Hydrogen Electrode (pH = 0). In the scheme, as explained in-depth in the next section, IP refers to the photocatalyst's ground-state adiabatic ionisation potential (the energetic cost of extracting an electron from the top of the photocatalyst's valence band), EA to the ground-state adiabatic electron affinity (the energy released upon adding an electron to the bottom of the photocatalyst's conduction band), IP* the excited-state ionisation potential, and EA* the excited-state electron affinity.

Currently, most polymeric photocatalysts only catalyse the proton reduction half-reaction (A) in the presence of a sacrificial electron donor (*e.g.* methanol or triethylamine) and thus, for the moment, very few can split water as such. Moreover, one of the few polymeric systems in the literature that are reported to split pure water, a carbon nitride polymer with polypyrrole nanoparticles on its surface[4], produces hydrogen and hydrogen peroxide instead of hydrogen and oxygen. In the last two years however, two additional polymeric systems were reported that do split pure water without using any sacrificial reagent; (i) a metal-free carbon nanodot–carbon nitride nanocomposite[5] that splits water *via* a two-step two-electron pathway, oxidising water into hydrogen peroxide, but the carbon nanodots subsequently catalyse the conversion of hydrogen peroxide into molecular oxygen, and (ii) a carbon nitride polymer[6] decorated with *in-situ* photodeposited Pt and PtO_x

that act as co-catalysts for the proton reduction and water oxidation reactions, respectively.

The lack of experimental activity for the water oxidation half-reaction (B) could in principle be thermodynamic in nature, *e.g*. because the (standard) reduction potential of the polymers holes is not sufficiently positive, or alternatively a kinetic issue. In the latter case, a co-catalyst that either lowers the kinetic barriers for water oxidation (*i.e.* reduces the required overpotential) or prevents electron–hole recombination, might turn a polymer that only catalyses half-reaction (A) into one that splits pure water. In contrast, if the lack of activity for reaction (B) is due to thermodynamics, a possible route towards true water splitting would be to use the polymer as a photocathode in combination with an electrical bias and a suitable counter electrode, or as part of a Z-scheme.[7-8]

In order to resolve if the issue with water oxidation for a given polymer is kinetic or thermodynamic in nature, in the Zwijnenburg group, we develop an approach that not only considers the free electron and holes but also the bound exciton (excited electron–hole pair). We also explicitly consider the effect of the environment and the nuclear relaxation associated with localising an excited electron, hole, or exciton (adiabatic potentials versus vertical potentials). I use this approach here primarily to rationalise the lack of water oxidation activity in the original poly(p-phenylene) (PPP) photocatalyst[9-10] of Yanagida and co-workers. I will demonstrate that the holes in PPP thermodynamically cannot drive the oxidation of water, but also suggest that for other systems the problem must be kinetic in nature and should be resolvable with the choice of a suitable co-catalyst.

3.2. Modelling the polymer and sacrificial reagents

3.2.1. Modelling the polymer

In Kohn-Sham DFT, molecular orbitals are one-electron wavefunctions, each associated with a specific energy level. The difference in energy between the Highest Occupied Molecular Orbital (HOMO) and the Lowest Unoccupied Molecular Orbital (LUMO) of a molecule is of particular interest, since it gives an approximation of its optical gap, that is often sufficient. However, it is important to note that what is measured experimentally upon excitation is the difference in energy between the N-electron ground state and the N-electron excited state of the molecule (the real *optical gap*[11]). In that case, the value of the Kohn-Sham band gap yielded by a DFT calculation is of little interest. Moreover, during photocatalysis, the effective energy to be provided by the incident photon must excite one electron, and overcome the electron-hole binding energy: in other terms, it must be equal to, or higher than the molecule's *fundamental gap*[11] (see Figure 3.2).

In other words, one must consider both the ground and excited states in order to assess a conjugated polymer molecule's capability to split water. Instead of relying on a pure HOMO-LUMO picture, the presented computational method introduces several quantities, each associated to a specific electron or hole behaviour:

- the ionisation potential of the ground state, IP, describing how readily an electron can be extracted from the ground-state system (or alternatively, how readily a hole from the ground state can accept an electron from somewhere else),
- the ionisation potential of the exciton, IP*, describing how readily the highest-energy electron from the excited state can be given away,
- the electron affinity of the ground state, EA, describing how readily an additional electron can be added to the ground-state system,
- the electron affinity of the exciton, EA*, describing how readily an additional electron can be added to the excited-state system.

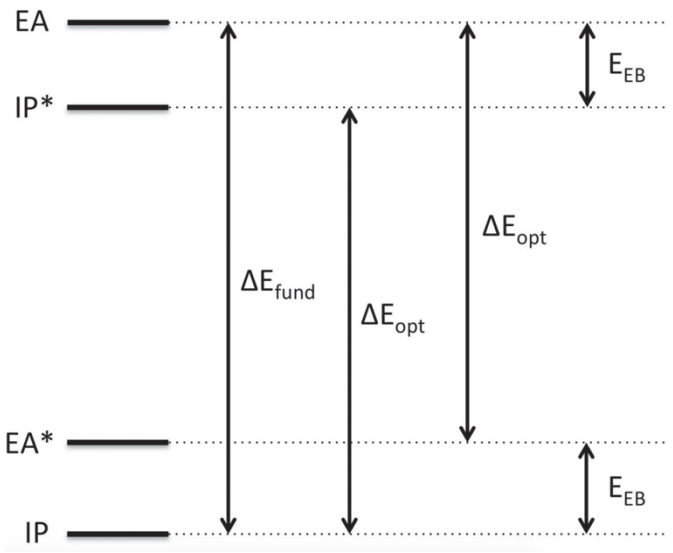

Figure 3.2: Scheme illustrating the connection between the vertical potentials and the fundamental (or band) gap ΔE_{fund} the optical gap ΔE_{opt} and the exciton binding energy E_{EB}.

When considering the ability of a photocatalyst to drive the reduction of protons and the oxidation of water or alternative sacrificial electron donors, there are therefore four redox half-reactions to consider. These half-reactions, written in line with convention as reduction reactions, are:

$$P^+ + e^- \rightleftarrows P^* \quad (C)$$

$$P^* + e^- \rightleftarrows P^- \quad (D)$$

$$P + e^- \rightleftarrows P^- \quad (E)$$

$$P^+ + e^- \rightleftarrows P \quad (F)$$

where P is the neutral photocatalyst, P* the excited photocatalyst (*i.e.* the exciton, a bound excited electron–hole pair), and P^-/P^+ the photocatalyst with a free electron in the conduction band or free hole in the valence band respectively. Free refers here to the fact that the charge carrier in P^-/P^+ does not form part of a neutral exciton. In the remainder of the chapter I will refer to the latter three simply as exciton, free electron and free hole.

In half-reactions (C) and (E) the exciton and free electron act as a reductant; they donate an electron and the half-reaction will run in the opposite direction to that

shown above. In the other two half-reactions the exciton and free hole will act as an oxidant; accepting electrons. Finally, the free electrons and holes responsible for half-reactions (E) and (F) could either be formed as a by-product of half-reactions (C) and (D) or directly by thermal or field ionisation of the exciton:

$$\mathrm{P}^{*} + \mathrm{P} \rightarrow \mathrm{P}^{+} + \mathrm{P}^{-} \tag{G}$$

The free energies of half-reactions (C)–(F) and reaction (G) then are:

$$\Delta\mathrm{G}(C) = \mathrm{G}\left(\mathrm{P}^{*}\right) - \mathrm{G}\left(\mathrm{P}^{+}\right) = -\mathrm{IP}^{*} \tag{1}$$

$$\Delta\mathrm{G}(D) = \mathrm{G}\left(\mathrm{P}^{-}\right) - \mathrm{G}\left(\mathrm{P}^{*}\right) = -\mathrm{EA}^{*} \tag{2}$$

$$\Delta\mathrm{G}(E) = \mathrm{G}\left(\mathrm{P}^{-}\right) - \mathrm{G}(\mathrm{P}) = -\mathrm{EA} \tag{3}$$

$$\Delta\mathrm{G}(F) = \mathrm{G}(\mathrm{P}) - \mathrm{G}\left(\mathrm{P}^{+}\right) = -\mathrm{IP} \tag{4}$$

$$\Delta\mathrm{G}(G) = \left(\mathrm{G}\left(\mathrm{P}^{+}\right) + \mathrm{G}\left(\mathrm{P}^{-}\right)\right) - \left(\mathrm{G}\left(\mathrm{P}^{*}\right) + \mathrm{G}(\mathrm{P})\right) \tag{5}$$

$\Delta\mathrm{G}(E)$ and $\Delta\mathrm{G}(F)$ are equal to negative of the common definition of adiabatic electron affinity and ionisation potential. Similarly, $\Delta\mathrm{G}(C)$ and $\Delta\mathrm{G}(D)$ can be thought of as the negative of the excited state ionisation potential and electron affinity, IP* and EA* respectively (see Figure 3.1).

Finally, the (standard) reduction potentials of the half-reactions can be calculated *via*:

$$\mathrm{E}^{0}(x) = -\frac{\Delta\mathrm{G}(x)}{n\mathrm{F}} \tag{6}$$

where n is the number of electrons involved in the half-reaction and F the Faraday constant. For the polymer, the respective potentials will be labelled as IP, IP*, EA, and EA*.

The Gibbs free energies of each relevant species can be considered as a sum of three contributions:

$$\mathrm{G}(x) = \mathrm{U}(x) + \mathrm{G}_{vib/rot/trans}(x) + \mathrm{G}_{sol}(x) \tag{7}$$

where U is the electronic energy, $G_{vib/rot/trans}$ the contribution to the free energy from vibration, rotation and translation, and G_{sol} the free energy of solvation. One can consider approximations to equation (7) where either or both of the latter terms are ignored. Below, I will comment on the effect of such an approximation.
Another approximation is to model the species in equations (1)–(5) using the ground state geometry of the neutral photocatalyst for all species, *i.e.* ignoring nuclear relaxation. This would be the so-called vertical approximation, yielding vertical potentials, which can be compared with their full adiabatic counterparts. The vertical approximation is not only a numerical simplification but also physically meaningful. Contrasting vertical and adiabatic values allows one to distinguish what would happen if electron transfer was respectively fast or slow compared with nuclear relaxation.

Now, as alluded to in the previous section, for a photocatalyst to be able to thermodynamically drive both the reduction of protons and the oxidation of water, the potentials of half-reactions (D) and (F) (the potentials EA* and IP) should be more positive than the O_2/H_2O reduction potential and the potentials of half-reactions (C) and (E) (the potentials IP* and EA) more negative than the H^+/H_2 reduction potential (see Figure 3.1). For either half-reaction to occur at an appreciable rate, like with any electrochemical reaction, an excess overpotential is usually required; *i.e.* the potentials should be even more positive and negative respectively.

At this point, two important observations need to be made. Firstly, as can be seen on Figure 3.2, the fundamental and optical gaps[11-12] are mirrored in the position of the potentials; the optical gap corresponds to the distance between IP and IP* (or EA and EA*) while the fundamental gap is the distance between IP and EA. Secondly, my calculations intrinsically yield results at pH 0. It can be argued that such a pH is hardly representative of real water splitting conditions, although (photo)electrocatalysis rarely happen at neutral pH, because of conductivity issues. The reason why I chose, in most cases, to show the results at pH 0 is twofold. First, shifting results to pH 7 instead of pH 0 wouldn't affect the main conclusions, qualitatively, as it only shifts the proton reduction and water oxidation potentials by

0.413 V to more negative values (as will be shown later). Quantitatively, it makes proton reduction slightly more difficult to drive, while slightly favouring the oxidation of water. Second, using pH 0 makes water splitting potentials easier to locate, and results easier to visualise, since proton reduction is intuitively positioned at 0 V and water oxidation at 1.23 V (or 1.05 V if taking the computational value instead of the experimental one).

3.2.2. Modelling the potentials of water and sacrificial electron donors

Standard reduction potentials for the reduction of protons, the 4-electron oxidation of water, and the 2-electron oxidation of the sacrificial electron donors methanol and triethylamine (TEA),[13] can be calculated from their respective half-reactions (A), (B), and:

$$CH_2O + 2H^+ + 2e^- \rightarrow CH_3OH \quad \text{(H)}$$

$$NH(CH_2CH_3)_2 + CH_3CHO + 2H^+ + 2e^- \rightarrow N(CH_2CH_3)_3 + H_2O \quad \text{(I)}$$

All these half-reactions involve one or more protons. Calculating the free energy of a proton, however, is rather complicated.[14-15] Following work of others, I thus use the experimentally determined absolute value of the standard hydrogen electrode for the potential of reaction (A) (4.44 V).[16] The proton free-energy ($G(H^+)$), for calculating the potentials of the other half-reactions ((B), (H), (I)) is determined *via*:

$$G(H^+) = \frac{1}{2}G(H_2) - \Delta G(SHE) \quad (8)$$

where $\Delta G(SHE)$ is the free energy of the standard hydrogen electrode (4.44 eV).

Tertiary aliphatic amines, such as TEA, are probably the most used sacrificial electron donors to fuel photochemical reduction reactions, thanks to their degradation pathway, that features a carbon-centered radical with significant reductive power. [17] TEA's 2 electron oxidation is a succession of two monoelectronic oxidation steps: [13, 17] (i) the formation of an aminyl radical, which is then deprotonated and rearranged into a carbon-centred radical, and (ii) the formation

of an iminium species, which in the presence of water is then hydrolysed to form diethylamine (DEA) and acetaldehyde (see Figure 3.3).

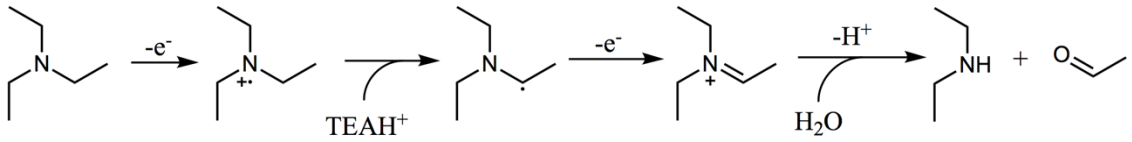

Figure 3.3: Degradation of triethylamine into diethylamine and acetaldehyde, via two 1-electron oxidation steps (TEAH+ refers to protonated TEA).

3.3. Computational methodology

To calculate the photocatalyst potentials outlined in the previous section, in the Zwijnenburg group, we use a combination of DFT,[18-19] for the ground (free) energies including those of the cation and anion, and TD-DFT,[20] for the excited state (free) energies. We use a molecular rather than a periodic approach[21-23] as this conveniently gives us access to the vacuum reference state and allow us to study cation and anions (P^+, P^-) without having to introduce additional approximations, such as a neutralising background charge. The molecular approach is also the natural description of the amorphous polymeric photocatalysts studied below, with excited states delocalised over a finite number of polymer units.

My calculations consist effectively of four major steps. First, I perform a conformational search using an interatomic potential to find the lowest energy conformers. Second, I optimise the geometries of these conformers using DFT for its neutral (P), cationic (P^+) and anionic state (P^-). Third, I optimise the geometry of the conformer in its lowest singlet excited state (S1) using TD-DFT (P*). Fourth, I calculate the vibrational spectra for all four minimum energy geometries (P, P^+, P^- and P*) to determine the vibrational, rotational and translational contributions to the free energy; $G_{vib/rot/trans}(x)$ in equation (7). A similar set-up is used to calculate the standard reduction potentials of water and the sacrificial electron donors, except for the lack of a conformer search and no need of TD-DFT calculations.

The effect of the solvent, and the environment in general, is included in all calculations, except where explicitly stated, by using the COSMO dielectric continuum solvation model,[24-25] allowing me to estimate the $G_{sol}(x)$ term in equation (7). I consider both single point COSMO calculations on the gas phase minimum energy structures and full COSMO geometry optimisations, except in the case of TD-DFT calculations, where no COSMO gradients are available in the code used, and for which hence only the former option is available. Within the COSMO model, the properties of the environment are characterised by its relative dielectric permittivity (ε_r). Calculations for the polymers are performed for a range of 3 values

(ε_r = 1, 5, 30 and 80.1), while the standard reduction potentials of water and the sacrificial electron donors are only calculated for the case of ε_r = 80.1 (solvation in water).

For the initial conformational search, the OPLS-2005 force-field[26] and the low-mode sampling algorithm[27] as implemented in MacroModel 9.9 (ref. [28]) are employed. I typically used a combination of 10000 search steps and minimum and maximum low-mode move distances of 3 and 6 Å respectively. All the structures located within an energy window of 100 kJ/mol relative to the lowest energy conformer are saved.

All the DFT and TD-DFT calculations employ the B3LYP[29-32] hybrid Exchange–Correlation (XC) functional and the Turbomole 6.5 code.[33-35] The standard basis-set used is the double-ζ DZP[36] basis set, but for selected calculations also the larger def2-TZVP[37] basis-set is employed. In all TD-DFT calculations, I use the Tamm–Dancoff[38] approximation.

Finally, for selected systems, Peach's Λ diagnostic[39] is calculated. The Λ diagnostic characterises the overlap between the occupied and unoccupied orbitals involved with an excitation, and the likeliness that this excitation is wrongly described in TD-DFT due to it having a charge-transfer (CT) nature. The Λ scale ranges from 0 (no overlap, CT-excitation) to 1 (full overlap, fully local excitation), and for excitations with Λ > 0.3, TD-B3LYP has been found to normally not suffer from any CT-problems.[39] The Λ values obtained, typically 0.4–0.8, suggest that CT-problems are unlikely to be an issue in the TD-B3LYP excited state description of any of the systems studied here.

3.4. Results and discussion

3.4.1. PPP model and its optical properties

In the follow-up to the original paper of Yanagida and co-workers,[9] Shibata *et al.*[10] estimate that the photocatalytically active PPP material consists approximately of *p*-phenylene chains of 7 and 11 phenylene units (see below). Hence in my calculations, I primarily focus on these molecules, hereafter referred to as PPP-7 and PPP-11. Figure 3.3 shows a picture of the DFT optimised structure of the lowest energy conformer of PPP- 7. To probe the effect of chain length I will also contrast the properties of these longer chains with those of the p-phenylene dimer, PPP-2.

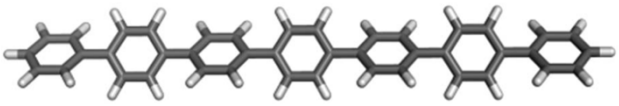

Figure 3.4: B3LYP optimised structure of PPP-7.

Before discussing my prediction for the (standard) reduction potentials of the exciton and the free charge carriers, I first compare the predicted absorption onset and luminescence signal of PPP-7 and PPP-11 with experimental data for PPP powder samples from the literature. Different authors[10, 40] report slightly different powder absorption spectra for PPP. These differences probably arise from slight variations in the PPP chain-length distributions obtained during synthesis, and from the experimental difficulty in characterising this chain-length distribution due to the poor solubility of PPP oligomers and polymers in common solvents. In the case of the PPP samples of Shibata and co-workers,[10] the fact that both the PPP-7 and PPP-11 samples have a similar absorption onset (see Fig. 2B in their paper) and the fact that the fluorescence spectrum they obtain for PPP-11 is bimodal (see their Fig. 3) suggest that both samples most likely contain a distribution of PPP chain lengths. The experimental labels PPP-7 and PPP-11, while probably representative, are hence likely to be a slight simplification of the true complexity of the experimental samples.

When comparing experimental spectra with TD-DFT predicted excitation energies, I make, following previous work in the Zwijnenburg group,[41-43] the implicit assumption that the top of the first peak or shoulder in the absorption spectrum equals the experimental vertical absorption onset, and that all absorption before this peak arises from vibrational broadening. For the small oligomers, one could assume that the lowest vertical singlet-singlet excitation energy (LVEE) would coincide with the maximum of the first absorption peak and that all experimental absorption intensity at lower energy (in other words between the experimental onset of light absorption, *i.e.* the optical gap, and the first peak maximum) would be due to vibrational broadening. For longer oligomers, and the polymer, the match might be more complicated due to inhomogeneous broadening and scattering.

As can be seen from Table 3.1, upon making this assumption, TD-B3LYP yields a good match to the experimental data. In line with the literature, adding a dielectric embedding to model the polymer matrix around the chains (assumed to have $\varepsilon_r = 5$) changes the results only marginally.

	Absorption on-set	Fluorescence
TD-B3LYP PPP-7	340 (350)	430 (440)
TD-B3LYP PPP-11	360 (370)	450 (460)
Experiment	~360[a]–400[b]	~460/490[c]

[a] From ref. 49 for PPP chains of on 7 units or more. [b] From ref. 22 for PPP-7 and 11 (based on top of plateau in Fig. 2B). [c] From ref. 22 for PPP-11 (Fig. 3).

Table 3.1: Comparison between the experimental and TD-B3LYP predicted optical properties of PPP-7 and PPP-11. All values given in nm, and $\varepsilon_r = 5$ TD-DFT COSMO results shown in parentheses.

3.4.2. Probing the influence of the environment

While the effect of dielectric embedding is small in the case of the predicted optical spectra, this is not the case for the calculated reduction potentials of the exciton and the free charge carriers. Focusing first on the standard reduction potentials of the free electrons (EA), Figure 3.4 shows that in PPP-7 the EA potential becomes more

positive by approximately 1 V when going from the gas phase (ε_r = 1) to a PPP chain surrounded by water (ε_r = 80.1). The change is far from linear with respect to the relative dielectric permittivity. The predicted standard reduction potential in a methanol environment (ε_r= 30), the solvent used by Shibata and co-workers[10], is very similar to that predicted for water, while the ε_r = 5 result lies numerically much closer to that obtained for water than that predicted for the gas phase. The standard reduction potential of the free holes (IP) becomes more negative upon embedding PPP, but again the shift is in the order of 1 V. As a result of these shifts, the thermodynamic ability of the polymer, or photocatalyst in general, will change with the environment it is embedded in.

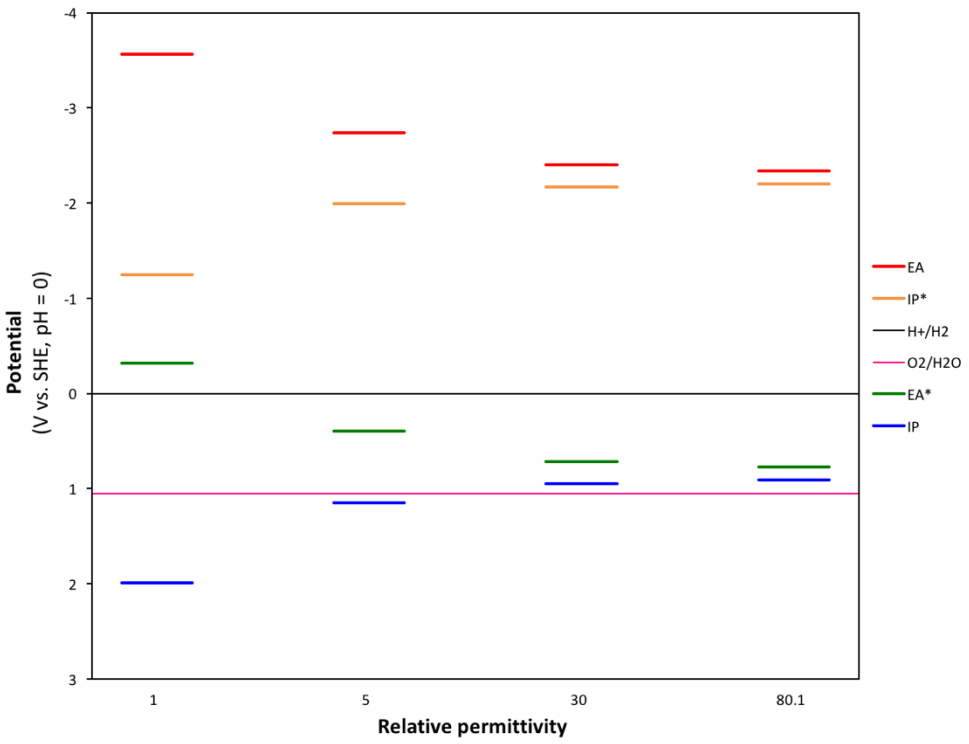

Figure 3.5: The (TD-)B3LYP predicted IP, EA, IP and EA* adiabatic potential values of PPP-7 at pH 0 as function of the dielectric permittivity of the embedding medium (water oxidation and proton reduction potentials calculated with ε_r = 80.1).*

The standard reduction potentials involving the exciton (EA* and IP*) show similar behaviour. Upon increasing the relative dielectric permittivity of the environment, the standard reduction potential of the reaction where the exciton donates an electron (IP*), becomes more negative and the standard reduction potential of the reaction where the exciton accepts an electron (EA*) becomes more positive. The

difference in potential between EA and IP* and between IP and EA* becomes progressively smaller, approaching zero for water (0.2 eV). For PPP-7 embedded in water, less than 10 kT of additional energy (at room temperature) needs to be provided to ionise the exciton into free charge carriers (compared with more than 100 kT for the gas phase). Splitting the exciton, required for chemistry involving the free charge carriers, is thus predicted to be much easier in a high dielectric permittivity environment, even if still unlikely (see next section and Table 3.3).

The large shifts in predicted potentials with changes in the relative dielectric permittivity of the environment in which the PPP polymer is embedded make physical sense. All potentials involve charged species, the free charge carriers, and those charged species are to a much larger degree stabilised energetically by the dielectric embedding than their neutral counterparts. The predicted adiabatic potentials in Figure 3.4 neglect the contribution of $G_{vib/rot/trans}$ in equation (7). Data including $G_{vib/rot/trans}$ (see Table 3.2) shows that neglecting it generally results in changes of the order of 0.1 V in the predicted potentials. Ignoring nuclear relaxation, using vertical rather than adiabatic potentials, would introduce a larger error (0.2–0.3 V, see Table 3.2). In the remainder of this chapter, all polymer potentials discussed will be adiabatic potentials calculated for an aqueous environment (ε_r = 80.1), where $G_{vib/rot/trans}$ is neglected.

	Vertical	Adiabatic	Adiabatic+G_{vib}
EA	-2.57	-2.35	-2.27
IP	1.08	0.93	0.97
EA*	0.96	0.75	0.75
IP*	-2.45	-2.17	-2.05

Table 3.2: Vertical, adiabatic, and free energy ($G_{vib/rot/trans}$) corrected potentials of PPP-7 in water at pH = 0, calculated with (TD-)B3LYP/DZP and the COSMO solvation model (ε_r = 80.1). All values in Volt.

3.4.3. Exciton dissociation

Commonly, when studying photocatalysis, people only focus on processes involving free charge carriers (*i.e.* half reactions (E) and (F) as introduced in section 3.2), implicitly assuming that excitons spontaneously dissociate and that the exciton binding energy is negligible. While this is a fair assumption for many inorganic semiconductors, for which experimentally measured exciton binding energies are only in the order of tens of meV, this is not necessarily the case for polymers. For example, for PPP, the vertical exciton binding energy (ignoring nuclear relaxation as a result of localising a hole, electron or exciton on the polymer) is predicted to be ≈ 1200 meV in the middle of a polymer matrix and ≈ 170 meV on or near the interface with water (see Table 3.3). The difference between the exciton binding energies in the two scenarios arises from the fact that dielectric screening of free charges is larger in water (ε_r = 80.1) than in polymer (ε_r ≈ 2). Such exciton binding energy values are much larger than kT at room temperature (26 meV) suggesting that excitons do not spontaneously dissociate in these polymers. Going from the vertical to the adiabatic picture, where nuclear relaxation is taken into account, does not change this picture, except near the interface with water, for materials made of very short oligomers, where calculations suggest that exciton dissociation might be spontaneous.

	vacuum	polymer	water
PPP-6	2.47	1.6	0.14
PPP-12	1.96	1.36	0.24

Table 3.3: TD-B3LYP predicted exciton binding energy values for PPP-6 and PPP-12 in three different environments: vacuum (ε_r =1), polymer (ε_r = 2) and water (ε_r = 80.1).

Aside from the case of "bulk" exciton dissociation discussed above, where both the free electron and free hole remain in the same phase after dissociation, although far apart, excitons can also dissociate on the interface between two phases. This could be on the interface between different solid phases, which together form the photocatalyst, as exploited in photocatalytic heterostructures, or on the interface between the photocatalyst and the aqueous solution.[44] In both cases, one of the free

charge carriers remains in the phase where the exciton was originally generated, while the other gets transferred to the other phase, and in the case of exciton dissociation on the photocatalyst–solution interface, is subsequently consumed by a solution redox reaction (see Figure 3.5).

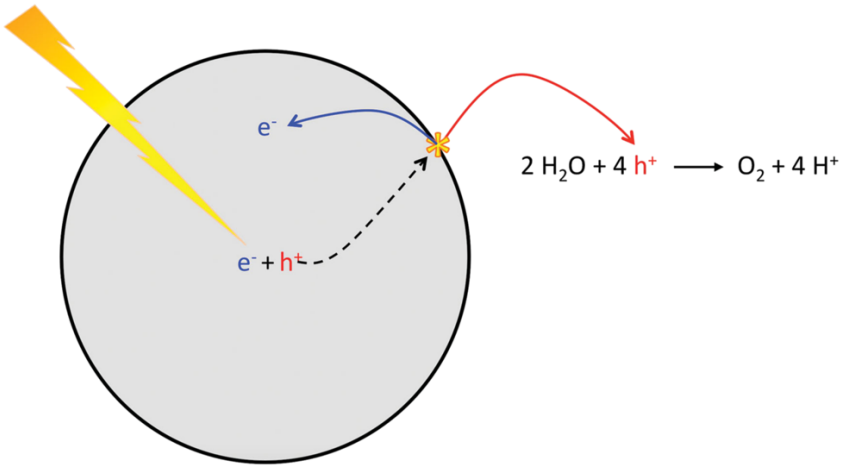

Figure 3.6: Illustration of exciton dissociation at the surface of a polymer particle for the case where the hole of the exciton goes into solution, where it drives water oxidation, while the electron remains on the particle.

For example, the free hole can be transferred to the solution and take part in the oxidation of water (half reaction (B)) or that of a sacrificial electron donor, while the free electron can remain on the photocatalyst, and subsequently reduce a proton (half reaction (A)). For many polymers/oligomers, for example PPP, this is the case for either pure water or the combination of water and a SED. The photocatalytic activity of such polymers can then be understood from a thermodynamic point of view as resulting from excitons dissociating at the polymer–solution interface, driving one of the solution half reactions, and generating free charge carriers in the process, to drive the other solution half-reaction.

This observation, that excitons in conjugated polymers should be so strongly bound that they are unlikely to spontaneously fall apart in the bulk, is confirmed experimentally (see section 4.3 of Chapter 4 for an estimate of the experimental adiabatic exciton-binding energy in P3HT and PPV). From the difference in the measured electron affinity[45-47] and two-photon photoelectron spectroscopy (2PPE)

intermediate state energy[45-46], their exciton binding energy is estimated to be as high as ~0.7 (e)V.

The importance of the polymer–water interface in exciton dissociation suggests that a high surface area is a desirable property for a polymer photocatalyst to have, and should result in better quantum efficiencies. As such, photocatalysts based on conjugated microporous polymers[48] and covalent organic frameworks,[49-50] with large internal surface areas because of their porosity, as will be discussed in Chapter 5, might be an attractive proposition.

3.4.4. Understanding the effect of oligomer length

Figure 3.6 compares the standard reduction potentials predicted for PPP-7, PPP-11 and the PPP-2 dimer, in water. Clearly the differences between PPP-7 and PPP-11 are relatively small, while, in contrast, the potentials of PPP-2 are significantly different. Overall, the potentials in which the polymer accepts electrons (IP and EA*) become more negative with chain length, while potentials in which the polymer donates electrons (EA and IP*) become more positive.

These trends are linked to the fact that PPP is a conjugated polymer, with a finite conjugation length, calculated below. The absorption onset values (modelled as the LVEE) of the infinite chain were determined by performing a least squares fit of the TD-B3LYP predicted absorption onset values to the equations developed by Meier *et al.*:[51]

$$E(n) = E(\infty) + \left[E(1) - E(\infty)\right]e^{-a(n-1)} \quad \text{(i)}$$

$$\lambda(n) = \lambda(\infty) - \left[\lambda(\infty) - \lambda(1)\right]e^{-b(n-1)} \quad \text{(ii)}$$

where $E(\infty)$ and $\lambda(\infty)$ are the absorption onset of the infinite chain (in eV and nm respectively), $E(1)$ and $\lambda(1)$ the absorption onset of the monomer (benzene), and a and b numerical constants.

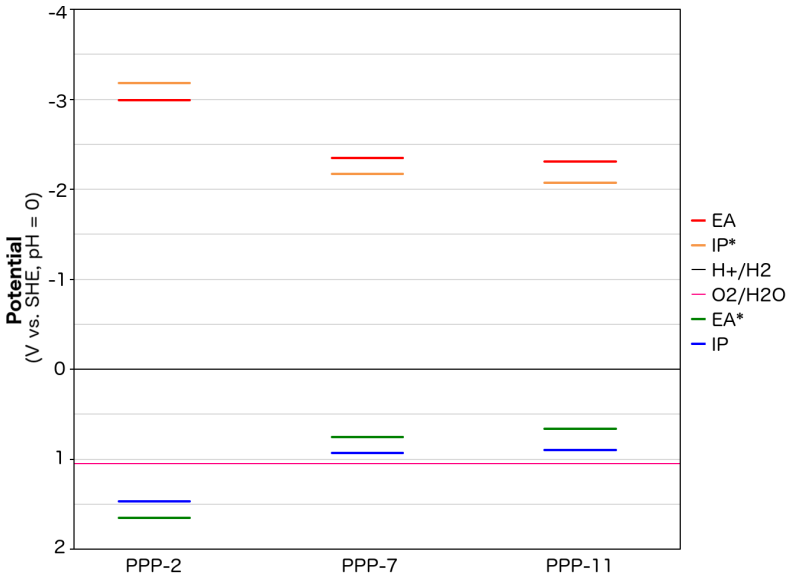

Figure 3.7: Comparison of the predicted IP, EA, IP and EA* adiabatic potential values of PPP-2, PPP-7 and PPP-11 in water (ε_r = 80.1) at pH 0.*

Following Meier, the conjugation length is here defined as the value of n for which λ(n) differs from λ(∞) by less than 1 nm, yielding a conjugation length value of 22 for PPP, which is rather long. The 1 nm value is, however, to a certain degree arbitrary, and it should be noted that, as can be seen from Figure 3.7, the difference of the absorption onset of PPP-11 and the infinite chain is of the order of only 0.05 eV. Additionally, while conjugation length may be a useful concept for linear conjugated polymers, it might not be as well defined or meaningful for real polymeric materials, due to molecular chain bending, entanglement, or crosslinking.

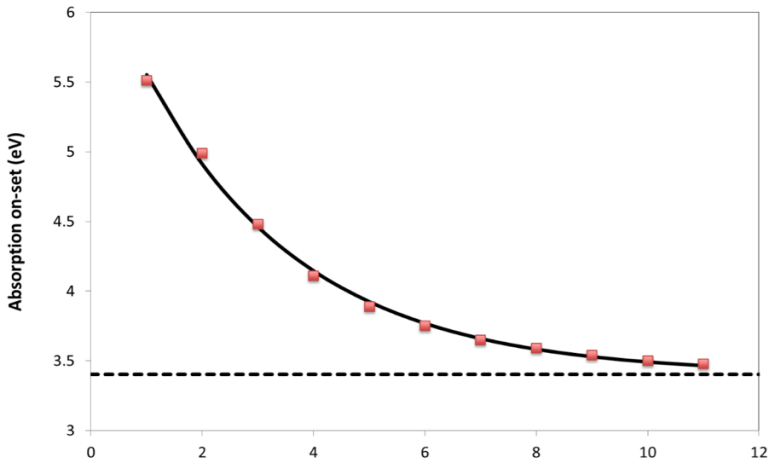

Figure 3.8: TD-B3LYP/DZP predicted absorption onset values of PPP in eV as a function of the number of phenylene units in the chain. The dashed line indicates the fitted absorption onset of an infinite PPP chain.

3.4.5. Assessing the water splitting potential of PPP

Using the potentials shown on Figure 3.6, I can now shed light on the ability of the different PPP oligomers to split water. These potentials are strictly speaking for a solution of pH 0, because $G(H^+)$ is calculated from the experimental SHE potential. The Nernst equation can be used to correct these results, where the polymer potentials relative to vacuum stay fixed, but all the water and sacrificial electron donor potentials that involve H^+ shift by 0.059 V per pH unit, to more experimentally relevant pH values. Figure 3.8 shows the situation for pH values of 7 (neutral water) and 10 (the likely pH of the methanol–triethylamine–water solutions used in the work of Shibata and co-workers, see Table 3.4 for the numerical values of the predicted potentials at the different pH values). It is clear from the figures that for the pH range studied, there is a strong thermodynamic driving force for proton reduction by both the free electron and the exciton. These results suggest that the exciton does not need to be split in order for photocatalysis to take place, as the exciton itself can thermodynamically reduce protons. This is an important observation, since in polymers there is less likely to be a space charge layer to split excitons through field ionisation. The situation for water oxidation is substantially different. At pH 0, water oxidation by both the free hole and the exciton is endothermic, while at pH 7 and 10 there is only a marginal driving force for the oxidation reaction to proceed. Based on these results, pure water splitting is thus unlikely to happen in the absence of some external electrical bias. Alternatively, PPP might find use as part of a Z-scheme.[7-8]

Figure 3.8 also includes the predicted potentials for the 2-electron oxidation of methanol and triethylamine (reactions (H) and (I)). Clearly there is a thermodynamic driving force for the oxidation of both by PPP-7 and PPP-11. The driving force is largest for triethylamine, in line with the results of Shibata and co-workers, where its use gave the highest hydrogen yield. The two expected products of the 2-electron oxidation of triethylamine (ethanol, produced through photoreduction of acetaldehyde, see equation (I) in section 3.2, and diethylamine) are indeed observed by Shibata and co-workers to be produced in conjunction with

hydrogen.[10] The success of triethylamine as a sacrificial electron donor is probably due to its more negative potential than that of water, combined with the fact it involves a 2- rather than a 4-electron reaction.

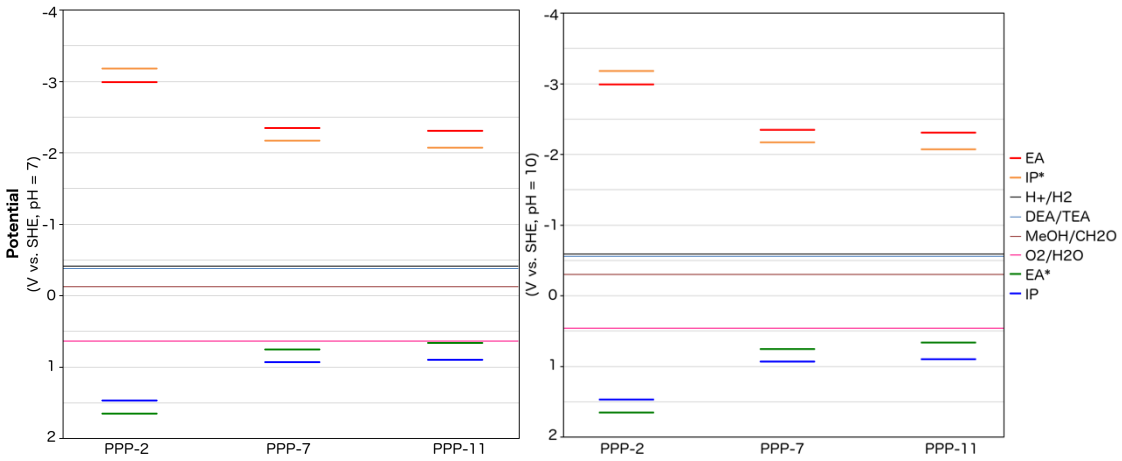

Figure 3.9: Predicted potentials of PPP at pH 7 (left side) and 10 (right side). The potentials of the 2-electron oxidation of triethylamine (TEA) and methanol are also shown (blue and brown lines respectively).

	pH 0	pH 7	pH 10
O_2/H_2O	1.05	0.64	0.46
H_2O/H_2O_2	1.64	1.23	1.05
TEA	0.03	-0.38	-0.56
MeOH	0.29	-0.12	-0.30

Table 3.4: Effect of the pH on the adiabatic and free energy ($G_{vib/rot/trans}$) corrected potentials of water, hydrogen peroxide and sacrificial electron donors (triethylamine and methanol). Potentials calculated using B3LYP/DZP and the COSMO solvation model (ε_r = 80.1). All potential values in Volt.

All results discussed here were obtained using the DZP basis-set. Some of the potentials for the polymer and all of the solution reaction potentials (reactions (A), (B), (H) and (I), see Table 3.5) were recalculated with the larger def2-TZVP basis; the effect of increasing the basis-set was found to be generally small. The most noticeable change was an even better agreement of the calculated standard reduction potential of water oxidation (1.05 V for DZP and 1.21 V for def2-TZVP) with its experimental value. Finally, while $G_{vib/rot/trans}$ is neglected for the polymer, it is always included when calculating the solution reaction potentials. Due to the structural differences between reactants and products, the effect of neglecting $G_{vib/rot/trans}$ would be substantially bigger here.

	DZP	def2-TZVP	def2-QZVP
O_2/H_2O	1.05	1.21	1.26
H_2O/H_2O_2	1.64	1.85	1.91
TEA	0.03	0.09	
MeOH	0.29	0.25	

Table 3.5: Basis-set effects on adiabatic and free energy ($G_{vib/rot/trans}$) corrected standard reduction potentials of water, hydrogen peroxide and sacrificial electron donors. Calculated using B3LYP (all values in V, pH = 0)

3.5. Conclusions

Using a newly developed computational approach, I probed the thermodynamic ability of a polymeric water splitting photocatalysts, PPP, to drive both the reduction of protons and the oxidation of water. Some optical properties of PPP were calculated and compared to experimental data. I took into consideration the effect of the chemical environment around PPP, and discussed the effect of increasing its oligomer length on the predicted IP, EA, IP* and EA* potentials.

Calculations strongly suggest (and it is confirmed experimentally) that, while this material can drive the oxidation of protons into hydrogen gas, in the presence of a sacrificial electron donor, it remains thermodynamically unable to oxidise water and hence split pure water. It is important to note that in PPP (and more generally for similar types of conjugated oligomers/polymers) according to calculations, excitons do not spontaneously dissociate, and are able to drive one electronic half-reaction on their own, as they dissociate at an interface, similar to exciton dissociation in organic photovoltaics on the donor–acceptor interface,[52] and generate free charge carriers.

The presented computational method proves its value as a tool to systematically study polymeric systems of interest, in the quest for an overall water splitting photocatalyst, in a rather computationally inexpensive way. After validating it in the next chapter, it will be used in Chapter 5 to carry out a broad screening among various types of chemical systems, and its predictive performance will be assessed.

3.6. References

1. Maeda, K.; Domen, K., "Photocatalytic Water Splitting: Recent Progress and Future Challenges", *The Journal of Physical Chemistry Letters* **2010**, *1*, 2655-2661.
2. Hisatomi, T.; Kubota, J.; Domen, K., "Recent advances in semiconductors for photocatalytic and photoelectrochemical water splitting", *Chemical Society Reviews* **2014**,
3. Guiglion, P.; Berardo, E.; Butchosa, C.; Wobbe, M. C. C.; Zwijnenburg, M. A., "Modelling materials for solar fuel synthesis by artificial photosynthesis; predicting the optical, electronic and redox properties of photocatalysts", *Journal of Physics: Condensed Matter* **2016**, *28*, 074001.
4. Sui, Y.; Liu, J.; Zhang, Y.; Tian, X.; Chen, W., "Dispersed conductive polymer nanoparticles on graphitic carbon nitride for enhanced solar-driven hydrogen evolution from pure water", *Nanoscale* **2013**, *5*, 9150-9155.
5. Liu, J.; Liu, Y.; Liu, N.; Han, Y.; Zhang, X.; Huang, H.; Lifshitz, Y.; Lee, S.-T.; Zhong, J.; Kang, Z., "Metal-free efficient photocatalyst for stable visible water splitting via a two-electron pathway", *Science* **2015**, *347*, 970.
6. Zhang, G.; Lan, Z.-A.; Lin, L.; Lin, S.; Wang, X., "Overall water splitting by Pt/g-C3N4 photocatalysts without using sacrificial agents", *Chemical Science* **2016**, *7*, 3062-3066.
7. Bard, A. J., "Photoelectrochemistry and heterogeneous photo-catalysis at semiconductors", *Journal of Photochemistry* **1979**, *10*, 59-75.
8. Maeda, K., "Z-Scheme Water Splitting Using Two Different Semiconductor Photocatalysts", *ACS Catalysis* **2013**, *3*, 1486-1503.
9. Yanagida, S.; Kabumoto, A.; Mizumoto, K.; Pac, C.; Yoshino, K., "Poly(p-phenylene)-catalysed photoreduction of water to hydrogen", *Journal of the Chemical Society, Chemical Communications* **1985**, 474-475.
10. Shibata, T.; Kabumoto, A.; Shiragami, T.; Ishitani, O.; Pac, C.; Yanagida, S., "Novel visible-light-driven photocatalyst. Poly(p-phenylene)-catalyzed photoreductions of water, carbonyl compounds, and olefins", *Journal of Physical Chemistry* **1990**, *94*, 2068-2076.
11. Brédas, J.-L., "Mind the gap!", *Materials Horizons* **2014**, *1*, 17-19.
12. Guiglion, P.; Butchosa, C.; Zwijnenburg, M. A., "Polymer Photocatalysts for Water Splitting: Insights from Computational Modeling", *Macromolecular Chemistry and Physics* **2016**, *217*, 344-353.
13. Portis, L. C.; Bhat, V. V.; Mann, C. K., "Electrochemical dealkylation of aliphatic tertiary and secondary amines", *The Journal of Organic Chemistry* **1970**, *35*, 2175-2178.
14. Zhan, C.-G.; Dixon, D. A., "Absolute Hydration Free Energy of the Proton from First-Principles Electronic Structure Calculations", *The Journal of Physical Chemistry A* **2001**, *105*, 11534-11540.
15. Bryantsev, V. S.; Diallo, M. S.; Goddard III, W. A., "Calculation of Solvation Free Energies of Charged Solutes Using Mixed Cluster/Continuum Models", *The Journal of Physical Chemistry B* **2008**, *112*, 9709-9719.

16. Trasatti, S., "The absolute electrode potential: an explanatory note (Recommendations 1986)", *Journal of Electroanalytical Chemistry and Interfacial Electrochemistry* **1986**, *209*, 417-428.
17. Pellegrin, Y.; Odobel, F., "Sacrificial electron donor reagents for solar fuel production", *Comptes Rendus Chimie* **2017**, *20*, 283-295.
18. Hohenberg, P.; Kohn, W., "Inhomogeneous Electron Gas", *Physical Review* **1964**, *136*, 864-871.
19. Kohn, W.; Sham, L. J., "Self-Consistent Equations Including Exchange and Correlation Effects", *Physical Review* **1965**, *140*, 1133-1138.
20. Runge, E.; Gross, E. K. U., "Density-Functional Theory for Time-Dependent Systems", *Physical Review Letters* **1984**, *52*, 997-1000.
21. Castelli, I. E.; Olsen, T.; Datta, S.; Landis, D. D.; Dahl, S.; Thygesen, K. S.; Jacobsen, K. W., "Computational screening of perovskite metal oxides for optimal solar light capture", *Energy & Environmental Science* **2012**, *5*, 5814-5819.
22. Wu, Y.; Lazic, P.; Hautier, G.; Persson, K.; Ceder, G., "First principles high throughput screening of oxynitrides for water-splitting photocatalysts", *Energy & Environmental Science* **2013**, *6*, 157-168.
23. Stevanovic, V.; Lany, S.; Ginley, D. S.; Tumas, W.; Zunger, A., "Assessing capability of semiconductors to split water using ionization potentials and electron affinities only", *Physical Chemistry Chemical Physics* **2014**, *16*, 3706-3714.
24. Klamt, A.; Schüürmann, G., "COSMO: a new approach to dielectric screening in solvents with explicit expressions for the screening energy and its gradient", *Journal of the Chemical Society, Perkin Transactions 2* **1993**, 799-805.
25. Barone, V.; Cossi, M.; Tomasi, J., "Geometry optimization of molecular structures in solution by the polarizable continuum model", *Journal of Computational Chemistry* **1998**, *19*, 404-417.
26. Jorgensen, W. L.; Tirado-Rives, J., "The OPLS [optimized potentials for liquid simulations] potential functions for proteins, energy minimizations for crystals of cyclic peptides and crambin", *Journal of the American Chemical Society* **1988**, *110*, 1657-1666.
27. Kolossváry, I.; Guida, W. C., "Low Mode Search. An Efficient, Automated Computational Method for Conformational Analysis: Application to Cyclic and Acyclic Alkanes and Cyclic Peptides", *Journal of the American Chemical Society* **1996**, *118*, 5011-5019.
28. Mohamadi, F.; Richards, N. G. J.; Guida, W. C.; Liskamp, R.; Lipton, M.; Caufield, C.; Chang, G.; Hendrickson, T.; Still, W. C., "Macromodel—an integrated software system for modeling organic and bioorganic molecules using molecular mechanics", *Journal of Computational Chemistry* **1990**, *11*, 440-467.
29. Vosko, S. H.; Wilk, L.; Nusair, M., "Accurate spin-dependent electron liquid correlation energies for local spin density calculations: a critical analysis", *Canadian Journal of Physics* **1980**, *58*, 1200-1211.
30. Lee, C.; Yang, W.; Parr, R. G., "Development of the Colle-Salvetti correlation-energy formula into a functional of the electron density", *Physical Review B* **1988**, *37*, 785-789.

31. Becke, A. D., "Density-functional thermochemistry. III. The role of exact exchange", *Journal of Chemical Physics* **1993**, *98*, 5648-5652.
32. Stephens, P. J.; Devlin, F. J.; Chabalowski, C. F.; Frisch, M. J., "Ab Initio Calculation of Vibrational Absorption and Circular Dichroism Spectra Using Density Functional Force Fields", *The Journal of Physical Chemistry* **1994**, *98*, 11623-11627.
33. Ahlrichs, R.; Bär, M.; Häser, M.; Horn, H.; Kölmel, C., "Electronic structure calculations on workstation computers: The program system turbomole", *Chemical Physics Letters* **1989**, *162*, 165-169.
34. Furche, F.; Ahlrichs, R., "Erratum: Time-dependent density functional methods for excited state properties", *The Journal of Chemical Physics* **2004**, *121*, 12772-12773.
35. van Wüllen, C., "Shared-memory parallelization of the TURBOMOLE programs AOFORCE, ESCF, and EGRAD: How to quickly parallelize legacy code", *Journal of Computational Chemistry* **2011**, *32*, 1195-1201.
36. Schafer, A.; Horn, H.; Ahlrichs, R., "Fully optimized contracted Gaussian basis sets for atoms Li to Kr", *The Journal of Chemical Physics* **1992**, *97*, 2571-2577.
37. Weigend, F.; Ahlrichs, R., "Balanced basis sets of split valence, triple zeta valence and quadruple zeta valence quality for H to Rn: Design and assessment of accuracy", *Physical Chemistry Chemical Physics* **2005**, *7*, 3297-3305.
38. Hirata, S.; Head-Gordon, M., "Time-dependent density functional theory within the Tamm-Dancoff approximation", *Chemical Physics Letters* **1999**, *314*, 291-299.
39. Peach, M. J. G.; Benfield, P.; Helgaker, T.; Tozer, D. J., "Excitation energies in density functional theory: An evaluation and a diagnostic test", *The Journal of Chemical Physics* **2008**, *128*, -.
40. Froyer, G.; Goblot, J., Y.; Guilbert, J., L.; Maurice, F.; Pelous, Y., "POLY(PARA PHENYLENE) : SOME PROPERTIES RELATED TO THE SYNTHESIS METHOD", *J. Phys. Colloques* **1983**, *44*, 745-748.
41. Zwijnenburg, M. A., "Elucidating the Microscopic Origin of the Unique Optical Properties of Polypyrene", *The Journal of Physical Chemistry C* **2012**, *116*, 20191-20198.
42. Zwijnenburg, M. A.; Cheng, G.; McDonald, T. O.; Jelfs, K. E.; Jiang, J. X.; Ren, S. J.; Hasell, T.; Blanc, F.; Cooper, A. I.; Adams, D. J., "Shedding Light on Structure-Property Relationships for Conjugated Microporous Polymers: The Importance of Rings and Strain", *Macromolecules* **2013**, *46*, 7696-7704.
43. Butchosa, C.; McDonald, T. O.; Cooper, A. I.; Adams, D. J.; Zwijnenburg, M. A., "Shining a Light on s-Triazine-Based Polymers", *The Journal of Physical Chemistry C* **2014**, *118*, 4314-4324.
44. Berardo, E.; Zwijnenburg, M. A., "Modeling the Water Splitting Activity of a TiO2 Rutile Nanoparticle", *The Journal of Physical Chemistry C* **2015**, *119*, 13384-13393.
45. Sohn, Y.; Stuckless, J. T., "Bimolecular recombination kinetics and interfacial electronic structures of poly[2-methoxy-5-(2-ethyl-hexyloxy)-p-phenylene vinylene] on gold studied using two-photon photoemission spectroscopy", *The Journal of Chemical Physics* **2007**, *126*, 174901.

46. Sohn, Y.; Stuckless, J. T., "Characteristics of Photoexcitations and Interfacial Energy Levels of Regioregular Poly(3-hexythiophene-2,5-diyl) on Gold", *ChemPhysChem* **2007**, *8*, 1937-1942.
47. Kanai, K.; Miyazaki, T.; Suzuki, H.; Inaba, M.; Ouchi, Y.; Seki, K., "Effect of annealing on the electronic structure of poly(3-hexylthiophene) thin film", *Physical Chemistry Chemical Physics* **2010**, *12*, 273-282.
48. Sprick, R. S.; Jiang, J.-X.; Bonillo, B.; Ren, S.; Ratvijitvech, T.; Guiglion, P.; Zwijnenburg, M. A.; Adams, D. J.; Cooper, A. I., "Tunable Organic Photocatalysts for Visible Light-Driven Hydrogen Evolution", *Journal of the American Chemical Society* **2015**, *137*, 3265-3270.
49. Stegbauer, L.; Schwinghammer, K.; Lotsch, B. V., "A hydrazone-based covalent organic framework for photocatalytic hydrogen production", *Chemical Science* **2014**, *5*, 2789-2793.
50. Vyas, V. S.; Haase, F.; Stegbauer, L.; Savasci, G.; Podjaski, F.; Ochsenfeld, C.; Lotsch, B. V., "A tunable azine covalent organic framework platform for visible light-induced hydrogen generation", *Nat Commun* **2015**, *6*,
51. Meier, H.; Stalmach, U.; Kolshorn, H., *Acta Polymerica* **1997**, *48*, 379-384.
52. Few, S.; Frost, J. M.; Nelson, J., "Models of charge pair generation in organic solar cells", *Physical Chemistry Chemical Physics* **2015**, *17*, 2311-2325.

CHAPTER 4:
Confronting theoretical predictions to experimental data

In this chapter, I will compare the (TD-)DFT predicted reduction potentials associated with charge carriers and excitons to those measured experimentally, for a variety of conjugated oligomers relevant to water splitting. I will confront the results produced by the total-energy ΔDFT approach to experimental results found in the literature, obtained *via* two different methods, ultraviolet photoemission spectroscopy (UV-PES) and cyclic voltammetry (CV), for materials in the gas or solid phase, and in solution, respectively. I will then gauge how well predictions fit to experimental data, and evaluate the quality of my results and of the approximations used. Finally, I will discuss what such a comparison can teach us about the use of conjugated polymers as photocatalysts, focussing on their large exciton binding energy, and the mechanism through which free charge carriers are generated.

The content of this chapter has been taken from part of the following work:

Guiglion, P.; Monti, A.; Zwijnenburg, M. A., "Validating a Density Functional Theory Approach for Predicting the Redox Potentials Associated with Charge Carriers and Excitons in Polymeric Photocatalysts", *J. Phys. Chem. C* **2017**, 121, 1498-1506.

4.1. Motivation and Literature review

One of the crucial requirements for a potential photocatalyst, polymeric or not, to meet is the thermodynamic ability to drive both of the water splitting, as seen in the previous chapter, or CO_2 photoreduction solution half-reactions. Knowledge of the IP, EA, IP* and EA* potentials is hence crucial when trying to understand the activity of known photocatalysts or develop new ones. Reliably measuring such potentials, especially under operating conditions, however, is far from easy. For example, cyclic voltammetry on solid polymer films, placed on an electrode in contact with an aprotic polar solvent system, is generally hard to interpret because the voltammograms tend to be broad, show signs of irreversibility[1-3] and involve the incorporation of counter ions and solvent molecules into the film,[4] which would not be expected under photocatalysis conditions. A related problem with CV is that measuring the electron affinity values of polymers is complicated by the fact that these often lie outside the stability window of common solvents, and that one thus has to be cautious not to confuse a signal due to solvent oxidation with the signature of electron affinity. The ability to calculate the redox potentials of charge carriers and excitons therefore is very useful, especially as it moreover allows one to predict those of hypothetical materials that have not been synthesised as yet, and thus to screen computationally for promising photocatalysts (see Chapter 5). The latter is an especially attractive proposition for polymeric materials, for which the synthesis, purification and characterisation of both the polymer and constituting monomers can be very time consuming.

The main difference between our group's computational approach and that developed by others[5-11] is that it revolves around molecular calculations in combination with a continuum dielectric screening model[12] to describe the material and its environment rather than calculations using periodic boundary conditions (PBC).

The focus, in the case of polymeric materials, on a single polymer strand and the assumption that all intermolecular interaction, be it with other polymer strands or

water, can be described in terms of a dielectric response, is related to the fact that such materials are often amorphous or only poorly crystallised. Therefore, we do not have good experimental structural models for polymers to use in PBC calculations, and even if we did construct periodic models artificially, they would not necessarily be representative of the solid. Another difference between our approach and that of many others is that we calculate the potentials using a total-energy ΔDFT approach, rather than equate IP and EA with generalised Kohn-Sham (GKS) orbital energies (see Chapter 2), which is problematic, at least conceptually, especially for EA.[13-14] Finally, we also take into account the (self-)trapping of charge carriers and excitons, *i.e.* the formation of polarons and polaronic excitons, into account by considering adiabatic rather than vertical potentials.

In this chapter, I compare predicted polymer and oligomer potentials to those measured from three distinctly different datasets; gas phase photoemission spectroscopy (PES) for oligomers of poly(p-phenylene),[15] solution electrochemistry data for oligomers of poly(p-phenylene)[16] and poly(fluorene)[17] derivatised with solubilising alkyl chains, and solid-state (inverse) PES data[10, 15, 18-27] for a range of conjugated polymers. The differences between this and previous work validating the use of hybrid DFT for predicting redox potentials in the literature[28-40] is a combination of (i) our focus on oligomers/polymers rather than small molecules or metal complexes, (ii) our emphasis on potentials in condensed phases, including the solid-state, (iii) the fact that we calculate adiabatic rather than vertical potentials and/or (iv) because we also consider excited state potentials.

I will show that (TD-)DFT calculations using the standard B3LYP[41-42] density functional yield reasonable gas and solution phase potentials and rather consistently good solid-state potentials, the latter in line with previous work for the IP and EA of small molecules.[32-34] I will further demonstrate that these good solid-state potentials appear to be the result of rather benign error cancellation. I will discuss that the good fit for solid-state potentials in vacuum suggests that a similar accuracy can be expected for calculations on solid-state polymers interfaced with water. I will also outline the requirements on a density functional to consistently calculate the potentials associated with charge carriers and excitons in polymeric

materials. Finally, I will examine what a comparison of experimental and computationally predicted potentials teaches us about conjugated polymers as water splitting photocatalysts.

4.2. Computational methodology

Potentials, be they computationally predicted or experimentally measured, are always expressed with respect to a reference (typically vacuum in the case of photoelectron spectroscopy) and a reference electrode, for example, the standard hydrogen electrode (SHE), for liquid electrochemistry. A key parameter in the conversion from one potential reference to another is the value of the SHE absolute potential (SHEAP), for which a range of experimental values are proposed, something that is partly related to different possible choices for thermodynamic standard states and partly due to extra-thermodynamic assumptions.[43] In this chapter, I consider two values of the SHEAP: 4.44 V, the original IUPAC-recommended value[44] as used in the previous chapter when studying PPP, and a more recently proposed value of 4.28 V.[43] Where possible, I will present results for both SHEAP choices. However, if in the text only one value is mentioned for a given system this will be based on the use of 4.44 V for SHEAP, which is the default value used throughout this thesis.

4.3. Results and discussion

4.3.1. Ionisation potentials

When an oligomer or polymer, or more generally a molecule, is taken from the gas phase into a solution, the solid state or a solid in contact with a solution, the IP of the molecule gets reduced and becomes shallower, through two different mechanisms.[45-46] Firstly, prior to ionisation, in solids, where the molecules are densely packed, hybridisation raises the energy of the highest-energy occupied orbital, from which an electron will get removed upon ionisation. Secondly, after ionisation, the dielectric nature of the environment will screen the generated charge by polarisation and stabilise energetically the charged species formed. The difference between the gas and condensed IP values is commonly referred to as the polarisation energy, even if only part of this difference is the result of dielectric polarisation and, in contrast to what the names suggest, it also contains a contribution due to hybridisation.

	gas phase		DCM[b]		solid phase	
n	*UV-PES*[a]	*B3LYP*[a]	*CV*[c]	*B3LYP*[a] *ε = 8.93*	*UV-PES*[a]	*B3LYP*[a] *ε = 2*
2	3.72 (3.88)	3.26 (3.42)	1.91	1.42 (1.58)	-	-
3	3.36 (3.52)	2.71 (2.87)	1.78	1.22 (1.38)	1.66 (1.82)	2.09 (2.25)
4	-	-	1.73	1.13 (1.29)	-	-
5	-	-	1.69	1.09 (1.25)	-	-
6	2.76 (2.92)	2.08 (2.24)	1.66	1.07 (1.23)	1.46 (1.62)	1.63 (1.79)
7	-	-	1.65	1.05 (1.21)	-	-
8	-	-	1.65	-	-	-
∞	-	-	1.5[d]	0.9[d]	1.21/1.36[e] (1.37/1.52)	1.45 (1.61)[f]

Table 4.1: Experimentally measured and computationally predicted IP values of p-phenylene oligomers and polymers in different environments vs. SHE (all values in volts).

[a]Absolute IP vs. vacuum converted to SHE scale by a shift of 4.44 and 4.28 (inside parentheses), respectively. [b]Oligomers with branched iso-alkyl chains at the terminal p-carbon atoms. [c]Measured in DCM in the presence of 0.2 M n-Bu4NPF6 supporting electrolyte against SCE, values converted to SHE scale by application of a shift of +0.244. [d]Obtained through linear extrapolation vs. 1/n. [e]Value obtained by two different extrapolation methods in the original experimental paper. [f]Modelled using an oligomer of 12 units.

Experimental CV data taken from reference [16], and UV-PES data from reference [15].

Table 4.1 shows experimental and DFT predicted values of the IP of oligomers and polymers of *p*-phenylene in the gas phase, in a dichloromethane (DCM) solution, and as a solid. I will first concentrate on the experimental values taken from the literature.[15-16] While one has to be slightly careful with comparing these experimental potentials as they are measured using two fundamentally different methods, ultraviolet PES (UV-PES) and CV, and because of the need to convert between different potential references, vacuum for UV-PES and the standard calomel electrode (SCE)/SHE and the ferrocene/ferrocenium redox couple in the case of CV, such a comparison is very insightful.

As expected based on the literature, the gas phase IP values are the deepest, with the solid state and DCM solution values being 1-2 V smaller than the corresponding gas phase values. More interestingly, the polarisation energies for the different oligomers in the solid state and DCM, which can be extracted from the IP values in Table 4.1, are very similar. As the dielectric permittivity of the solid-state oligomer/polymer phase is likely to be smaller than that of DCM, especially given the fact that the supporting electrolyte is likely to increase the effective dielectric permittivity of the DCM solution through ion-pair formation,[47] this suggests that the smaller dielectric contribution to the permittivity and thus screening of the formed charge in the solid state relative to the solution is more than compensated by the larger contribution due to hybridisation in the former. On the basis of the numbers, it is hard to extract an exact value for the effect of hybridisation, but it is likely to be at least a few tenths of volts. The experimental polarisation energy values measured for the oligomers, finally, are similar in magnitude to those measured for organic crystals[45-46] and appear to decrease with oligomer length.

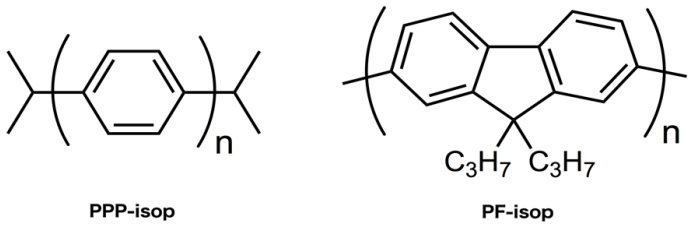

Figure 4.1: Structures of oligomer models studied computationally.

Moving on to the computational predictions, where the alkyl side chain is approximated by an isopropyl group (see Figure 4.1), inspection of Table 4.1 shows that, for the gas and solution phases, ΔDFT calculations using the B3LYP functional yield IP values that are 0.5−0.6 V shallower, *i.e.* less positive, than those measured experimentally. A similar shift was reported by Baik and Friesner when calculating EA values of small molecules in solution using B3LYP.[28] Calculations using a slightly higher dielectric permittivity for the DCM solution than that of pure DCM in order to take into account that the supporting electrolyte will likely increase the effective dielectric permittivity (see Table 4.2), as well as calculations with larger basis-sets (Table 4.3), do not sufficiently change this observation.

	p-phenylene			fluorene		
n	*CV*[c]	*B3LYP*[a] *ε = 8.93*	*B3LYP*[a] *ε = 12*	*CV*[c]	*B3LYP*[a] *ε = 8.93*	*B3LYP*[a] *ε = 12*
2	1.91	1.42 (1.58)	1.36 (1.52)	1.58	0.99 (1.15)	0.93 (1.09)
3	1.78	1.22 (1.38)	1.17 (1.33)	1.47	0.85 (1.01)	0.80 (0.96)
4	1.73	1.13 (1.29)	1.08 (1.24)	1.43	0.79 (0.95)	0.75 (0.91)
5	1.69	1.09 (1.25)	1.04 (1.20)	1.38	0.76 (0.92)	0.82 (0.98)
6	1.66	1.07 (1.23)	0.97 (1.13)	1.40	0.74 (0.90)	0.71 (0.87)
7	1.65	1.05 (1.21)	1.01 (1.17)	1.40	0.74 (0.90)	-

Table 4.2: Experimentally measured and computationally predicted IP values of p-phenylene and fluorene oligomers and polymers in a DCM solution vs. SHE (all values in volts).

[a]Absolute IP vs. vacuum converted to SHE scale by a shift of 4.44 and 4.28 (inside parentheses), respectively. [c]Measured in DCM in the presence of 0.2 M n-Bu_4NPF_6 supporting electrolyte against SCE, values converted to SHE scale by application of a shift of +0.244.

Phenylene experimental CV data taken from reference [16], and fluorene CV data from reference [17].

Moreover, a comparison between similar ΔB3LYP calculations and experimental data for the ionisation potentials of oligo(fluorene) in solution (Table 4.2) finds a similar 0.5−0.6 V shift, suggesting this to be a quite general feature. In contrast to the gas and solution phases, in calculations for the solid state, in which hybridisation is neglected, the predicted IP values are 0.2−0.4 V more shallow, less positive, than those measured experimentally.

	p-phenylene ε = 8.93				polyfluorene ε = 2	
n	*CV* [c]	*B3LYP/DZP*	*B3LYP /def2-TZVP*	*potential*	*B3LYP/DZP*	*B3LYP /def2-TZVP*
2	1.91	1.42	1.45	EA	1.41	1.48
3	1.78	1.22	1.26	IP	5.56	5.59
4	1.73	1.13	1.17			

Table 4.3: Comparison of the computationally predicted IPs of p-phenylene oligomers (vs. SHE, left side) and IP and EA values of a polyfluorene polymer (vs. Vacuum, right side) calculated using the double-zeta DZP and triple-zeta def2-TZVP basis-sets.

[c]Measured in DCM in the presence of 0.2 M n-Bu_4NPF_6 supporting electrolyte against SCE, values converted to SHE scale by application of a shift of +0.244.

Phenylene experimental CV data taken from reference [16]

For the dissolved oligomers, the calculations reproduce the experimentally obtained polarisation energy values rather well, but the solid-state polarisation energies are underestimated by ~1 V. If the isotropic dielectric screening model used in the calculation correctly reproduces the dielectric component of the polarisation energy, this would suggest that the effect of hybridisation is ~65% of the polarisation energy and far from negligible (calculated from values in Table 4.1 for the trimer and hexamer: comparison between the difference between (i) experimental data in gas phase and solid state, and (ii) B3LYP predictions in gas phase and solid state). However, the absolute values of the solid-state IPs, most relevant in this work, are, as discussed above, reasonably well reproduced. As the inherent density functional related error and the error introduced by neglecting hybridisation have similar magnitudes and opposite signs, the solid-state values lie close to their experimental counterparts by error cancelation.

This success in reproducing experimental values of solid-state IP values for polymers appears to be not limited to oligomers and the polymer of *p*-phenylene. Figure 4.2 and Table 4.4 show a comparison of IPs of a range of conjugated polymers measured experimentally by UV-PES[15, 18-21, 23, 27] and B3LYP calculations, again using ε_r = 2, for oligomers of 12 units (see Chapter 1 for the structures of different polymers studied). Concentrating on the polymers without side chains, for all materials, except perhaps polypyrrole, the match is quite good (maximum deviation of −0.44 V, for polypyrrole, and a mean absolute deviation of 0.20 V) and the DFT predictions correctly recover the relative ordering of the IPs of the different

polymers. Since polypyrrole is easily oxidisable,[21] the deviation observed for this material can in part find its origin in experiment.

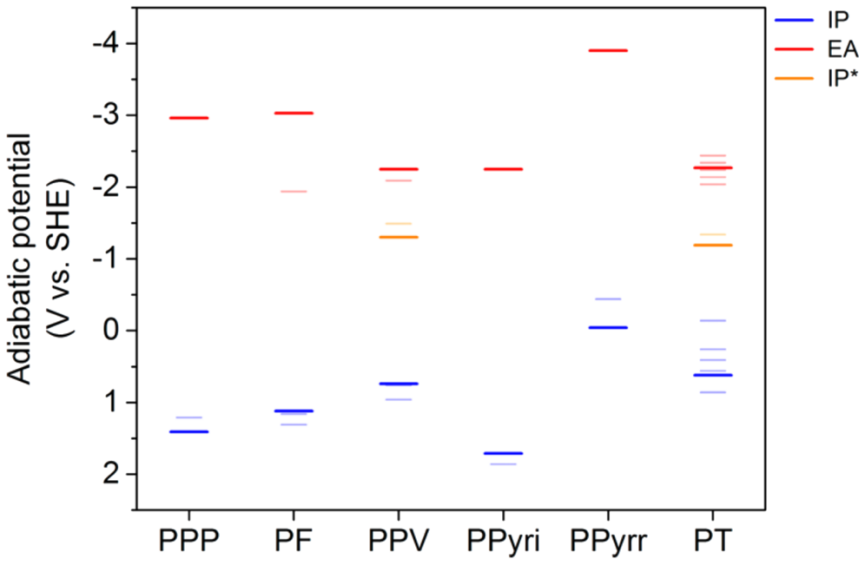

Figure 4.2: Comparison between the potentials predicted using (TD-)B3LYP and ε_r = 2 (thick lines), and measured experimentally (thin lines), for a range of conjugated polymers.

	IP		
	B3LYP [a]	*Experimental literature values*	
		non-derivatised	*derivatised*
PPP	5.85 (5.89)	5.65 / 5.85[b,15]	-
PF	5.56 (5.60)	-	5.75[24]
PPV	5.18 (5.21) - 5.49[c]	5.2[19]	5.4[25] / 5.6[23]
PPyri	6.15 (6.19)	6.3[22]	-
PPyrr	4.40 (4.44)	4.0[21]	-
PT	5.06 (5.09) - 4.91[c]	5.3[20]	4.3-5.0[d,27] / 4.85[26]

Table 4.4: Comparison between solid-state IP values for the different polymers predicted by B3YLP calculations, and experimental values from the literature. All values in Volt vs. vacuum. PPV refers to poly(p-phenylene-vinylene).

[a] values including outlying charge correction in between parentheses.
[b] value obtained by two different extrapolation methods in the original experimental paper.
[c] result for calculations including short alkyl chains.
[d] range of values reported depending on the regiochemistry and molecular weight.

Use of a slightly higher dielectric permittivity than 2 for the heteroatom containing polymers, to account for the fact that such polymers probably have a higher dielectric permittivity than pure hydrocarbon polymers (see Table 4.5), if anything worsens the fit. In this context, it is important to remember that photoemission is likely to mostly involve molecules near the polymer–vacuum interface due to the surface sensitivity of UV-PES and that such molecules as a result will be less screened than in the bulk.[48]

	IP	EA
PPyri	5.85	2.69
PPyrr	4.06	1.13
PT	4.76	2.69

Table 4.5: B3LYP solid-state IP and EA values for polypyridine, polypyrrole and polythiophene calculated using ε_r = 10 instead of 2. All values in Volt vs. vacuum.

These results also suggest that the single oligomer embedded in a dielectric continuum approximation, which ignores details of molecular packing, works very well for these amorphous/quasi-crystalline polymers, even if for fully crystalline materials there are cases known where non-isotropic packing effects are large and one has to go beyond the continuum approach.[49] Overall, these results and the fact that the (dielectric) effect of going from an interface with vacuum to water is most likely additive suggest that the computational setup used will also provide decent predictions for the IP of a polymer interfaced with water. Protonation of a polymer might induce an additional shift in the potentials, but this is, even for the nitrogen containing polymers, unlikely to be an issue at (near) neutral pH.

4.3.2. Electron affinities

In contrast to the relative multitude of reference data on the IP of oligomers and polymers, there is very little experimental data on the EA of oligomers and polymers, especially in the solid state. Most reported electron affinities are obtained by adding the optical gap, *i.e.* the onset of light absorption, to the value of the IP, but this is a questionable approach. More theoretically justified values can be obtained from

either inverse PES or the high kinetic energy edge of two-photon PES (2PPE) spectra. Such data only seem to be available, currently, for three of the polymers discussed in the previous section, which are the alkyl-chain derivatised versions: of PT, poly(3-hexylthiophene) (P3HT),[26-27] of PF, poly(9,9-dioctylfluorene)[24] (PF8), and of PPV, poly(2-methoxy-5-(2-ethyl-hexyloxy)-p-phenylene vinylene)[25] (MEH-PPV).

	EA		
	B3LYP [a]	*Experimental literature values*	
		non-derivatised	*derivatised*
PPP	1.48 (1.52)	-	-
PF	1.41 (1.45) - 1.45[b]	-	2.5[24]
PPV	2.19 (2.23)	-	2.35[25]
PPyri	2.19 (2.23)	-	-
PPyrr	0.54 (0.58)	-	-
PT	2.17 (2.20) - 1.95[b]	-	2.0-2.3[c,27] / 2.4[26]

Table 4.6: Comparison between solid-state EA values for the different polymers predicted by B3YLP calculations, and experimental values from the literature. All values in Volt vs. vacuum. PPV refers to poly(p-phenylene-vinylene).

[a] values including outlying charge correction in between parentheses.
[b] result for calculations including short alkyl chains.
[c] range of values reported depending on the regiochemistry and molecular weight.

As can be seen from Figure 4.2 in the previous section and Table 4.6 above, the fit is good for P3HT and PPV, and slightly less good for PF8. This is for calculations neglecting the alkyl side chains. However, calculations that take these side chains into account, included in Table 4.6, show that these side chains are predicted to only have a small effect on the electron affinity. While these three data points are not sufficient to properly test it in terms of its ability to correctly predict electron affinities of polymers in the solid state, they at least give some confidence in our approach. Similarly, as for the IP, the difference in the EA for a polymer in contact with vacuum and water is expected to be adequately described by changing the dielectric permittivity from 2 to that of water.

4.3.3. Excited-state potentials

Experimental benchmark data for the excited state potentials of relevant polymers are as rare as data for EA, if not rarer. There exist some 2PPE data, where the process of ionisation of the intermediate state by the second photon can be hypothesised to correspond to the ionisation of a (self-trapped) exciton and thus IP*, for only two polymers: P3HT,[26] and MEH-PPV.[25] As can be seen from Figure 4.2 in previous section 4.3.1, and in Table 4.7 below, the experimentally measured values appear in line with the values predicted by our computational approach for the polymers without side chains. Moreover, for both P3HT and MEH-PPV, EA and IP* are split by ~0.7 (e)V, *i.e.* the adiabatic exciton-binding energy, in experiment, and by ~1 (e)V in my calculations. Similarly, as for EA, while these two data points for IP* are not sufficient to properly test the computational methodology in terms of its ability to correctly predict electron affinities of polymers in the solid state, it does give confidence in our approach.

	IP*		
	B3LYP	*Experimental literature values*	
		non-derivatised	*derivatised*
PPV	3.14	-	2.95[25]
PT	3.25	-	3.1[26]

Table 4.7: Comparison between solid-state excited-state ionisation potentials for the different polymers predicted by B3YLP calculations and experimental values from the literature. All values in Volt vs. vacuum.

Experimental data that could directly validate EA* predictions, not found in the literature, would require a 2PPE equivalent inverse photoemission spectroscopy. However, as by definition, the splitting between IP and EA* is the same as between EA and IP*, the fit between predicted IP* and 2PPE values in combination with the fit between experimental and computational IP values suggests that EA* might be as well described as IP*. Again, just as for IP and EA, the effect of water is likely to be additive for IP* and EA*.

4.4. Perspectives

Consistently calculating the set of potentials associated with the charge carriers and exciton is a rather demanding application. Other density functionals than B3LYP, for example optimally tuned range-separated density functionals, [36, 39, 50] might very likely yield more accurate values for the ionisation potential or electron affinity of oligomers in the gas phase or in solution. However, to be useful in this context, use of such a functional should simultaneously allow for the calculations of the other potentials, including the excited state potentials (and hence the optical properties of a system) and the potentials of solution reactions, and all to a similar consistent standard. Additionally, while the dependence on error cancelation to predict decent solid-state values is unsatisfying from a theoretical point of view, it saves one from having to do calculations on extended models of the solid.

If our estimate of the contribution of hybridisation to the polarisation energy for PPP is correct and a general feature of conjugated polymers, then calculations with functionals that give better gas phase values might require calculations on explicit stacks to obtain solid-state values or *ad hoc* shifts. The latter is probably as conceptually unsatisfying as relying on error cancelation, while the former is, at least for polymers that are amorphous or poorly crystallised, difficult to achieve due to, as discussed in the first section of this chapter, the lack of meaningful structural models. An additional complication with calculations on explicit stacks is the fact that the percentage of Hartree–Fock exchange included the density functional fixes the intermolecular dielectric screening inside the stack.[51] As a result, the effective dielectric constant inside the stack might be different from its desired value and different from that used in the external continuum dielectric screening model.

4.5. Conclusions

For a range of polymers relevant to photocatalysis, the predictions of density functional theory for the redox potentials associated with charge carriers and excitons were compared to those measured experimentally. A good fit was found between the values predicted using ΔB3LYP and those measured experimentally, for the ionisation potentials of solid-state polymers in contact with vacuum. Among the different classes of potentials available experimentally for conjugated polymers, the ones considered were those measured under the conditions most similar to those occurring during water splitting.

Although experimental data measured under similar conditions for the electron affinity and excited state ionisation potential are much more limited, the fit to ΔB3LYP is decent in both cases. Overall, the comparison with experimental data gives good confidence in the use of ΔB3LYP to predict polymer potentials for solids and suggests that, if the effect of replacing the interface with vacuum by an interface with water is largely dielectric in nature, the here used approach should also give accurate predictions under water splitting conditions.

In contrast to the case of solid-state polymers, the ΔB3LYP predicted ionisation potentials for oligomers of *p*-phenylene in the gas phase and solutions and oligomers of fluorene are off by 0.5−0.6 V with respect to experiment. A combination of this observation and comparison of experimental and theoretical estimates of the polarisation energy suggests that the consistently good fit for solid polymers may be the result of error cancellation. Despite the lack of similar data for the electron affinity and excited state potentials, but it stands to reason that the decent description of these potentials is similarly the result of error cancelation.

4.6. References

1. Tsai, E. W.; Basak, S.; Ruiz, J. P.; Reynolds, J. R.; Rajeshwar, K., "Electrochemistry of some β-Substituted Polythiophenes: Anodic Oxidation, Electrochromism, and Electrochemical Deactivation", *Journal of The Electrochemical Society* **1989**, *136*, 3683-3689.
2. Novák, P.; Rasch, B.; Vielstich, W., "Overoxidation of Polypyrrole in Propylene Carbonate: An In Situ FTIR Study", *Journal of The Electrochemical Society* **1991**, *138*, 3300-3304.
3. Zotti, G.; Schiavon, G.; Zecchin, S., "Irreversible processes in the electrochemical reduction of polythiophenes. Chemical modifications of the polymer and charge-trapping phenomena", *Synthetic Metals* **1995**, *72*, 275-281.
4. Vyas, R. N.; Wang, B., "Electrochemical Analysis of Conducting Polymer Thin Films", *International Journal of Molecular Sciences* **2010**, *11*, 1956-1972.
5. Toroker, M. C.; Kanan, D. K.; Alidoust, N.; Isseroff, L. Y.; Liao, P.; Carter, E. A., "First principles scheme to evaluate band edge positions in potential transition metal oxide photocatalysts and photoelectrodes", *Physical Chemistry Chemical Physics* **2011**, *13*, 16644-16654.
6. Castelli, I. E.; Olsen, T.; Datta, S.; Landis, D. D.; Dahl, S.; Thygesen, K. S.; Jacobsen, K. W., "Computational screening of perovskite metal oxides for optimal solar light capture", *Energy & Environmental Science* **2012**, *5*, 5814-5819.
7. Persson, K. A.; Waldwick, B.; Lazic, P.; Ceder, G., "Prediction of solid-aqueous equilibria: Scheme to combine first-principles calculations of solids with experimental aqueous states", *Physical Review B* **2012**, *85*, 235438.
8. Zhuang, H. L.; Hennig, R. G., "Single-Layer Group-III Monochalcogenide Photocatalysts for Water Splitting", *Chemistry of Materials* **2013**, *25*, 3232-3238.
9. Stevanovic, V.; Lany, S.; Ginley, D. S.; Tumas, W.; Zunger, A., "Assessing capability of semiconductors to split water using ionization potentials and electron affinities only", *Physical Chemistry Chemical Physics* **2014**, *16*, 3706-3714.
10. Jiang, X.; Wang, P.; Zhao, J., "2D covalent triazine framework: a new class of organic photocatalyst for water splitting", *Journal of Materials Chemistry A* **2015**, *3*, 7750-7758.
11. Buckeridge, J.; Butler, K. T.; Catlow, C. R. A.; Logsdail, A. J.; Scanlon, D. O.; Shevlin, S. A.; Woodley, S. M.; Sokol, A. A.; Walsh, A., "Polymorph Engineering of TiO2: Demonstrating How Absolute Reference Potentials Are Determined by Local Coordination", *Chemistry of Materials* **2015**, *27*, 3844-3851.
12. Tomasi, J.; Mennucci, B.; Cammi, R., "Quantum Mechanical Continuum Solvation Models", *Chemical reviews* **2005**, *105*, 2999-3094.
13. Baerends, E. J.; Gritsenko, O. V.; van Meer, R., "The Kohn-Sham gap, the fundamental gap and the optical gap: the physical meaning of occupied and virtual Kohn-Sham orbital energies", *Physical Chemistry Chemical Physics* **2013**, *15*, 16408-16425.

14. Guiglion, P.; Berardo, E.; Butchosa, C.; Wobbe, M. C. C.; Zwijnenburg, M. A., "Modelling materials for solar fuel synthesis by artificial photosynthesis; predicting the optical, electronic and redox properties of photocatalysts", *Journal of Physics: Condensed Matter* **2016**, *28*, 074001.
15. Seki, K.; Karlsson, U. O.; Engelhardt, R.; Koch, E.-E.; Schmidt, W., "Intramolecular band mapping of poly(p-phenylene) via UV photoelectron spectroscopy of finite polyphenyls", *Chemical Physics* **1984**, *91*, 459-470.
16. Banerjee, M.; Shukla, R.; Rathore, R., *Journal of the American Chemical Society* **2009**, *131*, 1780-1786.
17. Chi, C.; Wegner, G., "Chain-Length Dependence of the Electrochemical Properties of Conjugated Oligofluorenes", *Macromolecular Rapid Communications* **2005**, *26*, 1532-1537.
18. Nagashima, U.; Fujimoto, H.; Inokuchi, H.; Seki, K., "Electronic and geometric structures of oligothiophenes", *Journal of Molecular Structure* **1989**, *197*, 265-289.
19. Seki, K.; Asada, S.; Mori, T.; Inokuchi, H.; Murase, I.; Ohnishi, T.; Noguchi, T., "UV photoemission spectroscopy of poly(p-phenylene vinylene) (PPV)", *Solid State Communications* **1990**, *74*, 677-680.
20. Fujimoto, H.; Nagashima, U.; Inokuchi, H.; Seki, K.; Nakahara, N.; Nakayama, J.; Hoshino, M.; Fukuda, K., "Electronic and geometric structures of oligothiophenes studied by UPS and MNDO: π-band evolution and effect of disorder", *Physica Scripta* **1990**, *41*, 105.
21. Hino, S.; Iwasaki, K.; Tatematsu, H.; Matsumoto, K., "Photoelectron Spectra of Polypyrrole: The Effect of the Ambient Atmosphere to the Spectra", *Bulletin of the Chemical Society of Japan* **1990**, *63*, 2199-2205.
22. Miyamae, T.; Yoshimura, D.; Ishii, H.; Ouchi, Y.; Seki, K.; Miyazaki, T.; Koike, T.; Yamamoto, T., "Ultraviolet photoelectron spectroscopy of poly(pyridine-2,5-diyl), poly(2,2′-bipyridine-5,5′-diyl), and their K-doped states", *The Journal of Chemical Physics* **1995**, *103*, 2738-2744.
23. Liao, L. S.; Fung, M. K.; Lee, C. S.; Lee, S. T.; Inbasekaran, M.; Woo, E. P.; Wu, W. W., "Electronic structure and energy band gap of poly (9,9-dioctylfluorene) investigated by photoelectron spectroscopy", *Applied Physics Letters* **2000**, *76*, 3582-3584.
24. Hwang, J.; Kim, E.-G.; Liu, J.; Brédas, J.-L.; Duggal, A.; Kahn, A., "Photoelectron Spectroscopic Study of the Electronic Band Structure of Polyfluorene and Fluorene-Arylamine Copolymers at Interfaces", *The Journal of Physical Chemistry C* **2007**, *111*, 1378-1384.
25. Sohn, Y.; Stuckless, J. T., "Bimolecular recombination kinetics and interfacial electronic structures of poly[2-methoxy-5-(2-ethyl-hexyloxy)-p-phenylene vinylene] on gold studied using two-photon photoemission spectroscopy", *The Journal of Chemical Physics* **2007**, *126*, 174901.
26. Sohn, Y.; Stuckless, J. T., "Characteristics of Photoexcitations and Interfacial Energy Levels of Regioregular Poly(3-hexythiophene-2,5-diyl) on Gold", *ChemPhysChem* **2007**, *8*, 1937-1942.
27. Kanai, K.; Miyazaki, T.; Suzuki, H.; Inaba, M.; Ouchi, Y.; Seki, K., "Effect of annealing on the electronic structure of poly(3-hexylthiophene) thin film", *Physical Chemistry Chemical Physics* **2010**, *12*, 273-282.

28. Baik, M.-H.; Friesner, R. A., "Computing Redox Potentials in Solution: Density Functional Theory as A Tool for Rational Design of Redox Agents", *The Journal of Physical Chemistry A* **2002**, *106*, 7407-7412.
29. Uudsemaa, M.; Tamm, T., "Density-Functional Theory Calculations of Aqueous Redox Potentials of Fourth-Period Transition Metals", *The Journal of Physical Chemistry A* **2003**, *107*, 9997-10003.
30. Shimodaira, Y.; Miura, T.; Kudo, A.; Kobayashi, H., "DFT Method Estimation of Standard Redox Potential of Metal Ions and Metal Complexes", *Journal of Chemical Theory and Computation* **2007**, *3*, 789-795.
31. Roy, L. E.; Jakubikova, E.; Guthrie, M. G.; Batista, E. R., "Calculation of One-Electron Redox Potentials Revisited. Is It Possible to Calculate Accurate Potentials with Density Functional Methods?", *The Journal of Physical Chemistry A* **2009**, *113*, 6745-6750.
32. Nayak, P. K.; Periasamy, N., "Calculation of ionization potential of amorphous organic thin-films using solvation model and DFT", *Org. Electron.* **2009**, *10*, 532-535.
33. Nayak, P. K.; Periasamy, N., "Calculation of electron affinity, ionization potential, transport gap, optical band gap and exciton binding energy of organic solids using 'solvation' model and DFT", *Org. Electron.* **2009**, *10*, 1396-1400.
34. Schwenn, P. E.; Burn, P. L.; Powell, B. J., "Calculation of solid state molecular ionisation energies and electron affinities for organic semiconductors", *Org. Electron.* **2011**, *12*, 394-403.
35. Hughes, T. F.; Friesner, R. A., "Development of Accurate DFT Methods for Computing Redox Potentials of Transition Metal Complexes: Results for Model Complexes and Application to Cytochrome P450", *Journal of Chemical Theory and Computation* **2012**, *8*, 442-459.
36. Tamblyn, I.; Refaely-Abramson, S.; Neaton, J. B.; Kronik, L., "Simultaneous Determination of Structures, Vibrations, and Frontier Orbital Energies from a Self-Consistent Range-Separated Hybrid Functional", *The Journal of Physical Chemistry Letters* **2014**, *5*, 2734-2741.
37. Phillips, H.; Zheng, Z.; Geva, E.; Dunietz, B. D., "Orbital gap predictions for rational design of organic photovoltaic materials", *Org. Electron.* **2014**, *15*, 1509-1520.
38. Richard, R. M.; Marshall, M. S.; Dolgounitcheva, O.; Ortiz, J. V.; Brédas, J.-L.; Marom, N.; Sherrill, C. D., "Accurate Ionization Potentials and Electron Affinities of Acceptor Molecules I. Reference Data at the CCSD(T) Complete Basis Set Limit", *Journal of Chemical Theory and Computation* **2016**, *12*, 595-604.
39. Gallandi, L.; Marom, N.; Rinke, P.; Körzdörfer, T., "Accurate Ionization Potentials and Electron Affinities of Acceptor Molecules II: Non-Empirically Tuned Long-Range Corrected Hybrid Functionals", *Journal of Chemical Theory and Computation* **2016**, *12*, 605-614.
40. Rangel, T.; Hamed, S. M.; Bruneval, F.; Neaton, J. B., "Evaluating the GW Approximation with CCSD(T) for Charged Excitations Across the Oligoacenes", *Journal of Chemical Theory and Computation* **2016**, *12*, 2834-2842.
41. Becke, A. D., "Density-functional thermochemistry. III. The role of exact exchange", *Journal of Chemical Physics* **1993**, *98*, 5648-5652.

42. Stephens, P. J.; Devlin, F. J.; Chabalowski, C. F.; Frisch, M. J., "Ab Initio Calculation of Vibrational Absorption and Circular Dichroism Spectra Using Density Functional Force Fields", *The Journal of Physical Chemistry* **1994**, *98*, 11623-11627.
43. Isse, A. A.; Gennaro, A., "Absolute Potential of the Standard Hydrogen Electrode and the Problem of Interconversion of Potentials in Different Solvents", *The Journal of Physical Chemistry B* **2010**, *114*, 7894-7899.
44. Trasatti, S., "The absolute electrode potential: an explanatory note (Recommendations 1986)", *Journal of Electroanalytical Chemistry and Interfacial Electrochemistry* **1986**, *209*, 417-428.
45. Sato, N.; Seki, K.; Inokuchi, H., "Polarization energies of organic solids determined by ultraviolet photoelectron spectroscopy", *Journal of the Chemical Society, Faraday Transactions 2: Molecular and Chemical Physics* **1981**, *77*, 1621-1633.
46. Inokuchi, H.; Seki, K.; Sato, N., "UV Photoelectron Spectroscopy of Organic Molecular Materials", *Physica Scripta* **1987**, *1987*, 93.
47. Gestblom, B.; Songstad, J., "Solvent Properties of Dichloromethane. VI. Dielectric Properties of Electrolytes in Dichloromethane.", *Acta Chem. Scand.* **1987**, *41*, 396–409.
48. Tsiper, E. V.; Soos, Z. G.; Gao, W.; Kahn, A., "Electronic polarization at surfaces and thin films of organic molecular crystals: PTCDA", *Chemical Physics Letters* **2002**, *360*, 47-52.
49. Ryno, S. M.; Risko, C.; Brédas, J.-L., "Impact of Molecular Packing on Electronic Polarization in Organic Crystals: The Case of Pentacene vs TIPS-Pentacene", *Journal of the American Chemical Society* **2014**, *136*, 6421-6427.
50. Stein, T.; Eisenberg, H.; Kronik, L.; Baer, R., "Fundamental Gaps in Finite Systems from Eigenvalues of a Generalized Kohn-Sham Method", *Physical Review Letters* **2010**, *105*, 266802.
51. Refaely-Abramson, S.; Sharifzadeh, S.; Jain, M.; Baer, R.; Neaton, J. B.; Kronik, L., "Gap renormalization of molecular crystals from density-functional theory", *Physical Review B* **2013**, *88*, 081204.

CHAPTER 5:
Beyond PPP; screening for suitable photocatalysts

In this chapter, I will apply the computational methodology presented in Chapter 3 and validated in Chapter 4, to systematically calculate the redox potentials associated with free charge carriers and excitons (IP, EA*, IP*, EA), for a variety of oligomeric systems. Those include oligofluorene derivatives, phenylene and pyrene-based conjugated microporous polymers (CMPs), linear oligomers of common conjugated "building blocks" (pyridine, pyrimidine, pyrazine, pyrrole, furan, and thiophene), and carbon nitride flakes or oligomers (based on triazine and heptazine motifs). I will comment on key factors that can enhance photocatalytic properties, and describe the strengths and limitations of our computational approach.

Some of the content of this chapter has been taken from the following published work:

Guiglion P.; Butchosa C.; Zwijnenburg M. A., "Polymeric watersplitting photocatalysts; a computational perspective on the water oxidation conundrum", *J. Mat. Chem. A* **2014**, *2*, 11996-12004.

Butchosa C.; Guiglion P.; Zwijnenburg M. A., "Carbon Nitride Photocatalysts for Water Splitting: A Computational Perspective", *J. Phys. Chem. C* **2014**, *118*, 24833-24842.

Sprick R.S.; Jiang J.-X.; Bonillo B.; Ren S.; Ratvijitvech T.; Guiglion P.; Zwijnenburg M. A.; Adams D. J.; Cooper A. I., "Tunable Organic Photocatalysts for Visible Light-Driven Hydrogen Evolution", *J. Am. Chem. Soc.* **2015**, *137*, 3265-3270.

Sprick R. S.; Bonillo B.; Clowes R.; Guiglion P.; Brownbill N.J.; Slater B.J.; Blanc F.; Zwijnenburg M. A.; Adams D. J.; Cooper A. I., "Visible Light-Driven Water Splitting

Using Planarized Conjugated Polymer Photocatalysts", *Angew. Chem. Int. Ed.* **2016**, *55*, 1792-1796.

Guiglion P.; Butchosa C.; Zwijnenburg M. A., "Polymer Photocatalysts for Water Splitting: Insights from Computational Modeling", *Macromol. Chem. Phys.* **2016**, *217*, 344-353.

5.1. Motivation and Literature review

The computational method introduced in Chapter 3 and validated in Chapter 4 offers a tool for screening molecules that is robust and computationally tractable. The idea of using computational screening in order to find promising candidate photocatalysts is not a new one. However, studies that compare the effectiveness of chemical systems to split water traditionally employ a rather crude approximation. Such studies generally assess the relevance of photocatalysts by predicting and comparing the positions of their Kohn-Sham HOMO and LUMO. As explained in Chapter 3, the presented methodology goes beyond those limitations by considering both the ground state and excited state of chemical systems, using a TD-DFT approach.

The screening for relevant photocatalysts will be carried out by gradually moving away from pure PPP. I will first investigate copolymers of phenylene and fluorene (and of other fluorene-type derivatives), then focus on Conjugated Microporous Polymers (CMPs) based on phenylene and pyrene, before shifting my attention to a variety of heteroatom-containing linear oligomers. Finally, I will discuss one of the most promising candidate photocatalysts for overall water splitting, Carbon Nitride (CN).

Copolymers based on fluorene and its derivatives are a class of materials that show great potential. Starting from a rather flexible PPP chain, it is possible to further planarise and rigidify the molecular backbone, by introducing a methylene linker between every other phenylene unit (effectively replacing some phenylene moieties by fluorene motifs). Indeed, extended planarisation in polymers has been shown to decrease the electron-hole binding energy, and to increase exciton dissociation yields[1-2] and charge carrier mobility.[3-4], which should result in overall better photocatalytic activity. Additionally, Sprick and co-workers [5] recently demonstrated experimentally that planarisation leads to increased hydrogen evolution rates. I will therefore discuss several planarised copolymers of phenylene and fluorene, and of fluorene-type derivatives (introduced in Chapter 1) to hopefully find the origin of

such enhanced photocatalytic performance for the reduction of protons to molecular hydrogen.

Conjugated Microporous Polymers (CMPs) have also generated a lot of interest in the last few years[6-9]. Phenylene and pyrene-based CMP materials (introduced in Chapter 1) are rather challenging to characterise experimentally, hence the need for a computational approach to help elucidate their structure-property relationships. In particular, the origin of the relatively good performance of pyrene-phenylene CMPs compared to their pure phenylene counterparts, noted by Sprick *et al.*,[10] needs to be explained.

Apart from fluorene derivatives and pyrene and phenylene-based CMPs, other types of oligomers, built from linear arrangements of common conjugated molecules (introduced, along with PPP, in Chapter 1), widely described in fields such as organic photovoltaics and organic light-emitting diodes, will be investigated. Those include linear homopolymers of pyrrole, pyridine, diazine, pyrimidine, thiophene, phenylene-vinylene, and furan, as well as their phenylene copolymers.

Linear polymer and 2D carbon nitride materials are another very promising type of materials, that have received much attention in the last few years, due to the experimental report, in 2009, by Antonietti and co-workers, of their experimental activity for the reduction of protons, in the presence of a sacrificial electron donor, and for the oxidation of water, in the presence of a sacrificial electron acceptor, under visible light.[11] More recently, other carbon nitride systems containing carbon nanodots[12] or decorated with Pt-based co-catalysts[13] were reported to split pure water in the absence of any sacrificial reagent.

In the next section, the standard reduction potentials of CN cluster models will be calculated, first, in order to evaluate the established computational methodology, and second, to hopefully determine the reason why in most cases[12-13], experimentally, carbon nitride, until recently[12-13], was only known to catalyse either the proton reduction half-reaction in the presence of a SED, or the oxidation of water into molecular oxygen in the presence of a SEA, but not both concurrently.[11]

Among those different types of materials, I will aim at finding the most promising candidates for solar-driven water splitting, *i.e.* photocatalysts that have deep (very positive) IP and EA*, and shallow (very negative) EA and IP*, always bearing in mind the additional constraint that the absorption onset of the ideal material should be small enough for it to absorb visible light, and large enough for it to drive, at least thermodynamically, ideally both the proton reduction and the water oxidation half-reactions.

5.2. Results and discussion

5.2.1. Fluorene-based oligomers and derivatives

The standard reduction potentials of four fluorene-type oligomers (Fl-Ph, Cz-Ph, DBT-Ph and DBTsulf-Ph, as introduced in Chapter 1, see p. 24) were calculated, using the same methodology as for PPP in Chapter 3, *i.e.* using (TD-)B3LYP/DZP and the COSMO solvation model, with ε_r = 80.1 to take into account the influence of an aqueous environment. The standard reduction potentials of the diethylamine/triethylamine (DEA/TEA) redox couple was also calculated. As shown in our previous work on PPP[14], using the dielectric permittivity of methanol or triethylamine (experimentally used as a mixture of sacrificial reagents by Sprick *et. al*[5]) instead of water only makes a small difference. The magnitude of the contribution of vibrational/rotational/translational free-energy to the potentials of the half-reactions associated with the reduction of the oligomers (IP, EA, IP* and EA*) is small, as found in our previous work[14-15], because of the structural similarity between products and reagents, but it is large for the oxidation half-reactions of water and triethylamine.

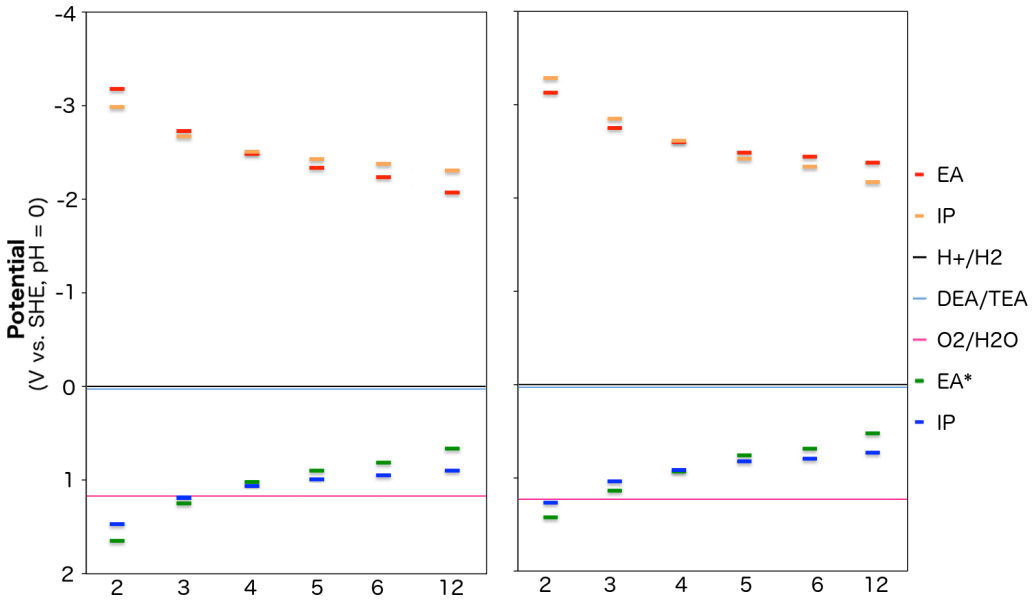

Figure 5.1: Comparison between the predicted potentials for the p-phenylene (left) and the Fl-Ph (right) oligomers, calculated at pH = 0. The numbers along the x-axis correspond to the number of equivalent phenylene moieties.

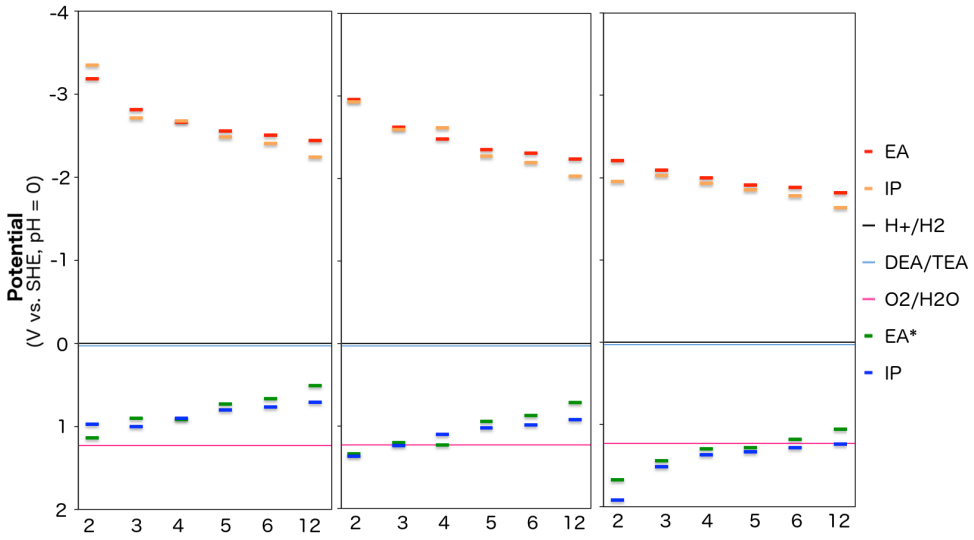

Figure 5.2: Predicted potentials for the Cz-Ph (left), the DBT-Ph (centre), and the DBTsulf-Ph (right) oligomers, calculated at pH = 0.

The absorption onsets of those oligomers were also predicted by calculating their lowest vertical singlet-singlet excitation energy (LVEE) using TD-B3LYP, either in the gas phase, or in chloroform, the solvent used experimentally when measuring the UV-Vis spectrum of the soluble oligomers, by using the COSMO model with ε_r = 4.81.

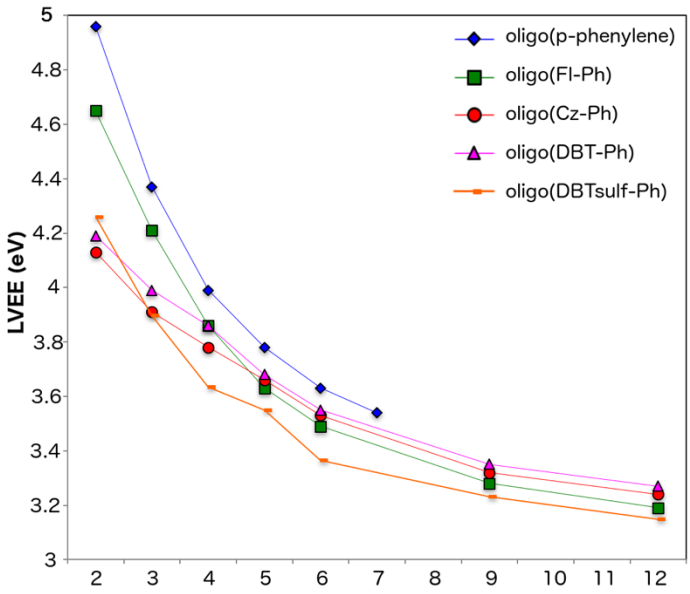

Figure 5.3: Predicted LVEE in chloroform.

For a given type of oligomer, our calculations predict a decrease in absorption onsets and a shift of EA/IP* potentials towards more positive values, when the oligomer length increases (see Figures 5.1, 5.2 and 5.3), in line with previous observations for

PPP. However, in all cases, those potentials remain considerably more negative than the potential for proton reduction to hydrogen, meaning that there will still be, in principle, ample thermodynamic driving force for hydrogen generation (Figures 5.1 and 5.2) in the long chain limit. It is therefore predicted that all fluorene-type oligomers considered should be able to run the reduction of protons to hydrogen, although it is difficult to know with certainty which material will perform best based on calculations only, due to the similarity of their EA/IP* potentials.

Sprick and co-workers, our collaborators from the University of Liverpool, carried out a series of experiments[5] where they measured the hydrogen evolution rates of small molecules including *p*-phenylene and Fl-Ph oligomers, and of polymers including PPP and Fl-Ph (and other fluorene-type, such as Cz-Ph, DBT-Ph and BDTsulf-Ph) copolymers. They also observed (unpublished work) that the photocatalytic performance of some fluorene-type homopolymers, *i.e.* without any phenylene moiety, was worse, in general, compared to their phenylene copolymer analogues. For this reason, although some pure fluorene-like homopolymers (*e.g.* polyfluorene, not shown here) are predicted to have slightly more favourable potentials for proton reduction and smaller optical gap than Fl-Ph polymers, this section will focus on copolymers instead of fluorene-like homopolymers. For all the oligomers considered, Sprick *et al.* measured a steady, almost linear increase in hydrogen evolution rates with increasing chain length (see Figure 5.4), related to a red shift of absorption onsets, enabling longer oligomers to absorb a larger part of the visible spectrum, and thus to generate more charge carriers, leading to enhanced rates of hydrogen formation.[5]

Within a range chemical compositions, for a given oligomer length, my (TD-)DFT calculations predict no significant change in absorption onset (Figures 5.1 and 5.2 for optical/fundamental gaps, and Figure 5.3 for LVEE). For short oligomer lengths, oligo(*p*-phenylene)s are expected to have consistently higher LVEE values than fluorene-*co*-phenylenes. In contrast, in the long oligomer limit, all the materials we modelled have very similar LVEE values. This is confirmed experimentally by the fact that the measured absorption onsets lie between 2.7 and 2.9 eV for all copolymers (where the conjugation limit is presumably reached), whereas for all

small oligomers, they range from 4.4 to 3.5 eV, decreasing as expected with oligomer length.

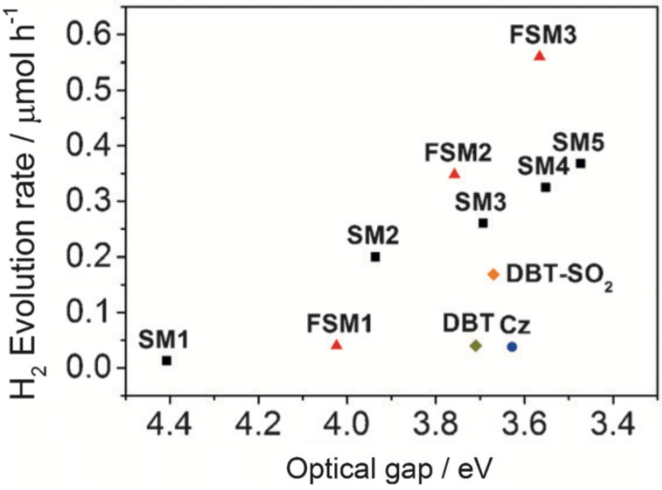

Figure 5.4: Experimentally measured[5] photocatalytic performance of oligomers against their optical gap. SM1-5 refer to PPP of oligomer lengths 3-7, FSM1-3 refer to Fl-Ph containing 2-4 phenylene equivalents, and DBT, DBT-SO_2 and Cz refer to our DBT-Ph, DBTsulf-Ph and Cz-Ph respectively.

It can be observed that, in line with the successful use of triethylamine as a sacrificial electron donor, triethylamine oxidation is overall predicted to be exothermic; the calculated IP/EA* potentials are considerably more positive than the triethylamine oxidation potential. The same also holds for methanol oxidation, not shown here, although there, the overpotential is smaller, as the methanol oxidation reaction is predicted to have a potential of +0.29 V instead of +0.03 V in the case of triethylamine (see Chapter 3).

Interestingly, it is the DBTsulf-Ph copolymer that achieves the highest hydrogen evolution rate experimentally,[5] both under UV and visible light irradiation (~145µmol/h, *i.e.* up to 15 times better than pure PPP, which evolves from ~10 to ~15 µmol/h of hydrogen depending on the type of polymerisation) followed by the DBT-Ph copolymer (~102µmol/h). By looking at the EA and IP* potentials alone, it seems that the computational approach doesn't predict those dramatic improvements in HER, which can't be rationalised by a decrease in optical gap, nor by an increased thermodynamic driving force for proton reduction. However, it is important to keep in mind that hydrogen generation is enabled by the oxidation of a

SED, here triethylamine, whose reaction rate is regulated by the positions of IP and EA* potentials. The overall water splitting reaction rate (and HER), therefore, is limited by the slowest reaction between proton reduction and triethylamine oxidation. The IP and EA* values, for the DBTsulf-Ph oligomers, are slightly deeper that for all other fluorene-type copolymers (see Figure 5.2), while their EA and IP* levels (responsible for hydrogen generation) do not vary significantly, meaning that triethylamine oxidation would be slightly favoured, which could partly explain the better performance of DBTsulf-Ph compared to the other fluorene-types, if triethylamine oxidation is indeed the rate-limiting step. This increase in HER is also likely to be ascribed to a combination of other factors, such as a change in charge carrier lifetime, charge carrier mobility, or specific surface wettability.

5.2.2. Conjugated microporous polymers

Phenylene and pyrene-phenylene CMPs

In a first step, the LVEE of the phenylene and pyrene-phenylene CMP cluster models (presented in Chapter 1) were calculated using TD-DFT with a combination of the B3LYP and CAM-B3LYP functionals (the CAM-B3LYP results are not shown here as they yield similar results and lead to the similar conclusions).

As discussed previously in the case of fluorene, for small molecules, one could assume that the LVEE coincides with the maximum of the first absorption peak. For the more complicated extended CMPs, however, the situation is more convoluted. The absorption spectrum of a CMP can be understood as the weighted average of the absorption spectra of the different local environments present, those sampled in our calculations by the different cluster models. As a result, if the more red-shifted environments form only a relatively small part of the CMP structure, the true vertical absorption onset of the CMP and other vertical excitations will lie in between the experimental absorption onset and the maximum of the first absorption peak.

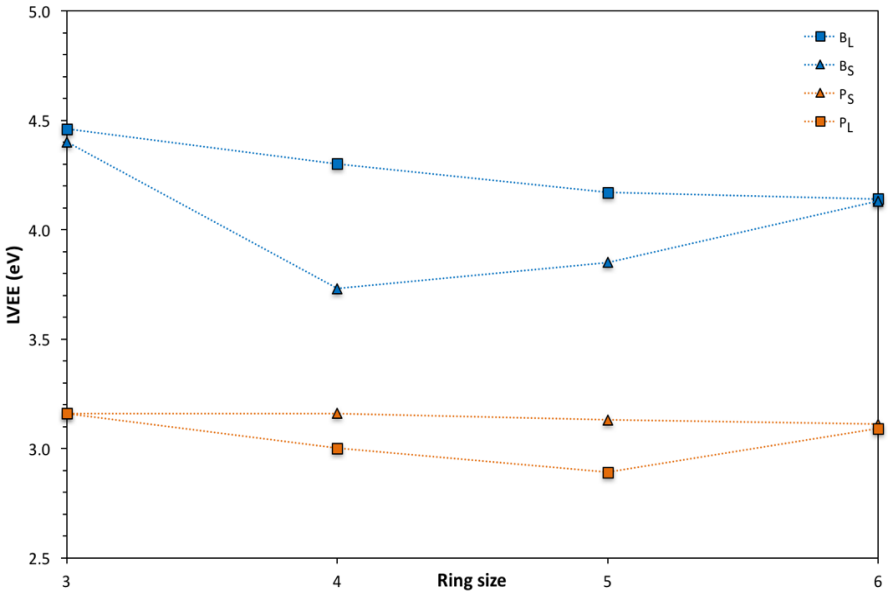

Figure 5.5: Comparison between the B3LYP predicted LVEE of phenylene (B_L and B_S) and pyrene-phenylene (P_S and P_L) cluster models of ring sizes 3 to 6 (see nomenclature p. 30, Fig. 1.15).

We observe that, independently of ring size and ring type (*i.e.* short or long vertices), phenylene rings are always predicted to have the most blue-shifted LVEE values (see Figure 5.5). The LVEE of the pyrene-phenylene rings are found to be more red-shifted relative to the pure phenylene rings (while pure pyrene rings, not shown here, are predicted to have the most red-shifted vertical absorption onset values, unsurprisingly[16]). It is likely that the above-mentioned trend in LVEE for ring cluster models is virtually independent of ring size and ring type, and that this shift is also the origin of the experimentally observed red shift in absorption onsets of the series of CMPs considered by Sprick *et al.*,[10] from pure phenylene, to pyrene-phenylene, and pure pyrene. For real materials, the ring-size distribution is likely to be different for different CMPs in the series, and some of the intermediate compositions might have phenylene-rich or phenylene-poor domains, but we believe that this will only result in second-order shifts relative to the simple effect of composition.

Computationally, the origin of the effect of composition appears to be a change in the character of the orbitals contributing to the excitations responsible for the absorption onset. The highest occupied molecular orbital (HOMO) of a pyrene ring always lies higher in energy than that of its phenylene equivalent and equally the

lowest unoccupied molecular orbital (LUMO) of a pyrene ring always lies lower in energy than that of its phenylene equivalent.

In a second step, to assess these materials' relevance for water splitting, their IP/EA* and EA/IP* potentials were calculated for the different cluster models (see nomenclature p. 29 and p. 30 Fig. 1.15).

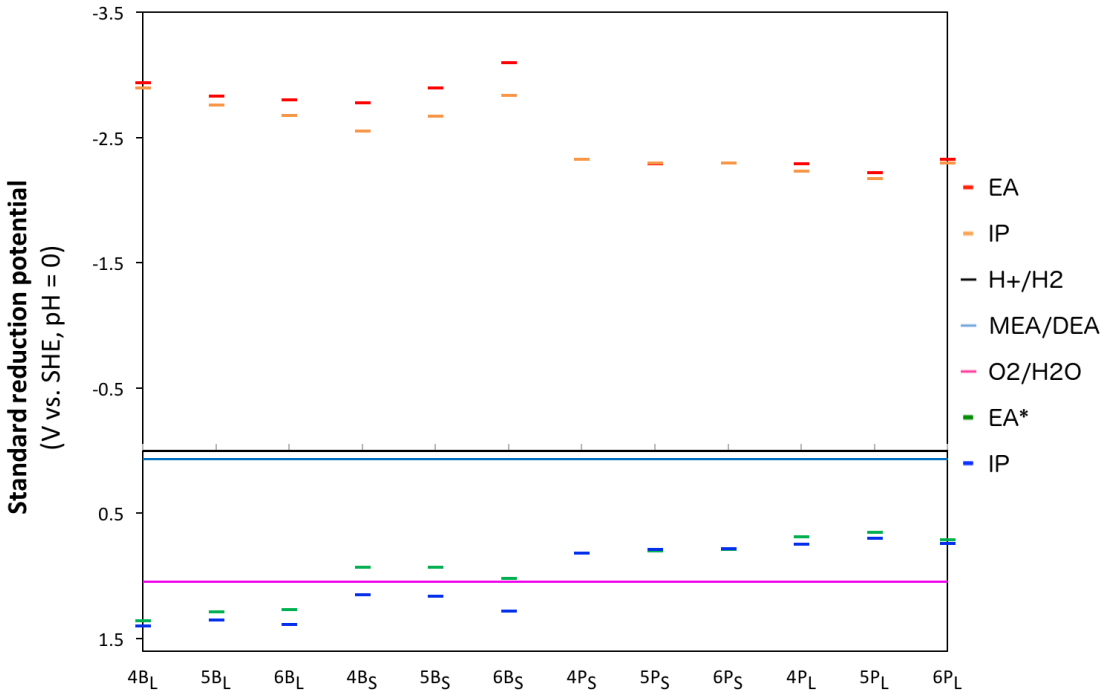

Figure 5.6: TD-B3LYP predicted IP, EA, IP* and EA values of the different ring cluster models for the phenylene and pyrene-phenylene structures, versus the standard reduction potentials of proton reduction, water oxidation and diethylamine oxidation. Potentials calculated for pH = 0, in water (using COSMO with ε_r = 80.1).*

All isomers considered show significant driving force for the reduction of protons to hydrogen, regardless of cluster size see Figure 5.6). There are, however, two key differences between phenylene and pyrene-phenylene materials. We observe that phenylene clusters (B_S and B_L) overall, have more negative EA/IP* potentials (by ~0.5 to 0.7 V), but that their optical gaps are on average 1 eV larger than their pyrene-phenylene counterparts (as can be seen on both the potential and LVEE figures above). We can therefore predict that, although phenylene clusters have a larger thermodynamic driving force for proton reduction, pyrene-phenylene clusters will absorb visible photons more readily, creating more excitons, thus generating more charge carriers, potentially resulting in improved hydrogen

evolution rates. Unfortunately, those observations are not sufficient to determine accurately which of those two competing effects will predominate. However, in contrast to the previous section, where the surprisingly good HER of DBTsulf-Ph was in part rationalised by a larger driving force for SED oxidation, we know that here it cannot be the case, since for pyrene-phenylene clusters compared to pure phenylene clusters, both the IP/EA* and the EA/IP* couples are more unfavourable (respectively for SED oxidation, and for proton reduction).

In contrast to their good predicted performance for proton reduction, all phenylene and pyrene-phenylene clusters show no or negligible driving force for water oxidation to oxygen. Therefore, sacrificial electron donors such as di- or triethylamine, whose oxidation is predicted to be very exothermic, will need to be used as electron donors.

Experimentally[10], all CMPs across a range of chemical composition, from pure phenylene to 50:50 pyrene-phenylene, show steady hydrogen production under visible-light illumination, with a gradual increase from the pure phenylene CMP (~1μmol/h), to the 50:50 pyrene-phenylene CMP, which performs best (~17μmol/h). The consistent decrease in optical gap between those two types of CMPs, which is also confirmed experimentally, seems to be the origin of the enhanced performance for the hydrogen evolution. Measurements subsequently performed on CMPs with even increased pyrene content (obtained by gradually replacing phenylene linkers by pyrene linkers, effectively increasing pyrene content gradually from 50% to 100%) showed dramatically worse hydrogen evolution rates, corresponding to much smaller optical gaps (decreasing from 2.33 to 1.94 eV, *i.e.* absorbing UV instead of visible light). All hydrogen evolution rates were measured in the presence of diethylamine as a sacrificial electron donor, since experimentally the water oxidation half-reaction cannot be driven by these CMPs.

It appears, despite the fact that the position of EA/IP* potentials is what dictates if a material can theoretically drive the reduction of protons to hydrogen, that the width of the optical gap plays a crucial role in their overall experimental hydrogen evolution performance. Among two CMPs that have well-positioned EA levels, the

best candidate will therefore be the one which has an optical gap between 2.3 and 2.5 eV, *i.e.* small enough to absorb many visible photons, but a fundamental gap large enough to straddle the potentials of the two water splitting half-reactions and drive those reactions.

Covalent triazine frameworks

The standard reduction potentials of some CTF fragment clusters were also calculated. The CTF materials of interest (presented in Chapter 1) are similar to CMPs, to the extent that they include *p*-phenylene "linker" building blocks in their molecular backbone, and can form ring structures (such as CTF-1, see Figure 5.7, and other related ring clusters)[17-18], but also very unique since they have a high nitrogen content, are typically 2-dimensional (although in practice, stacking usually makes them 3-dimensional), and possess an inherently different connectivity (trivalent triazine *vs.* tetravalent phenylene vertices).

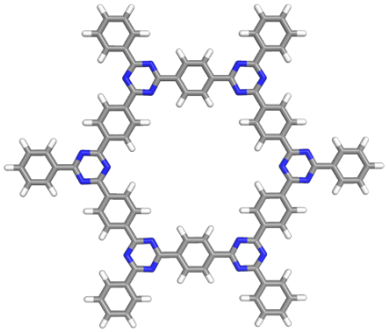

Figure 5.7: B3LYP optimised ground state structure of CTF-1, modelled as a single ring cluster.

Figure 5.8 below shows a comparison between the predicted potentials of those CTF clusters, and that of CTF-1 (see nomenclature p. 31 Fig 1.16). First, we observe that all CTF fragments have much deeper IP/EA* values than the phenylene/pyrene CMPs, and that these are ideally positioned (more positive than the water oxidation potential), meaning that they should theoretically be able to drive oxygen evolution. Their EA/IP* values, although deeper than those of the CMPs due to their overall smaller optical and fundamental gaps, are still predicted to be sufficiently negative to drive hydrogen evolution. Second, we notice that the potentials of cyano-

terminated CTF clusters are shifted to more positive values, which can be rationalised by the very electron-withdrawing nature of the cyano group.

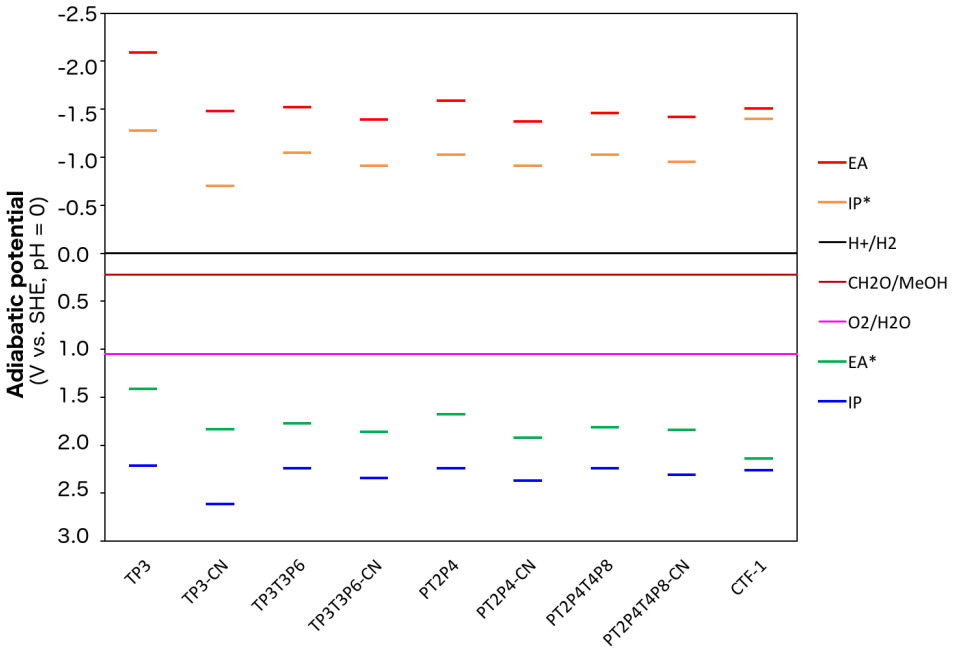

Figure 5.8: TD-B3LYP predicted IP, EA, IP* and EA values of selected CTF fragments (see nomenclature p. 31 Fig 1.16). The "–CN" suffixes indicate a cyano termination on each of the terminating phenylene para position. Potentials calculated in water.*

Third, we note that the exciton binding energy (EBE) of CTF-1, *i.e.* the difference between its fundamental and optical gaps, is predicted to be much smaller than that of the other CTF clusters. More precisely, while their fundamental gaps stay similar, the optical gap of CTF-1 is larger than those of the other CTFs. In other words, while the ring and non-ring clusters have a similar ability to drive water splitting half-reactions through charge carriers, calculations predict that in the non-ring clusters, excitons themselves can drive those reactions directly, and do not need to dissociate (which is very unlikely to happen spontaneously, given the magnitude of the predicted EBE values). However, for this last point, as the EBE values of most materials are typically in the order of tens of meV, the calculated EBE values (up to ~1.5 eV, *i.e.* larger by two orders of magnitude) and the associated interpretations should be taken with caution. Those high EBE values are likely to be artefacts due to the highly symmetrical structure of the CTF clusters, which introduces an additional excited state minimum where the excited state is delocalised over the whole structure, not encountered for real, less symmetrical structures.[19]

5.2.3. Linear conjugated oligomers

Although for PPP, in line with our predictions[14], and similarly for fluorene-phenylene oligomers[5] and (pyrene-)phenylene CMPs,[10] water oxidation has never been observed, other photocatalysts do oxidise water experimentally when using a sacrificial electron acceptor (or a sacrificial hole donor) other than water. Most of these photocatalysts are not simple hydrocarbons, but contain heteroatoms. Aside from carbon nitride (one of the most promising candidates, which will be discussed in the next section) I will now discuss simple linear, heteroatom-substituted variations of PPP. Specifically, as presented in Chapter 1, I will focus on oligomers based on pyridine, pyrimidine, pyrazine, pyrrole, thiophene and furan, some of the most popular aromatic building blocks used in the fields of organic photovoltaics and organic light emitting diodes.[20-21]

In our original PPP study[14], calculations on a heptamer of poly(pyridine-2,5-diyl)[22-23] (PPyri), the pyridine equivalent of PPP-7, suggested that the presence of nitrogen in the backbone of the polymer leads to a positive shift of the IP and EA* potentials, and thus to a larger thermodynamic driving force for water oxidation (see Figure 5.9).

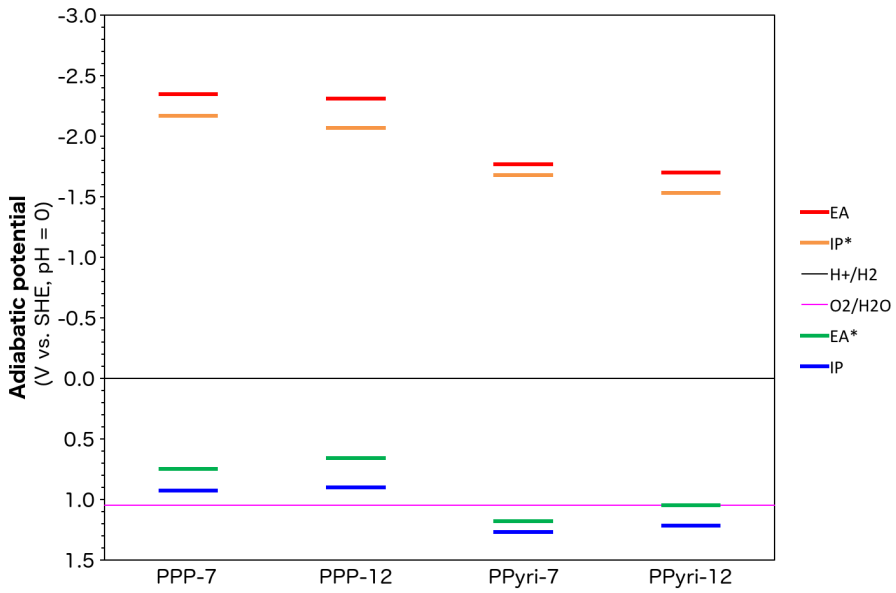

Figure 5.9: Comparison between (TD-)B3LYP predicted adiabatic potentials of PPP and PPyri, for oligomer lengths of 7 and 12, at pH = 0.

PPyri has only been observed to catalyse the proton reduction reaction experimentally[22-23] in the presence of triethylamine as sacrificial electron donor (although those studies, dating back to the years 1990s, didn't aim at achieving overall water splitting). Our calculations, however, predicted a significant overpotential (0.6 V at pH 7), implying that the lack of water oxidation activity could also be resolved for PPyri through the addition of a suitable co-catalyst. We thus observed that nitrogen substitution is a promising method of shifting the water oxidation potential in the desired direction. Moreover, in the last section, we also observed that CTFs, which were reported to oxidise water in the presence of a SEA[24], had relevant IP/EA* potentials for water oxidation.

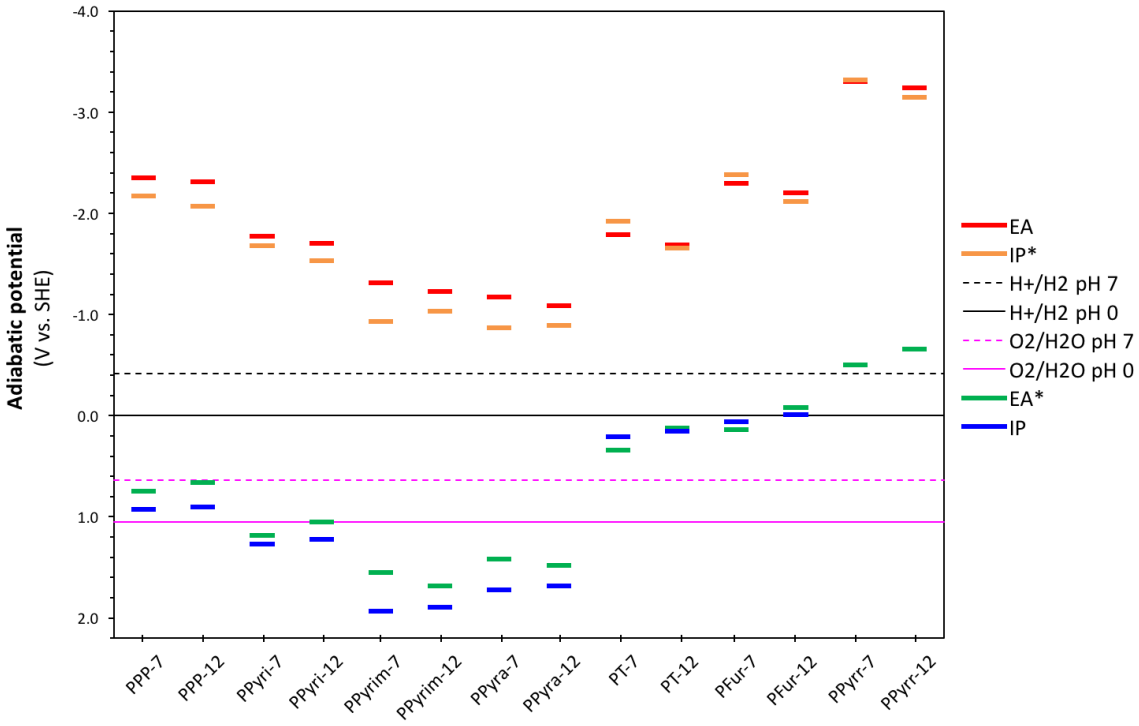

Figure 5.10: Comparison between the predicted adiabatic potentials of a range of conjugated molecules, for oligomer lengths of 7 and 12, at pH = 0 and pH = 7. See nomenclature p. 23 Fig. 1.5.

Now considering the whole range of heteroatom-containing linear oligomers (see Figure 5.10), we see that in all cases, increasing the oligomer length, as observed previously, red-shifts the optical (and fundamental) gaps. The most promising candidates for proton reduction (that have the largest driving force, *i.e.* the most negative EA/IP* potentials) are the pyrrole oligomers (PPyrr). The phenylene (PPP) and furan (PFur) oligomers, followed by the pyridine (PPyri) and thiophene (PT)

oligomers, also have suitable EA/IP* levels, whereas the pyrimidine (PPyrim) and pyrazine (PPyra) oligomers seem unpromising. All of these molecules can theoretically drive the proton reduction half-reaction. The most promising candidates for water oxidation (that have the largest driving force, *i.e.* the most positive IP/EA* potentials), on the contrary, are the pyrimidine and pyrazine oligomers, and the pyridine oligomers only show a very small overpotential for water oxidation. The remaining ones, namely PPP, PT, PFur and PPyrr, can be eliminated because of very shallow IP/EA* potentials, regardless of the pH considered.

The pyrrole and furan oligomers have more negative IP/EA and EA*/IP* potentials than the other oligomers considered. This can be explained by the fact that, although both the pyrrole and furan molecules are aromatic, they contain heteroatoms (an oxygen and a nitrogen atom, respectively) that each have two lone-pair π-electrons that participate in the molecule's aromaticity, effectively making the aromatic rings electron-rich, which shifts reduction potentials to more shallow (negative) values. Conversely, the pyridine oligomers contain nitrogen atoms that have two lone-pair π-electrons that do not contribute to the molecule's aromaticity, as they reside in a sp^2 hybrid orbital (as opposed to a 2p atomic orbital in the case of pyrrole and furan, see Figure 5.11), thus making the aromatic rings electron-deficient, which shifts reduction potentials to more positive values (see Figure 5.12 that shows electron-rich and electron-poor aromatic rings in the resonance structures of pyridine and pyrrole)

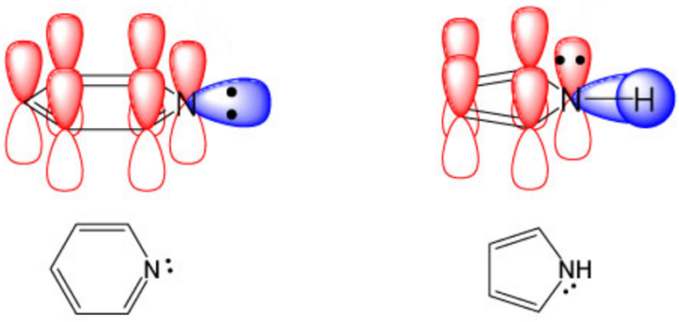

Figure 5.11: Diagram[25] showing the difference in electronic configuration of the lone pairs of pyridine (left side) and pyrrole (right side).

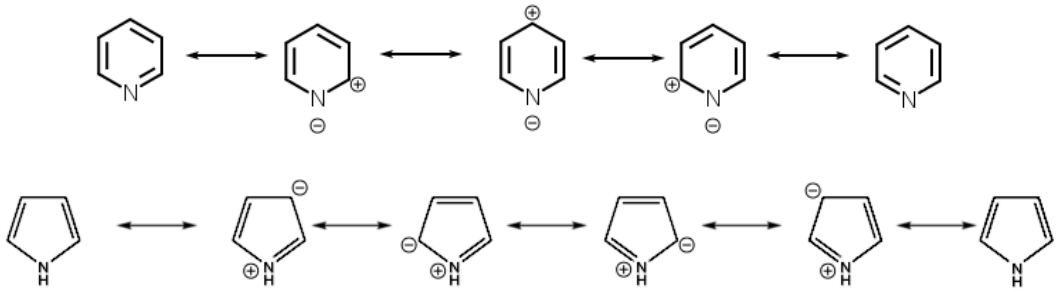

Figure 5.12: Resonance structures or pyridine (top) and pyrrole (bottom), showing electron-depleted and electron-rich aromatic rings, respectively.

For the same reasons, as they contain two nitrogen atoms per aromatic ring that make them even more electron-deficient, the pyrimidine and pyrazine oligomers have even deeper IP/EA* potentials than pyridine oligomers. The potentials of thiophene oligomers are in the same range as those of the pyrrole oligomers, because thiophene and furan have the similar electronic configuration, but the more electronegative sulphur atom of thiophene makes his aromatic ring more electron-depleted than furan, therefore shifting potentials to slightly more negative values.

Aside from these homopolymers, their PPP copolymer homologues are also investigated. For example, the pyridine-co-phenylene oligomers (PPyri-Ph) are formed by a succession of alternating pyridine and phenylene units. Our interest in phenylene copolymers rather than pyridine/pyrimidine homopolymers, for example, finds its origin in experimental observations. This class of (homo)polymers, as well as CMPs, can be synthesised mainly through Yamamoto or Suzuki couplings; the former is nickel-catalysed and involves a reaction between two bromides, while the latter is palladium-catalysed and involves a condensation between a bromide and a boronic acid. Firstly, polymers obtained *via* Yamamoto coupling experimentally give worse hydrogen evolution rates and different optical spectra (compared to those obtained *via* Suzuki coupling), and hence are likely to be have different microstructures and molecular weights. The possibility that such differences arise from the presence of residual traces of nickel or palladium in the final product was ruled out by subsequent carbon monoxide poisoning experiments[10]. Secondly, the preferred method of synthesis, Suzuki coupling, requires the presence of a boronic acid. However, boronic acids of the small

nitrogen-containing aromatic monomers prove to be challenging to synthesise, which makes their homopolymerisation *via* Suzuki coupling unpractical.

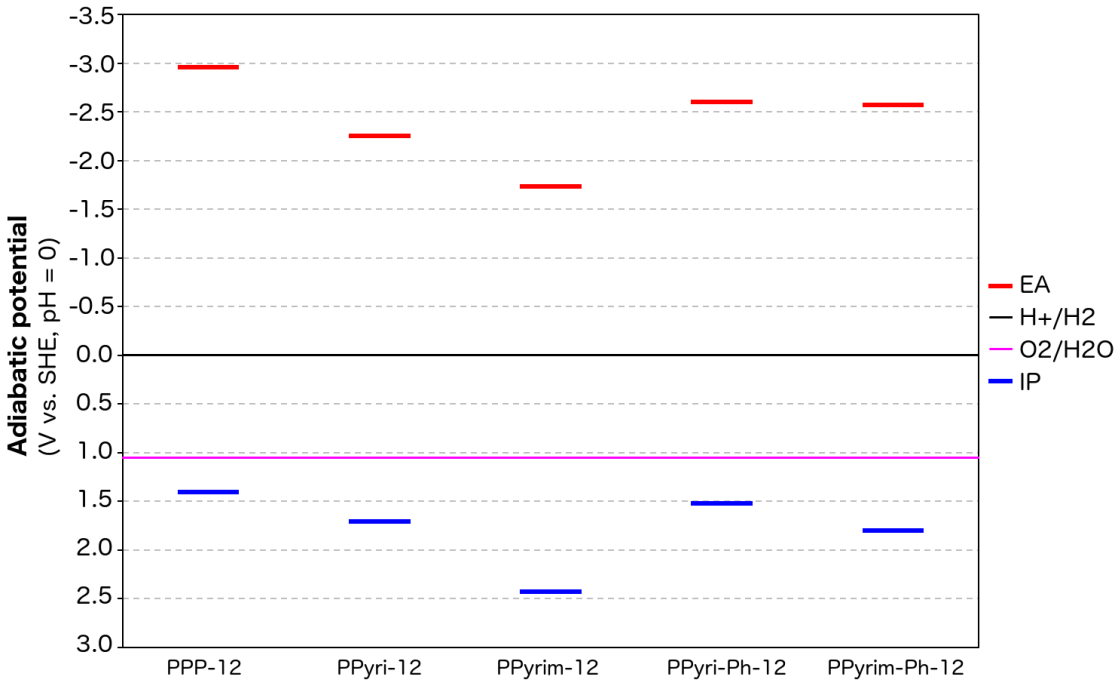

Figure 5.13: Comparison between the predicted adiabatic potentials of the PPyri (pyridine) and PPyrim (pyrimidine) oligomers, and their phenylene co-oligomer analogues PPyri-Ph and PPyrim-Ph, all having a chain length of 12 equivalent phenylene units.

Unsurprisingly, the potentials of the phenylene co-oligomers (Figure 5.13), which contain an equal number of phenylenes and other aromatic motifs (*e.g.* PPyri-Ph-12 contains 6 phenylene and 6 pyridine aromatic rings) lie halfway between the potentials of their two homo-oligomer counterparts. For example, PPyri-Ph-12 has an IP of 1.52 eV vs. SHE, while the pyridine and phenylene homo-dodecamers have IP values of 1.41 and 1.71 eV, respectively.

5.2.4. Carbon nitride

In previous work within our group, by Butchosa *et al.*,[15], the IP/EA* and EA/IP* potentials of carbon nitride cluster models were calculated. Although the calculations on heptazine and triazine oligomers were originally performed by C. Butchosa, I repeated the calculations on the heptazine models introduced in Chapter 1, starting from their ground state B3LYP optimised molecular structures, and extended those calculations by taking into consideration different solvents (*e.g.* acetonitrile) in order to compare calculated values to experimental data.

Let's first consider heptazine-based linear chains and graphitic clusters (see nomenclature pp. 26-27).

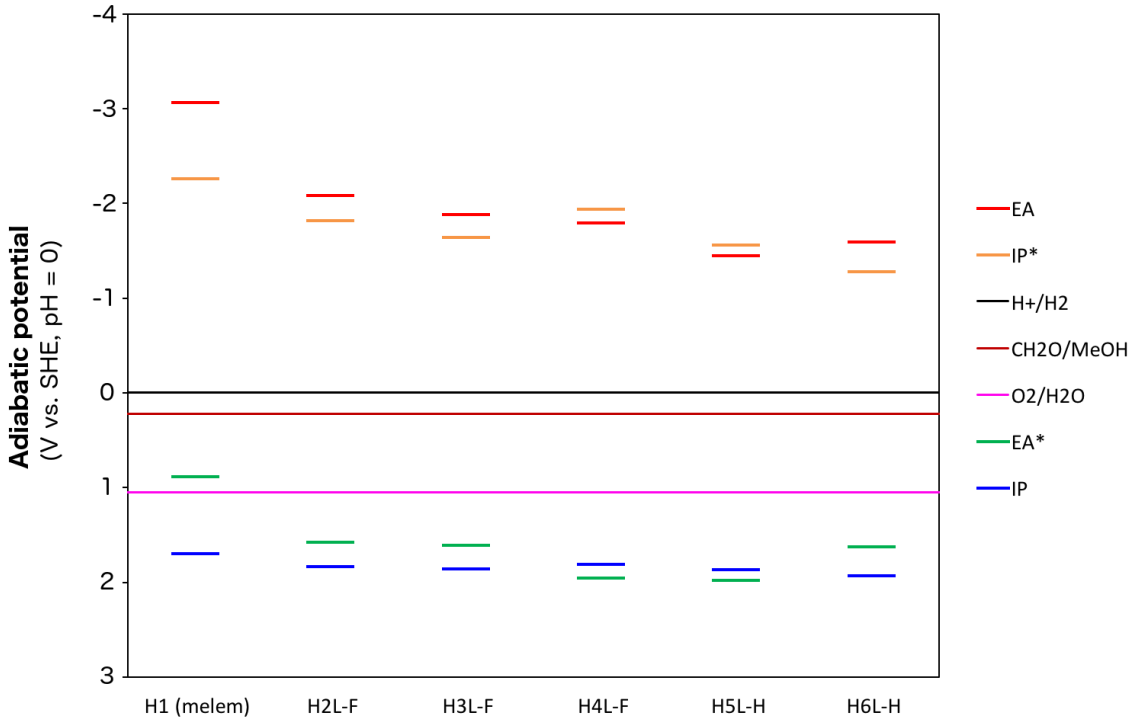

Figure 5.14: Comparison between the predicted adiabatic potentials of melem (heptazine monomer), and heptazine-based linear chains of length 2 to 6, taking into account two possible conformers (F stands for flat and H stands for helical). See nomenclature p. 26.

As we discussed in the original paper,[15] all linear cluster models are predicted to have significant thermodynamic driving force for both the reduction of protons and the oxidation of water (see Figure 5.14). Smaller clusters have higher absorption

onsets than longer chains (increasing cluster size shifts absorption onsets to the red). Therefore, if one makes the reasonable approximation that the exciton binding energy (*i.e.* the difference between the fundamental and the optical gap) doesn't vary much, smaller cluster models are predicted to have a larger thermodynamic driving force for proton reduction (the EA and IP* of the former being more negative than those of the latter), since IP and EA* do not vary significantly. However, smaller clusters might not absorb light in the desired range (visible) because of the high absorption onset.

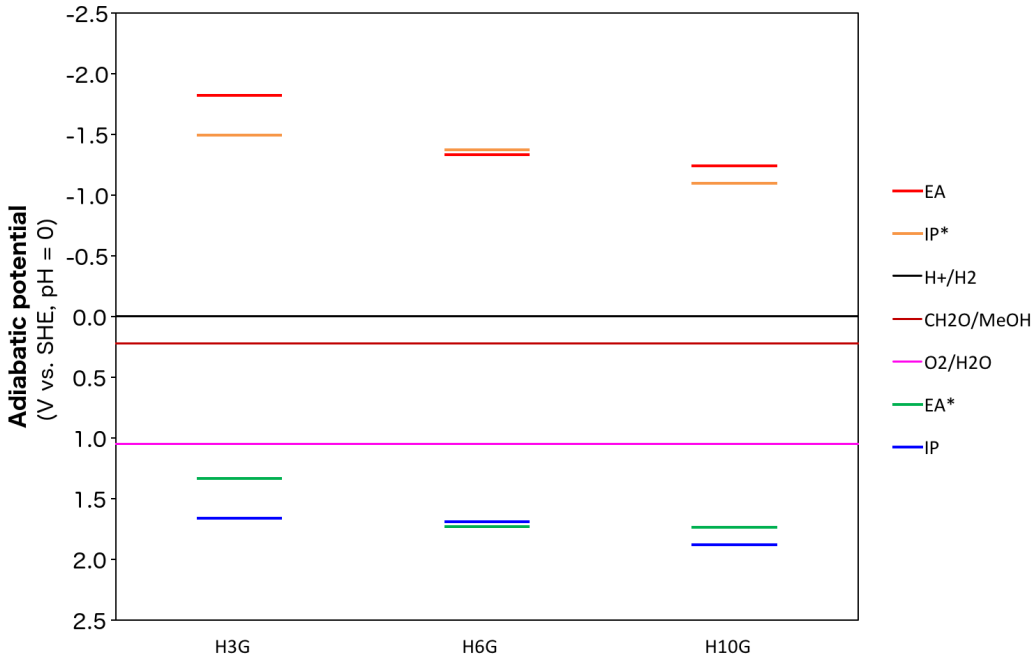

Figure 5.15: Comparison between the predicted potentials of graphitic heptazine-based clusters of sizes 3, 6 and 10. See nomenclature p. 27.

All graphitic clusters are predicted to have significant thermodynamic driving force for both the reduction of protons and the oxidation of water (see Figure 5.15). Increasing the size of the cluster shifts absorption onsets slightly to the red, and brings both IP/EA* and EA/IP* to more positive values, which only slightly decreases the driving force for proton reduction, but is beneficial for water oxidation.

Additional calculations on graphitic triazine-based clusters of sizes 3, 6, 10 and 15 by Butchosa *et al.*[15] (not shown here) lead to similar conclusions; all clusters are

predicted to have sufficient driving force for the reduction of protons. Smaller clusters have larger driving force than the larger ones; clusters of sizes 3 and 6 are predicted to have a very low driving force for water oxidation, while clusters of size 10 and 15, however, are predicted to perform better for water oxidation that their smaller counterparts, but are slightly worse for proton reduction. In line with graphitic heptazine-based clusters, increasing the cluster size shifts all absorption onsets to the red, which is desired in order to use those materials as photocatalysts under visible light irradiation.

A comparison of three different isomers of heptazine trimers was subsequently performed. Three heptazine units are (A) linked to form a linear chain, (B) joined through a central 3-coordinated nitrogen atom, and (C) each linked to the two others *via* -NH- bridges to form a graphite-like shape, relatively flat but slightly buckled (see Figure 5.16). The potentials (not shown here) of all three isomers are in the same range, theoretically making them all suitable for both proton reduction and water oxidation. We also observed slightly shallower IP/EA* and deeper EA/IP* for the graphitic cluster (C), *i.e.* slightly worse predicted performance for both reactions, but slightly better visible light absorption due to its lower absorption onset, in line with previous observations.[15]

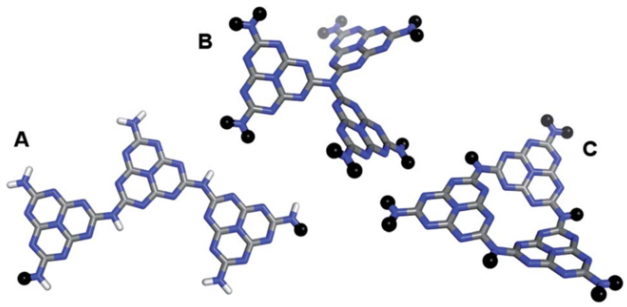

Figure 5.16: DFT-optimised ground state structures of three different isomers of a heptazine trimer.[14] The black spheres show the positions where the isomers would extend, in the case of larger, more realistic clusters.

Generally, the predicted potentials for all the carbon nitride cluster models considered are significantly different from those for PPP. Now, there is not only a clear driving force for proton reduction, but also for water oxidation. These results

strongly suggest that with a suitable co-catalyst such materials should be able to photocatalyse both reactions and split pure water into hydrogen and oxygen.

The reason why, until year 2015[12-13], no carbon nitride photocatalyst had been observed experimentally to split pure water into hydrogen and oxygen is most likely related to the fact that water oxidation to oxygen is a 4-electron reaction; therefore it is likely to be outcompeted by electron–hole recombination that prevents the build-up of sufficient amount of holes for the oxidation, in the absence of some mechanism of keeping electron and holes apart. In contrast, the oxidation of sacrificial electron donors, typically methanol (as shown on Figures 5.14 and 5.15) or triethylamine, is much more favourable both thermodynamically, because the associated potentials are shifted by approximately 1 V, making them more exothermic than water oxidation, and kinetically, since it involves only two electrons (for both methanol and triethylamine) instead of four for water.

Before the discovery of two new CN-based overall water splitting photocatalysts by Liu *et al.* and Zhang *et al.*, the only experiment in the literature where carbon nitride split pure water, by Sui *et al.*[26], used a polypyrrole co-catalyst and formed hydrogen peroxide rather than oxygen. Below, I discuss the reason for such observations. The oxidation of water to hydrogen peroxide, while thermodynamically much less favourable than the oxidation of water to oxygen (it involves a larger potential of 1.64 V, with an overpotential of 0.4–0.6 V), only requires 2 instead of 4 electrons. Liu and co-workers then showed that incorporating carbon nanodots within the carbon nitride matrix could subsequently catalyse the decomposition of photogenerated hydrogen peroxide into molecular oxygen,[12] effectively making CDot-CN an overall, metal-free water splitting photocatalyst, although still *via* a two-electron pathway.

Calculating IP and EA potentials for a graphitic heptazine-based cluster model and a pyrrole is useful to understand the observations of Sui *et al.* (see Figure 5.17). We have seen that most graphitic heptazine-based materials don't catalyse the oxidation of water, for kinetic reasons. The reduction of protons by PPyrr is predicted to be strongly exothermic, due to its very negative EA potential. However, polypyrrole shouldn't be able, on its own, to drive any oxidation (water to oxygen or

to hydrogen peroxide), on purely thermodynamic grounds, due to its extremely shallow IP.

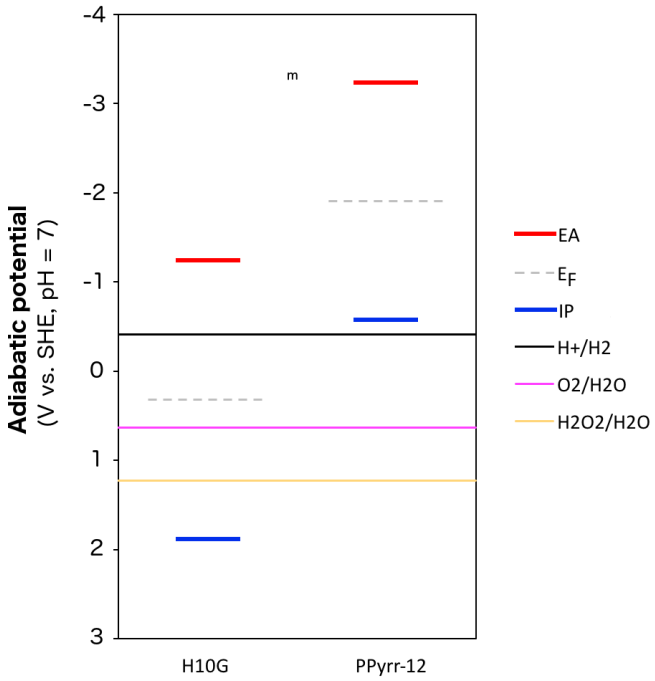

Figure 5.17: Comparison of the predicted IP and EA potentials of a graphitic carbon nitride cluster (H10G) and a polypyrrole oligomer (PPyrr-12) in water (ε_r = 80.1) at pH 7. E_F denotes the Fermi levels of corresponding materials.

However, taking the semiconductor nature of both materials into account, when carbon nitride and polypyrrole come into contact, a heterojunction is formed, and the Fermi levels of the two previously isolated semiconductors, which are likely to be very different, should equilibrate. This results in a shift between the vacuum levels on both side of the junction, which generates a difference of electrical potential, and hence an electric field. Although the exact character of the junction formed is unknown, we believe, based on the alignment of the potentials in Figure 5.17, that this built-in potential will create, after equilibration of the Fermi levels, a net negative charge on the carbon nitride, and a net positive charge on the polypyrrole. This prevents photo-generated electrons from trickling down from the conduction band of polypyrrole to the conduction band of carbon nitride, and photo-generated holes from rising up to the valence band of polypyrrole. Not only does it keep electrons and holes where they are thermodynamically able to drive water

oxidation to hydrogen peroxide and proton reduction to hydrogen, *i.e.* in the polypyrrole conduction band, and in the carbon nitride valence band, respectively, but it also increases the lifetime of charge carriers, by preventing electron-hole recombination to some extent. A similar mechanism probably explains why the CDot-CN material reported by Liu and co-workers exhibits those high oxygen evolution rates.[12]

Moving away from fully polymeric photocatalytic systems, Zhang *et al.*'s latest breakthrough[13] uses similar a mechanism to split water directly, for the first time, *via* a four-electron pathway, using selectively photodeposited Pt, PtO_x and CoO_x species as redox co-catalysts (*e.g.* Pt for hydrogen evolution and $Co(OH)_2$ for oxygen evolution). Those catalysts greatly improve reduction and oxidation rates at the active sites, leaving few electrons and holes available for recombination. While this chemical system is not metal-free, it does overcome the kinetic barriers to the oxidation of water, and doesn't need any sacrificial reagent, which shows that indeed, carbon nitride can inherently drive water oxidation, as predicted by our computational method.

5.3. Conclusions

Applying the computational methodology described in Chapter 3 to a range of conjugated molecular cluster models reveals some of the strengths and limitations of this approach.

Firstly, the study of fluorene-type oligomeric materials shows that the computational approach is successful in predicting which materials will be able to catalyse the reduction of protons to molecular hydrogen. However, there are some factors, related to experimental conditions during synthesis or photocatalysis, such as kinetic aspects, or the material's microstructure, that can't be easily predicted. Therefore, although qualitative predictions seem robust, the main goal of those calculations is not to yield an accurate and quantitative comparison of the performance of several materials. The value of this methodology, rather than finding the perfect candidate for water splitting, lies in its ability to easily and consistently rule out certain materials that would be poor choices, and hence not be worth studying for that particular application.

Secondly, comparing phenylene to pyrene-phenylene CMPs shows that absorption onsets related to the width of the optical/fundamental gap) play a crucial role in a material's photocatalytic performance; two materials that are predicted to have a similar ability to drive the proton reduction half-reaction, due to very similar EA and IP* values, might in fact differ radically because one can absorb a larger part of the visible spectrum than the other. It hence appears crucial to take into consideration both potentials and absorption onsets when screening for suitable photocatalysts.

Thirdly, applying the computational methodology to linear oligomers confirms that, by introducing heteroatoms in a linear conjugated chain, it is possible to tune the position of their standard reduction potentials, effectively making them potentially suitable, in theory, for overall water splitting. Their IP and EA potentials can either be shifted to more negative values, when making the aromatic ring units electron-rich (hence favouring thermodynamically the reduction of protons, or of sacrificial

hole donors), or to more positive values, when rendering the aromatic ring units more electron-deficient (hence favouring the oxidation of water, or of sacrificial electron donors). This prediction that heteroatom doping controls IP/EA levels is observed experimentally for polymeric materials in vacuum (see Figure 4.2 in the previous chapter).

Is is also possible to tune the optical gaps of these linear oligomers or polymers, by controlling their chain length; for the materials studied, increasing the chain length leads to smaller absorption onsets, and conversely, very short oligomers often absorb light in the UV range.

Finally, for carbon nitride, in contrast to PPP, we predict that overall water splitting is feasible in theory, which was recently confirmed[12-13], although experimentally, it has been notoriously challenging to drive both water splitting half-reactions concurrently. Typically, one would focus on hydrogen generation by using a sacrificial electron donor that was oxidised instead of water, or alternatively would favour oxygen generation by using a sacrificial electron scavenger that was reduced instead of protons. Any previous issue with water oxidation, as demonstrated by our approach, appears kinetic in nature, since the IP/EA* and EA/IP* are ideally positioned for overall water splitting. Indeed for these materials, the development of suitable co-catalysts that minimises electron–hole recombination by keeping them apart and maximises water oxidation kinetics (*e.g.* through the targeted deposition of selective co-catalysts on the photocatalyst's active sites)[13] has the potential to transform them into true water splitting photocatalysts.

5.4. References

1. Schwarz, C.; Bässler, H.; Bauer, I.; Koenen, J.-M.; Preis, E.; Scherf, U.; Köhler, A., "Does Conjugation Help Exciton Dissociation? A Study on Poly(p-phenylene)s in Planar Heterojunctions with C60 or TNF", *Advanced Materials* **2012**, *24*, 922-925.
2. Schwarz, C.; Tscheuschner, S.; Frisch, J.; Winkler, S.; Koch, N.; Bässler, H.; Köhler, A., "Role of the effective mass and interfacial dipoles on exciton dissociation in organic donor-acceptor solar cells", *Physical Review B* **2013**, *87*, 155205.
3. Zhang, W.; Smith, J.; Hamilton, R.; Heeney, M.; Kirkpatrick, J.; Song, K.; Watkins, S. E.; Anthopoulos, T.; McCulloch, I., "Systematic Improvement in Charge Carrier Mobility of Air Stable Triarylamine Copolymers", *Journal of the American Chemical Society* **2009**, *131*, 10814-10815.
4. Sprick, R. S.; Hoyos, M.; Wrackmeyer, M. S.; Sheridan Parry, A. V.; Grace, I. M.; Lambert, C.; Navarro, O.; Turner, M. L., "Extended conjugation in poly(triarylamine)s: synthesis, structure and impact on field-effect mobility", *Journal of Materials Chemistry C* **2014**, *2*, 6520-6528.
5. Sprick, R. S.; Bonillo, B.; Clowes, R.; Guiglion, P.; Brownbill, N. J.; Slater, B. J.; Blanc, F.; Zwijnenburg, M. A.; Adams, D. J.; Cooper, A. I., "Visible Light-Driven Water Splitting Using Planarized Conjugated Polymer Photocatalysts", *Angewandte Chemie International Edition* **2016**, *55*, 1792-1796.
6. Jiang, J.-X.; Trewin, A.; Adams, D. J.; Cooper, A. I., "Band gap engineering in fluorescent conjugated microporous polymers", *Chemical Science* **2011**, *2*, 1777-1781.
7. Brandt, J.; Schmidt, J.; Thomas, A.; Epping, J. D.; Weber, J., "Tunable absorption and emission wavelength in conjugated microporous polymers by copolymerization", *Polymer Chemistry* **2011**, *2*, 1950-1952.
8. Xu, Y.; Nagai, A.; Jiang, D., "Core-shell conjugated microporous polymers: a new strategy for exploring color-tunable and -controllable light emissions", *Chemical Communications* **2013**, *49*, 1591-1593.
9. Liu, X.; Xu, Y.; Guo, Z.; Nagai, A.; Jiang, D., "Super absorbent conjugated microporous polymers: a synergistic structural effect on the exceptional uptake of amines", *Chemical Communications* **2013**, *49*, 3233-3235.
10. Sprick, R. S.; Jiang, J.-X.; Bonillo, B.; Ren, S.; Ratvijitvech, T.; Guiglion, P.; Zwijnenburg, M. A.; Adams, D. J.; Cooper, A. I., "Tunable Organic Photocatalysts for Visible Light-Driven Hydrogen Evolution", *Journal of the American Chemical Society* **2015**, *137*, 3265-3270.
11. Wang, X. C.; Maeda, K.; Thomas, A.; Takanabe, K.; Xin, G.; Carlsson, J. M.; Domen, K.; Antonietti, M., "A metal-free polymeric photocatalyst for hydrogen production from water under visible light", *Nature Materials* **2009**, *8*, 76-80.
12. Liu, J.; Liu, Y.; Liu, N.; Han, Y.; Zhang, X.; Huang, H.; Lifshitz, Y.; Lee, S.-T.; Zhong, J.; Kang, Z., "Metal-free efficient photocatalyst for stable visible water splitting via a two-electron pathway", *Science* **2015**, *347*, 970.

13. Zhang, G.; Lan, Z.-A.; Lin, L.; Lin, S.; Wang, X., "Overall water splitting by Pt/g-C3N4 photocatalysts without using sacrificial agents", *Chemical Science* **2016**, *7*, 3062-3066.
14. Guiglion, P.; Butchosa, C.; Zwijnenburg, M., "Polymeric watersplitting photocatalysts; a computational perspective on the water oxidation conundrum", *Journal of Materials Chemistry A* **2014**, *2*, 11996-12004.
15. Butchosa, C.; Guiglion, P.; Zwijnenburg, M. A., "Carbon Nitride Photocatalysts for Water Splitting: A Computational Perspective", *The Journal of Physical Chemistry C* **2014**, *118*, 24833-24842.
16. Zwijnenburg, M. A.; Cheng, G.; McDonald, T. O.; Jelfs, K. E.; Jiang, J. X.; Ren, S. J.; Hasell, T.; Blanc, F.; Cooper, A. I.; Adams, D. J., "Shedding Light on Structure-Property Relationships for Conjugated Microporous Polymers: The Importance of Rings and Strain", *Macromolecules* **2013**, *46*, 7696-7704.
17. Butchosa, C.; McDonald, T. O.; Cooper, A. I.; Adams, D. J.; Zwijnenburg, M. A., "Shining a Light on s-Triazine-Based Polymers", *The Journal of Physical Chemistry C* **2014**, *118*, 4314-4324.
18. Jiang, X.; Wang, P.; Zhao, J., "2D covalent triazine framework: a new class of organic photocatalyst for water splitting", *Journal of Materials Chemistry A* **2015**, *3*, 7750-7758.
19. Meier, C. B.; Sprick, R. S.; Monti, A.; Guiglion, P.; Zwijnenburg, M. A.; Cooper, A. I., "Structure-property relationships for covalent triazine-based frameworks: the effect of spacer length on photocatalytic hydrogen evolution from water", *submitted to Polymer* **2017**,
20. Chizu, S.; Yoshiaki, T.; Takeshi, Y.; Makoto, K.; Shuji, D., "Recent progress of high performance polymer OLED and OPV materials for organic printed electronics", *Science and Technology of Advanced Materials* **2014**, *15*, 034203.
21. Li, G.; Zhu, R.; Yang, Y., "Polymer solar cells", *Nat Photon* **2012**, *6*, 153-161.
22. Matsuoka, S.; Kohzuki, T.; Kuwana, Y.; Nakamura, A.; Yanagida, S., "Visible-light-induced photocatalysis of poly(pyridine-2,5-diyl). Photoreduction of water, carbonyl compounds and alkenes with triethylamine", *Journal of the Chemical Society, Perkin Transactions 2* **1992**, 679-685.
23. Maruyama, T.; Yamamoto, T., "Effective Photocatalytic System Based on Chelating π-Conjugated Poly(2,2'-bipyridine-5,5'-diyl) and Platinum for Photoevolution of H2 from Aqueous Media and Spectroscopic Analysis of the Catalyst", *The Journal of Physical Chemistry B* **1997**, *101*, 3806-3810.
24. Bi, J.; Fang, W.; Li, L.; Wang, J.; Liang, S.; He, Y.; Liu, M.; Wu, L., "Covalent Triazine-Based Frameworks as Visible Light Photocatalysts for the Splitting of Water", *Macromolecular Rapid Communications* **2015**, DOI: 10.1002/marc.201500270.
25. Teach the Mechanism. teachthemechanism.com.
26. Sui, Y.; Liu, J.; Zhang, Y.; Tian, X.; Chen, W., "Dispersed conductive polymer nanoparticles on graphitic carbon nitride for enhanced solar-driven hydrogen evolution from pure water", *Nanoscale* **2013**, *5*, 9150-9155.

CHAPTER 6:
Contrasting the optical properties of the different isomers of PPP

In this chapter, I will study and compare the trends in optical properties of the three isomers of oligophenylene (*ortho*-phenylene, *meta*-phenylene and *para*-phenylene) using a combination of TD-DFT, with three different exchange-correlation potentials (B3LYP, BHLYP and CAM-B3LYP), and approximate Coupled Cluster Theory (RI-CC2). By carefully investigating their structure, topology, and excited-state electronic properties (absorption and fluorescence energies), I will highlight a striking difference in behaviour between those three isomers, and propose an explanation for the origin of this observed phenomenon.

The content of this chapter has been taken from the following published work:

Guiglion P.; Zwijnenburg M. A.; "Contrasting the optical properties of the different isomers of oligophenylene"; *Phys. Chem. Chem. Phys.* **2015**, *17*, 17854-17863.

6.1. Motivation and Literature review

Polyphenylene is perhaps one of the simplest conjugated polymers imaginable; consisting of a chain of aromatic phenylene units linked together by single carbon-carbon bonds. This simplicity is, however, deceptive as polyphenylene can occur in three different structural isomers; poly(*ortho*-phenylene) (*o*-phenylene), poly(*meta*-phenylene) (*m*-phenylene) and poly(*para*-phenylene) (*p*-phenylene) (see Figure 1).

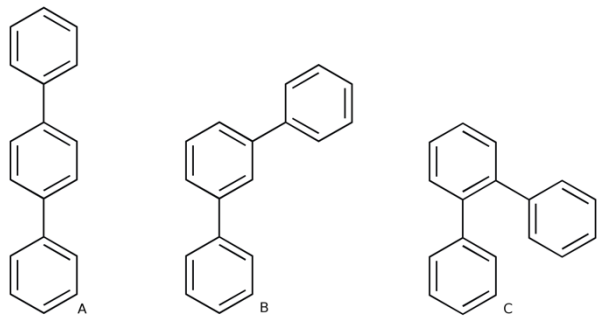

Figure 6.1: Structures of the p-terphenyl (A), m-terphenyl (B) and o-terphenyl (C) oligomers.

The difference between these three isomers is the position of the carbon atom through which the phenylene units are linked; this structural change gives rise to significantly different optical properties. For example, experimentally, the fluorescence spectrum of oligomers of *p*-phenylene is known to red shift with increasing chain length[1-5] while for oligomers of *o*-phenylene, surprisingly, it shifts to the blue.[6-9] In contrast, *m*-phenylene is effectively non-conjugated[10] and its optical properties are virtually independent of chain length.

The differences in the optical properties of these three phenylene isomers are not merely of academic interest. Polyphenylene, as outlined in Chapter 1, finds application in light emitting diodes[11] and as a photocatalyst[12-16] for the reduction of protons to molecular hydrogen (see Chapter 3) and carbon dioxide to formic acid, both in the presence of a suitable electron donor. Most of these applications involve *p*-phenylene and it stands to reason that the other isomers would give rise to a different performance in such applications. Indeed a study that explicitly compared

the ability of *o*-terphenyl, *m*-terphenyl and *p*-terphenyl oligomers to act as photocatalyst for the reduction of carbon dioxide found that *p*-terphenyl was significantly more active than the other two isomers, and interestingly also more active than the *p*-phenylene polymer.[14]

Elucidating the origin of the starkly different optical properties of the isomers of such a conceptually simple polymer is clearly both an academically and practically relevant question. Not surprisingly, there is thus a large number of computational studies on the optical[3, 5-6, 8] and related structural[9-10] properties of oligomers of phenylene. Such studies generally focus on only one of the three isomers and attempt to correlate its structural and optical properties. In this chapter, I go a step further, and study oligomers of all three isomers of phenylene on an equal footing in order to uncover the overarching structural and electronic features that explain the deviation between the optical properties of the different isomers. In order to minimise the chance of computational artefacts complicating the comparison between the different isomers, I not only use TD-DFT to calculate the optical properties of the oligomers but also, where possible, approximate couple cluster theory (see Chapter 2 for theoretical details). Finally, I carefully consider the treatment of intramolecular dispersive interactions, which will prove to be especially crucial in the case of *o*-phenylene.

6.2. Computational methodology

The computational investigation of the optical properties of oligophenylenes was carried-out using a six-step approach. First, for every system, a conformational search was performed in order to find the lowest-energy conformers. Second, the singlet ground state (S0) of selected conformers was optimised using DFT[17-18]. Third, for selected structures (trimer and hexamer), harmonic frequency calculations were performed to verify that the stationary points obtained in the S0 optimisation indeed correspond to ground-state minima. Fourth, the vertical excitation energies of the oligomers were calculated using both TD-DFT[19] and the approximate coupled-clusters singles-and-doubles method[20] (CC2). Fifth, for each oligomer, the geometry of the first excited state (S1) was relaxed using TD-DFT to obtain the S1 minimum energy structure and predict its photoluminescence (PL) energy. Finally, for selected oligomers (trimer and hexamer), numerical TD-DFT frequency calculations were performed on the S1 relaxed geometries to verify that they indeed correspond to minima.

For the conformational sampling (see Chapter 2), the OPLS-2005 forcefield[21] and the low-mode sampling algorithm[22] were employed, as implemented in Macromodel 9.9.[23] I used a combination of 10000 Monte Carlo search steps and minimum and maximum low-mode move distances of 3 and 20 Å respectively. All the structures located within an energy window of 200 kJ/mol relative to the lowest energy conformer were saved.

The DFT and TD-DFT calculations employed three different hybrid Exchange-Correlation (XC) potentials; B3LYP[24-27], BHLYP[26] and CAM-B3LYP[28]. As mentioned in Chapter 2, the B3LYP and BHLYP XC potentials include 20% and 50% Hartree-Fock-like exchange (HFLE) respectively, whereas the percentage of HFLE in CAM-B3LYP, a range separated XC-potential, changes from 19 to 65 with increasing interelectronic separation. As a result, the asymptotic behaviour of the CAM-B3LYP XC-potential (the derivative of the XC-potential with respect to the interelectronic separation r) will be closer to the formal 1/r dependence of the exact XC-potential.

Furthermore, in all TD-DFT calculations, the Tamm−Dancoff approximation to TD-DFT[29] was used, which fixes among other things problems with triplet instabilities present in full TD-DFT.[29-30] Finally, in the case of B3LYP, Grimme's D3 empirical dispersion correction was also employed.[31-33]

In the B3LYP and BHLYP calculations, the double-ζ DZP[34] basis set was used, while the CAM-B3LYP calculations typically employed the 6-31G** split-valence basis set[35]. A limited number of calculations with other basis-sets such as the larger triple-ζ def2-TZVP[36] were performed for selected systems in order to check the effect of the basis set size on the results.

The CC2 calculations were carried-out using the frozen core approximation and the resolution-of-the-identity (RI-CC2) approximation to the electron repulsion integrals. The majority of RI-CC2 calculations, for reasons of computational tractability, further employed the small def2-SV(P)[34] split-valence basis. However for single points on the smallest oligomers, calculations with the larger triple-ζ def2-TZVPP[36] basis set were also performed.

Finally, all B3LYP, BHLYP and RI-CC2 calculations were performed with the Turbomole 6.5 code[37-38]. The CAM-B3LYP calculations used NWChem 6.0[39] except in the case of the TD-DFT S1 relaxations, which were performed using GAMESS-US[40] (version 1 October 2010 R1).

6.3. Results and discussion

6.3.1. Structural models

I will start with a brief discussion of the classes of conformers considered for each isomer and their characteristic structural features before moving on to an in-depth analysis of the predicted absorption (optical gap) and fluorescence (fluorescence energy) spectra. Oligomers of *o*-, *m*- and *p*-phenylene were built. Oligomer lengths ranging from 3 (trimer) to 8 (octamer) phenylene repeat units were considered. The dimer is not considered since it is the same for *o*-, *m*- and *p*-phenylene; because of the high symmetry of benzene, the labels *o*-, *m*- and *p*- only become meaningful for oligomers of 3 units of phenylene or more.

For each isomer, conformer searches were performed to find a number of low energy conformers, with a specific focus on classes of *ordered* conformers, that were selected and subsequently re-optimised *via* DFT(+D), *i.e.* taking dispersion into account. The latter selection includes for every oligomer-size the lowest energy structure found by OPLS_2005, any ordered structures (see Figure 6.2), any structures previously reported in the literature, and a number of less-ordered structures. The ground state energy differences and variations in optical gap values between the different conformers are typically very small (less than 0.1 eV, not shown here).

The class of *p*-phenylene conformer of interest here are the lowest-energy structures for each oligomer length. It consists of a linear backbone, and has alternating torsion angles of approximately +37° and -37° (see Figure 6.2 A). Another slightly higher-energy class of *p*-phenylene conformer also has a linear backbone, but with +37° torsion angles between each phenylene unit, making it essentially helical. The latter structural difference, however, is of limited significance in the context of this study, since the optical properties of both conformers are generally very similar. The class of *o*-phenylene conformer of interest are again the lowest-energy structures for each oligomer length (when

taking into account the dispersion correction). This class of conformer has a helical backbone, where phenylenes stack every three units (see Figure 6.2 B).

For *m*-phenylene, finally, three low-energy conformers are considered: the "flat" lowest-energy conformer (see Figure 6.2 C), and two conformers with helical backbones ("large helix" and "small helix", see Figure 6.2 D and E). All those three *m*-phenylene conformers yield almost identical optical properties (again, differing by less than 0.1 eV, calculations not shown here), and are treated collectively in the remainder of this chapter.

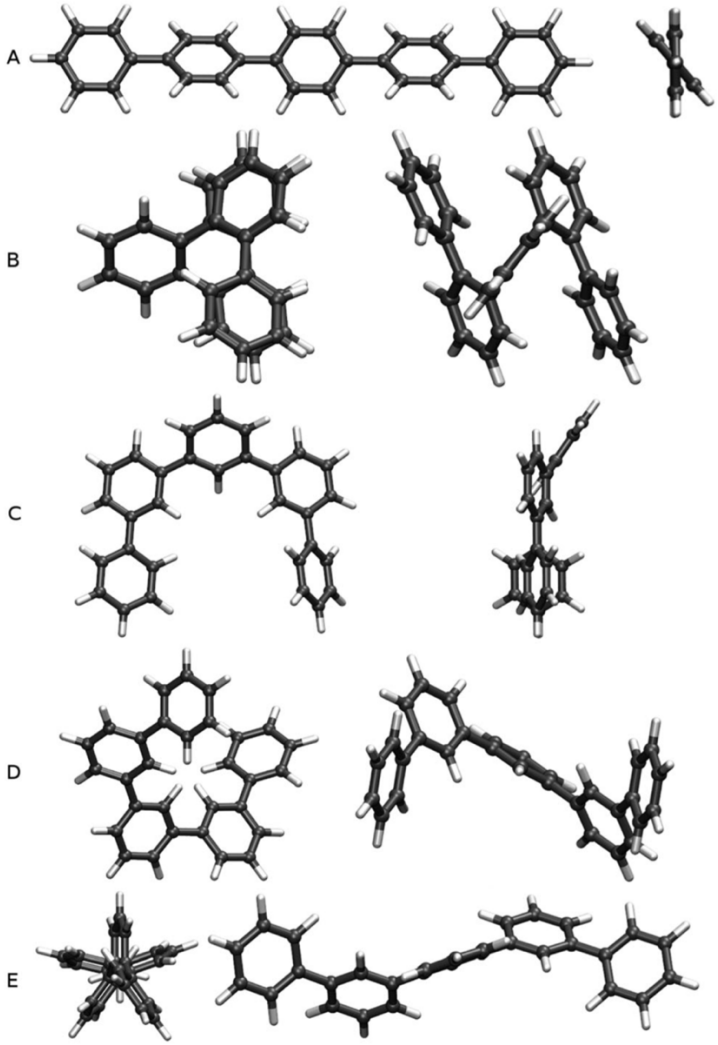

Figure 6.2: Top and side views of B3LYP optimised ground state geometries of the lowest energy conformers of p-quinquephenyl (A) and o-quinquephenyl (B), as well as three low energy conformers of m-quinquephenyl (flat structure: C; large helix: D; small helix: E).

6.3.2. Predicting the effect of isomer type and oligomer length on optical gaps

The variation of the optical gap (assimilated to the lowest vertical excitation energy, as explained in previous chapters) with the oligomer length for the different phenylene isomers is shown in Figure 6.3.

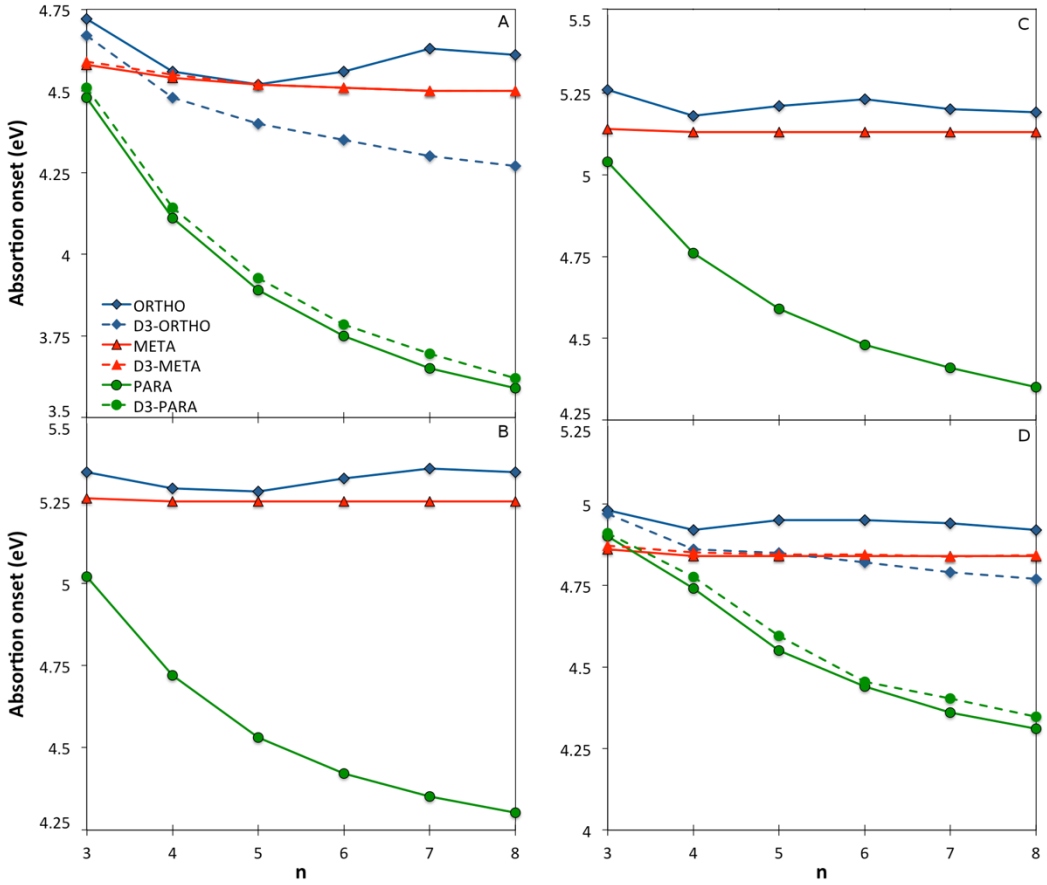

Figure 6.3: Optical gap values as a function of oligomer length for the different phenylene isomers calculated with TD-B3LYP (A), BHLYP (B), CAM-B3LYP (C) and RI-CC2 (D).

As can be seen, TD-DFT using all the three density potentials considered (B3-LYP, BH-LYP and CAM-B3LYP), as well as RI-CC2, generally yield the same qualitative trends. Moreover, quantitatively, the predictions of RI-CC2 lie in between those obtained using TD-B3YLP and TD-CAM-B3LYP. The effect of increasing the basis-set quality in the DFT calculations to def2-TZVP finally is very small (see Table 6.1). For *p*-phenylene, a pronounced red shift in the optical gap with increasing oligomer length is observed, as previously reported in the literature[1, 3-5] (see also Table 6.1).

	TD-B3LYP			Experiment
n	*gas phase*	*DCM*	*DCM* [a]	*DCM*
3	4.48 (4.44)	4.37	4.24	4.28
4	4.11 (4.09)	3.99	3.92	4.07
5	3.89 (3.87)	3.78	3.73	3.95
6	3.75	3.63	-	3.85
7	3.65	3.54	-	3.80

Table 6.1: Comparison between TD-B3LYP predicted optical gaps (in eV) of p-phenylene oligomers, in the gas phase and dichloromethane (DCM, ε_r = 8.93) and experimental data.[4] Values in brackets are obtained with the larger def2-TZVP basis-set.

[a] Substituted at both chain ends with isopropyl groups in para position.
Experimental data taken from reference [4]

Ortho-phenylenes show similar behaviour, again in line with literature[6, 8-9]. However in this case, use of Grimme's dispersion correction[31-33] to DFT (DFT-D3) is needed to accurately describe Van der Waals interactions (arene-arene π-stacking) between the phenylene units, due to their spatial proximity. Calculations on *o*-phenylene without the use of DFT-D3 in contrast predict that the optical gap first decreases then increases and ultimately decreases again with increasing oligomer length. Finally, for *m*-phenylene, increasing the oligomer length does not result in any significant change in the calculated optical gaps beyond the trimer, again in agreement with literature[10] where they are described as "conjugation breakers".

Finally, the effective conjugation length of *o*-, *m*-, and *p*-phenylene was calculated in the case of TD-B3LYP using the methodology of Meier and co-workers[41], as described in Chapter 3. Among the three isomers, *p*-phenylene is predicted to have the longest effective conjugation length (~20 repeat units, $\lambda_\infty \approx 370$ nm, $E_\infty \approx 3.35$ eV), followed by o-phenylene (~10 units, $\lambda_\infty \approx 293$ nm, $E_\infty \approx 4.23$ eV), and ultimately m-phenylene (~6 units, $\lambda_\infty \approx 276$ nm, $E_\infty \approx 4.49$ eV). The here predicted *p*- and *o*-phenylene conjugation lengths are larger than the values obtained from experimental spectra (9 and ~4 respectively) but the calculations and experiment agree on the relative conjugation lengths of the different isomers.[7, 41] The consistent difference in the absolute magnitude of conjugation lengths between the calculations and experiment is probably due to a combination of three factors.

Firstly, our calculations ignore thermal effects that might reduce the effective conjugation length, secondly, experimentally the spectra of many longer oligomers do not show well-defined peaks, and thirdly, the general insolubility of the same oligomers in most solvents means that experimental spectroscopy is inherently limited to short oligomers.

6.3.3. Linking structure, topology, and optical gap

Naïve considerations based on Hückel or perturbation theory would suggest that the optical gap of phenylene oligomers and polymers is linked to the overlap between the π-systems of adjacent phenylene units and that the predominant structural parameter controlling this overlap is the interphenylene torsion angle. Flat structures with torsion angles of ~0° are expected to have maximum π-systems overlap and, as a result, small optical gap values while structures with torsion angles approaching 90° should have large(r) optical gap values not dissimilar to that of the monomer. For the case where torsion angles do not change much with the oligomer length, true for all systems studied here except *o*-phenylene when optimised with standard DFT instead of dispersion corrected DFT+D, one would thus expect to see this also reflected in the trends of optical gap with oligomer length. More specifically, one would expect for the optical gap to smoothly decrease with oligomer length in an approximate *1/n* fashion, and the long oligomer limit of the optical gap ($E_{0\infty}$) of different isomers to be smallest for the isomer with the smallest torsion angles. Indeed *p*-phenylene oligomers have consistently smaller average torsion angles than *o*-phenylene oligomers (37° versus 50°, see Figure 6.4, when concentrating on the DFT+D optimised geometry in the case of *o*-phenylene) and steadily lower optical gap values and a longer effective conjugation length.

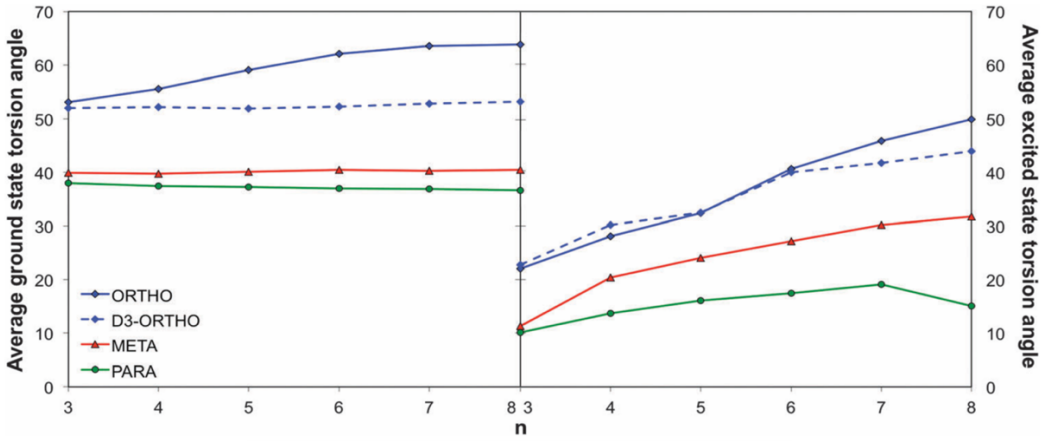

Figure 6.4: TD-B3LYP predicted average ground (right) and excited state (left) interphenylene torsion angles as a function of oligomer length for the different phenylene isomers.

Also, a D_{2h} version of the *p*-phenylene trimer, a transition state with two imaginary frequencies but 90° torsion angles, is predicted by TD-B3LYP to have a much larger optical gap than the *p*-phenylene trimer minimum energy geometry (5.28 *vs.* 4.49 eV), which lies rather close to that predicted for benzene (5.51 eV). The only minor issue with this naïve theoretical picture is that visualisation of the orbitals relevant for the optical gap (*e.g.* HOMO to LUMO excitation in the case of *p*-phenylene, see Figure 6.5), as well as the excited state-ground state density differences, suggest that the naïve picture might be slightly too simple. While the HOMO is typically localised on the constituent phenylene units and has π-like character, the LUMO is predominantly localised along the interphenylene bonds (π-like) with minor π*-like contributions on the phenylene units.

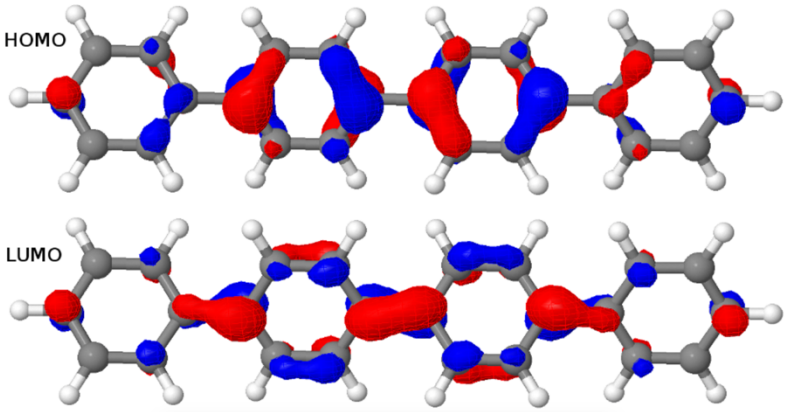

Figure 6.5: HOMO and LUMO for the p-quaterphenyl oligomer.

The case of using standard DFT when describing *o*-phenylene, where the optical gap is predicted to decrease, increase and decrease again (Figure 6.3) is a more complicated. The fact that *o*-phenylene forms helical structures with close contact between non-directly adjacent phenylene units means that a more accurate description of non-covalent dispersion interactions is required than available in standard DFT. As a result, while DFT and dispersion-corrected DFT+D predict essentially identical structures and optical gap values for *p*- and *m*-phenylene, their predictions differ considerably for *o*-phenylene. As can be seen in Figure 6.4, use of standard DFT results in the prediction that the average interphenylene torsion angle of *o*-phenylene increases with oligomer length rather than stay constant. Consequently, the trend in the optical gap for *o*-phenylene and plain DFT is a convolution of two trends; the decrease in optical gap with increasing oligomer length and the increase in the optical gap with increasing torsion angle. It should be noted here that the effect of the dispersion correction is purely structural and single point TD-DFT vertical excitation energy calculations with DFT and DFT+D give identical results.

Which brings us to the non-conjugated nature of *m*-phenylene oligomers. From the average interphenylene torsion angle values for *m*-phenylene in Figure 6.4, it is clear that this lack of conjugation is not due to the torsion angle being close to 90°. As a matter of fact, the average torsion angle values for *o*-phenylene oligomers are only very slightly larger than those of *p*-phenylene oligomers. Having ruled out that the lack of direct geometrical overlap is the origin of the lack of conjugation, we can consider alternative explanations. The most promising of such an alternative explanations is the proposal by Hong and co-workers[10] that the lack of overlap between the π-systems of adjacent phenylene units arises from the fact that the frontier orbitals contributing to this excitation only have small coefficients on the *meta* carbon atoms. Indeed, using DFT we find that for the dimer the atoms in *meta* position with respect to the interphenylene bond have a much lower contribution to the frontier orbitals than the atoms that lie in *para* or *ortho positions*. Similarly, in the valence bond perspective of van Veen and co-workers,[42] *m*-phenylene is cross-conjugated,[43-44] meaning that one cannot conceive a direct pathway involving alternating double and single bonds between more than two phenylene units (see

Figure 6.6), while the other two phenylene isomers are omniconjugated, and possess such pathways.

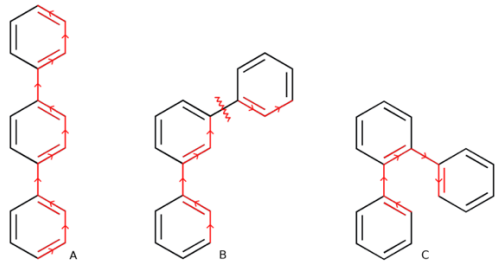

Figure 6.6: Direct pathways of alternating double and single bonds in p- and o-terphenyl (A & C) and absence of such a pathway in m-terphenyl (B).

Both explanations thus suggest that the origin of the lack of conjugation in *m*-phenylene oligomers in a topological rather than a geometric feature. As a result, while the optical gap of *p*- and *o*-phenylene can be controlled by changing the interphenylene torsion angle by tuning of the steric bulk of substituents, this strategy does not work for *m*-phenylene.

The break in conjugation when introducing *m*-phenylene units, finally, can conveniently be observed by modelling an oligomer consisting of two *p*-phenylene regions (3 or 4 units, depending on the perspective) separated by a *m*-phenylene segment in the centre of the molecule (see Figure 6.7). For this oligomers the TD-B3LYP predicted optical gap (4.06 eV) is very similar to the optical gap of an isolated *p*-phenylene tetramer (4.11 eV) and much larger than the value for the *p*-octamer (3.58 eV). This effect can also be observed from the electron density difference between the ground and the excited state, which shows that the lowest energy singlet excitation only involves to the *para*- chain ends (see Figure 6.7).

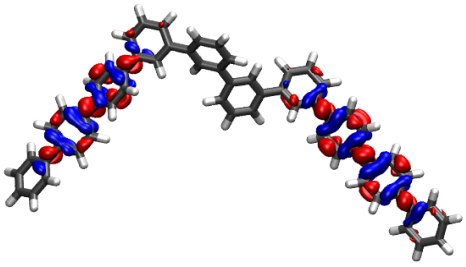

Figure 6.7: TD-B3LYP ground-excited state density difference plot for an oligomer consisting of two p-phenylene regions separated by a m-phenylene segment in the centre of the molecule (negative density difference in blue, positive density difference in red).

6.3.4. Investigating the effect of excited state localisation on fluorescence energies

Just as for the optical gap, all the method combinations used generally agree on the trends of fluorescence energies with respect to oligomer length for the different phenylene isomers (see Figure 6.8). However, as expected from the literature[2-3, 7-8] these predicted trends are very different from one isomer to the other. The *m*-phenylene isomers are predicted to have the highest fluorescence energies, of the order of 3.8 eV in the case of TD-B3LYP, and show effectively no variation in fluorescence energy with oligomer length.

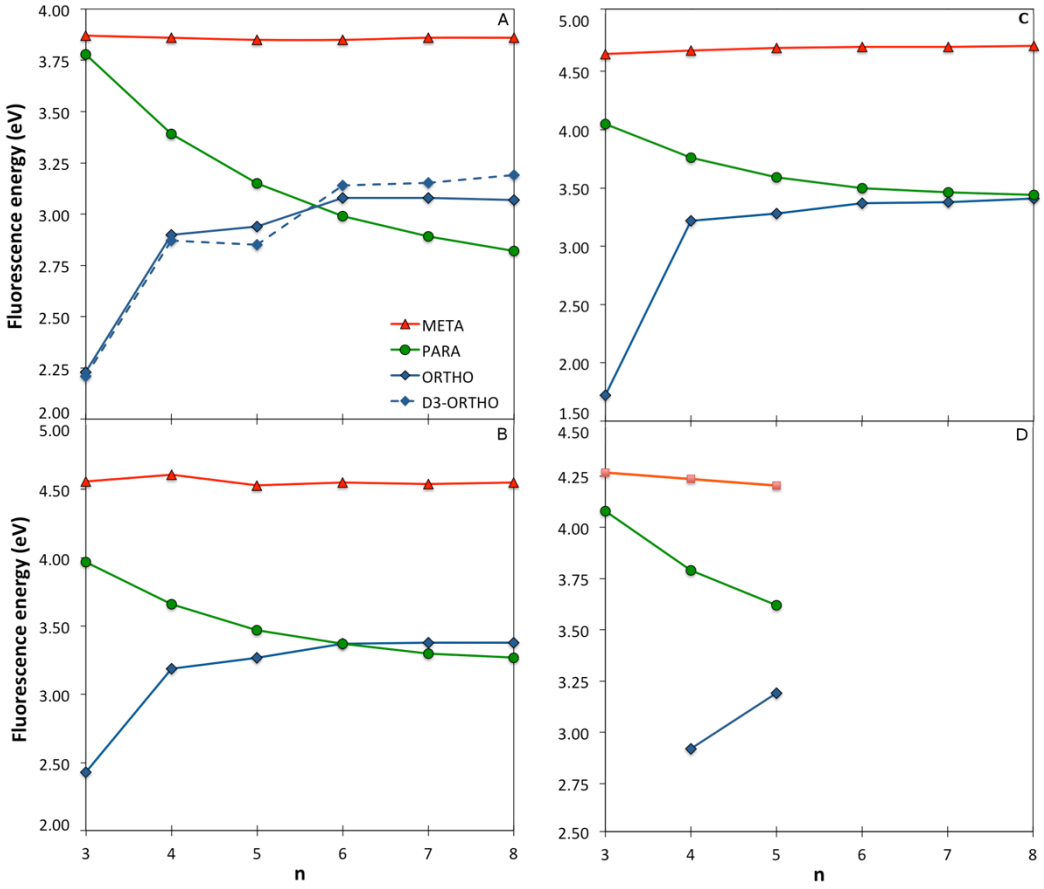

Figure 6.8: Fluorescence energy values as a function of oligomer length for the different phenylene isomers calculated with TD-B3LYP (A), BHLYP (B), CAM-B3LYP (C) and RI-CC2 (D).

The fluorescence energies of *p*-phenylene isomers, in contrast, show a distinct red shift with increasing oligomer length, while calculations predict a rather unique blue

shift in fluorescence energies for the *o*-phenylene isomers. The only structure where there is contention about the description is *o*-terphenylene. Here, TD-DFT calculations with all XC-potentials considered predict an excited state minimum, while RI-CC2 finds what appears to be a conical intersection between the ground and lowest excited state potential energy surface, where all three phenylene rings end up lying in approximately the same plane.

Having discussed the trend in fluorescence with oligomer length, I will now move on to an in-depth discussion of the differences in excited state relaxation and fluorescence between the different phenylene isomers. Here, the focus is on the results obtained using (TD-)B3LYP but, where insightful, the predictions of excited state relaxation calculations using the other XC-potential, as well as RI-CC2, will also be referred to. Concentrating first on the Stokes shift and its contributions due to the stabilisation of the excited state (Excited State Stabilisation Energy, ESSE) and destabilisation of the ground state (Ground State Destabilisation Energy, GSDE, see Figure 6.9), we observe a gradual increase for *p*-phenylene in the Stokes shift with oligomer length, and the contributions of the ESSE are roughly 25% larger than those of the GSDE.

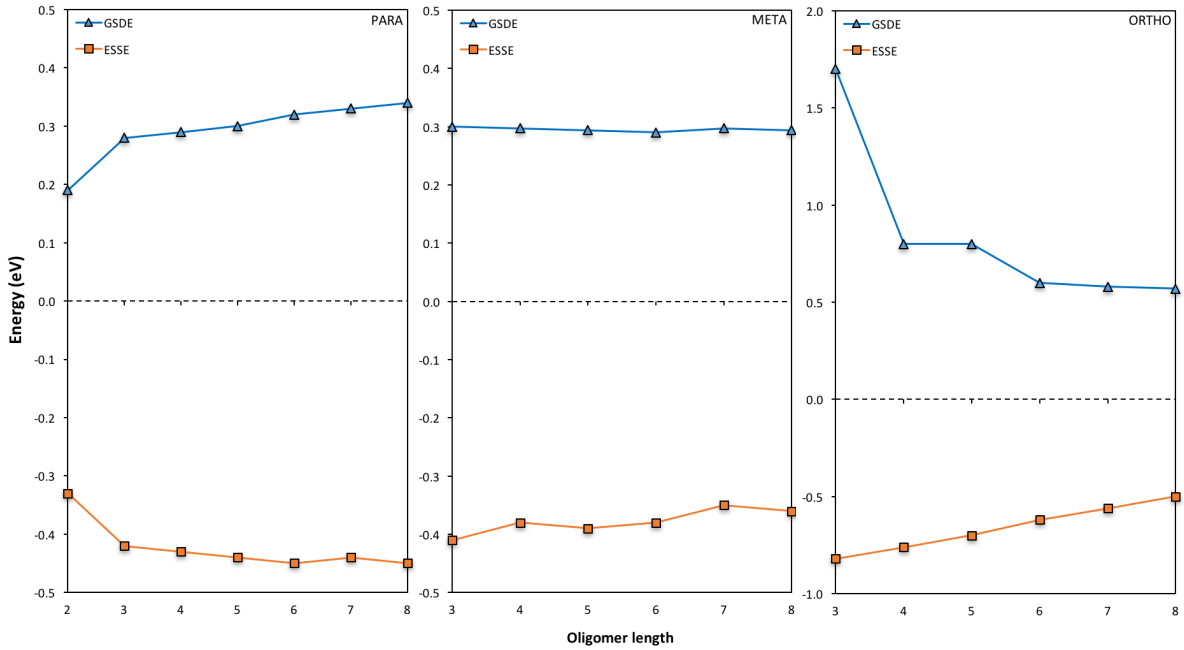

Figure 6.9: Variation in the ESSE and GSDE with oligomer length for p-phenylene (left), m-phenylene (centre), and o-phenylene (right, N.B.: different energy scale).

For *o*-phenylene, in contrast, though in line with the blue shift observed in the fluorescence energy, the Stokes shift decreases with increasing oligomer length, however, not as smoothly as for *p*-phenylene. Use of (TD-)B3LYP+D (which is not necessarily a panacea in this case, because the parameters of the dispersion correction should in principle be different for the ground and excited state, but are not in practice) also yields slightly different results than obtained when using standard (TD-)B3LYP.

Both methods, however, do agree that for the shorter *o*-phenylene oligomers, the GSDE is considerably larger than the ESSE, while for the longer oligomers they are of similar magnitude. Finally, the Stokes shift of the *m*-phenylene oligomers is, just like their optical gap and fluorescence energy, virtually independent of oligomer length and is the smallest in magnitude of all three isomers; just as for *p*-phenylene, the ESSE contribution is approximately 25% larger than that due to GSDE. Overall, it is clear that the Stokes shift does not merely find its origin in the stabilisation of the excited state but also has a large component due to the destabilisation of the ground state, at the excited state minimum energy geometry.

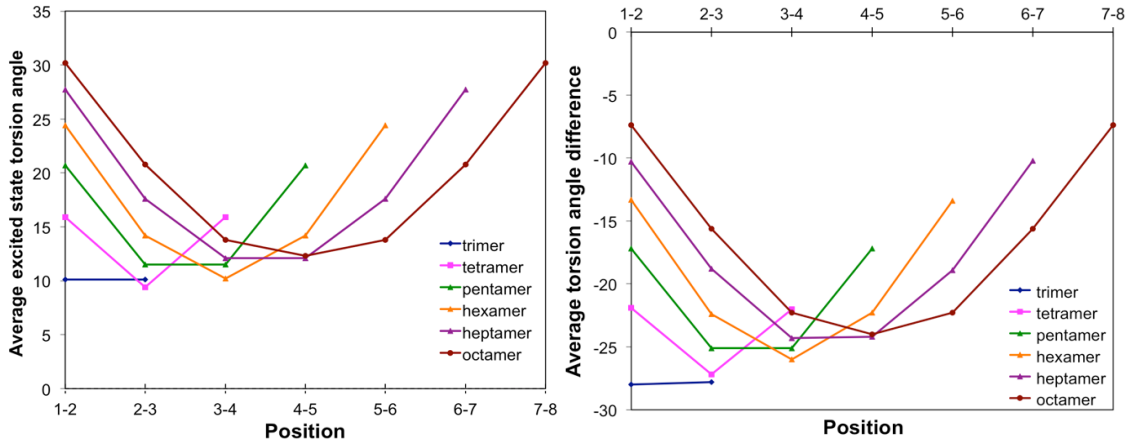

Figure 6.10: Variation of the TD-B3LYP calculated excited state interphenylene torsion angles (left) and ground state-excited state interphenylene torsion angle difference (right) along the oligomer, for the different p-phenylene oligomers.

A structural comparison of TD-B3LYP geometries shows that in the case of *p*-phenylene oligomers, the main differences between the ground and relaxed excited state minimum energy structures responsible for the fluorescence are: (i) a decrease

in the interphenylene torsion angles relative to those in the ground state (see Figure 6.4 in the previous section, and Figure 6.10 above) and (ii) a *para-quinone* like distortion of the bond lengths (see Figure 6.11). Both distortions are in all cases symmetrically delocalised over the whole chain with the largest distortion in the centre.

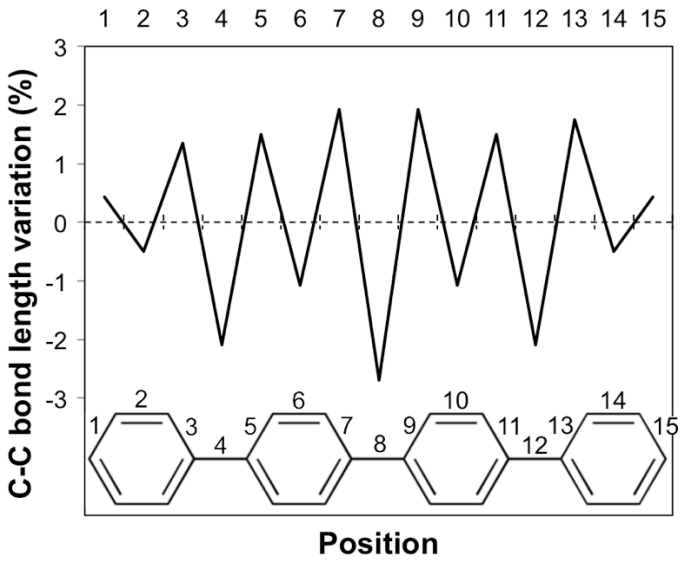

Figure 6.11: Para-quinone bond length distortion for the p-phenylene tetramer.

For *o*-phenylene, a similar reduction in torsion angles relative to the ground state is observed (see Figure 6.4 in the previous section, and Figures 6.12 and 6.13 below) but now combined with an *ortho* rather than a *para-quinone* like distortion of the bond lengths (as previously discussed by Hartley,[8] see Figure 6.14). Interestingly, the reduction of the torsion angle and the *ortho-quinone* like distortion of the bond lengths go together with two other types of distortions that are essentially unique to the excited state minimum of o-phenylene oligomers. Firstly, (i) there is a significant distortion of the planarity of the phenylene unit and, secondly, (ii) after excited state relaxations, the interphenylene bonds typically do not lie (anymore) in the same plane as either of the phenylene units they connect.

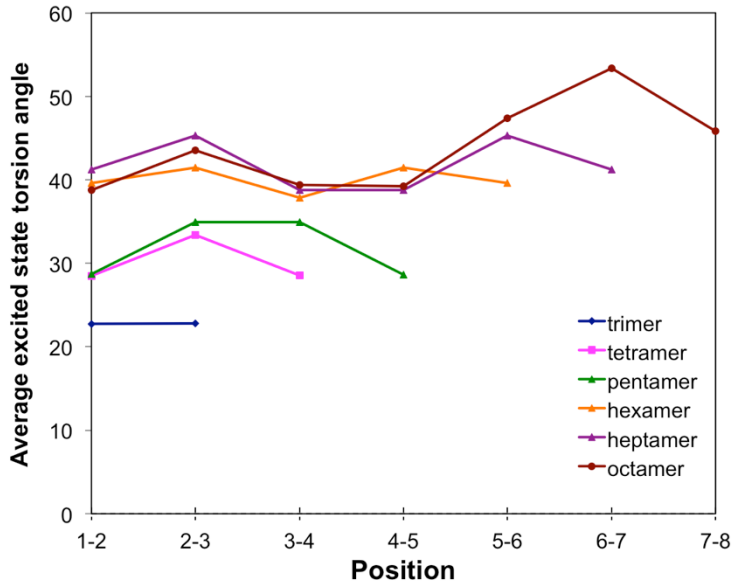

Figure 6.12: Variation of the TD-B3LYP+D calculated excited state interphenylene torsion angles along the oligomer for the different o-phenylene oligomers.

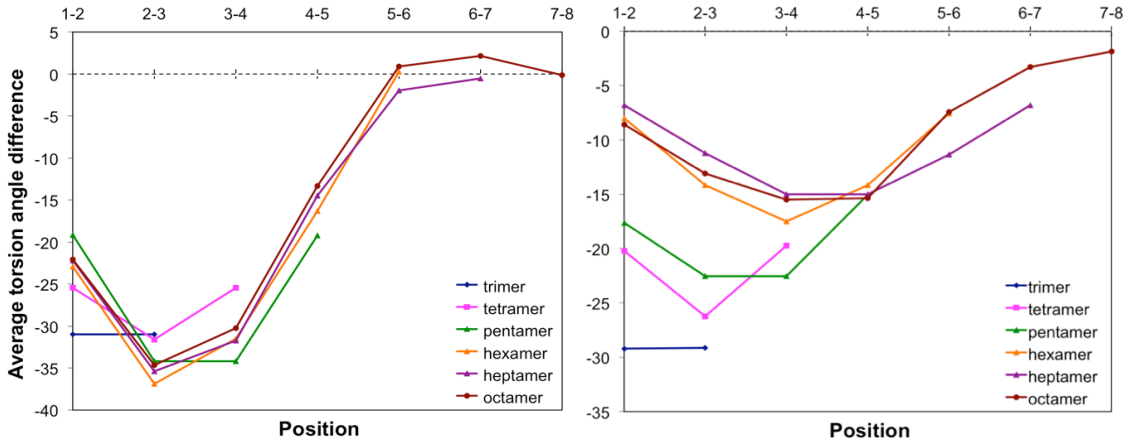

Figures 6.13: Variation of the TD-B3LYP (left) and TD-B3LYP+D (right) calculated ground state-excited state interphenylene torsion angle difference along the oligomer for the different o-phenylene oligomers.

Both of these latter "planarity" distortions are to a certain extent already present in the ground state structure of *o*-phenylene oligomers but become magnified enormously after excited state relaxation. A tell-tale sign, finally, of (ii) is that the magnitude of the torsion angle between two phenylene units is different depending on which pair of atoms are chosen (beyond those directly involved in the phenylene-phenylene bond) to represent the interphenylene torsion angle, by up to approximately 20° (see torsion angles 1-2-3-4 and 1'-2-3-4' in Figure 6.15). Taking

this into account, the values reported in Figure 6.4 and Figures 6.12 and 6.13 are thus averages of the two unique angle choices.

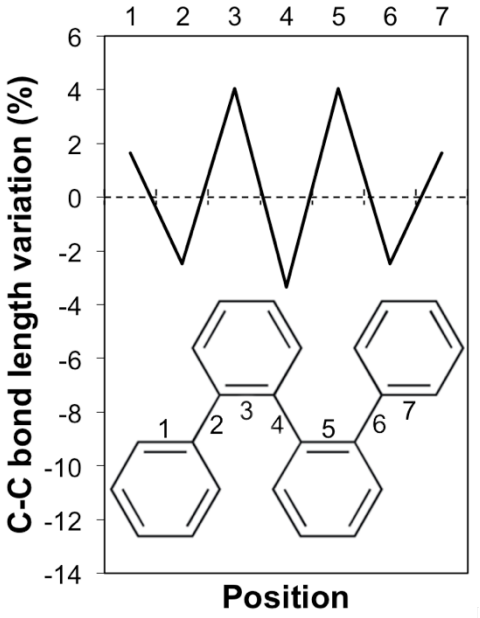

Figure 6.14: Ortho-quinone bond length distortion for the o-phenylene tetramer.

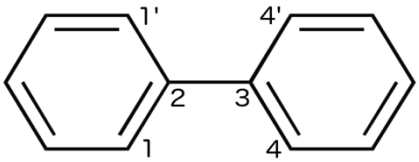

Figure 6.15: The two unique torsion angle choices 1–2–3–4 and 1'-2-3-4'.

The number of phenylene units involved in the distortion and the degree to which it is predicted to be symmetric differ with oligomer length, and the use of dispersion correction with TD-B3LYP+D predicts that the excited state minima remain symmetrical up to the heptamer, where the excited state is most likely delocalised over the whole oligomer length. The maximum distortion relative to the ground state structure is for all these oligomers in the centre of the chain and the flattest torsion angles generally occur at either end of the oligomer. For the octamer, in contrast, TD-B3LYP+D predicts an asymmetric excited state minimum, where the excited state appears to localise on one side of the oligomer. Use of plain TD-B3LYP yields symmetric excited state minima with a delocalised excited state, for oligomers up to and including the pentamer, and asymmetric structures for the longer oligomers, where the excited state has localised on one site of the chain (similar to

that of the TD-B3LYP+D octamer excited state minimum). The increase of selected torsion angles far away from where the excited state localises in asymmetric excited state minima (*i.e.* torsion angles that are actually larger than in the ground state structure, as previously observed by Hartley[8]) is only observed in my calculations in the absence of dispersion correction. RI-CC2 calculations, finally, only numerically tractable for up to the pentamer, yield symmetric excited state minima, similar to those found with TD-B3LYP+D and plain TD-B3LYP.

For *m*-phenylene, finally, excited state relaxation results in an extremely well localised excited state (see Figure 6.4 in the previous section, and Figure 6.16 below). In line with the lack of conjugation in this isomer, already discussed previously, only two adjacent torsion angles and the associated two interphenylene bond distances are always significantly distorted.

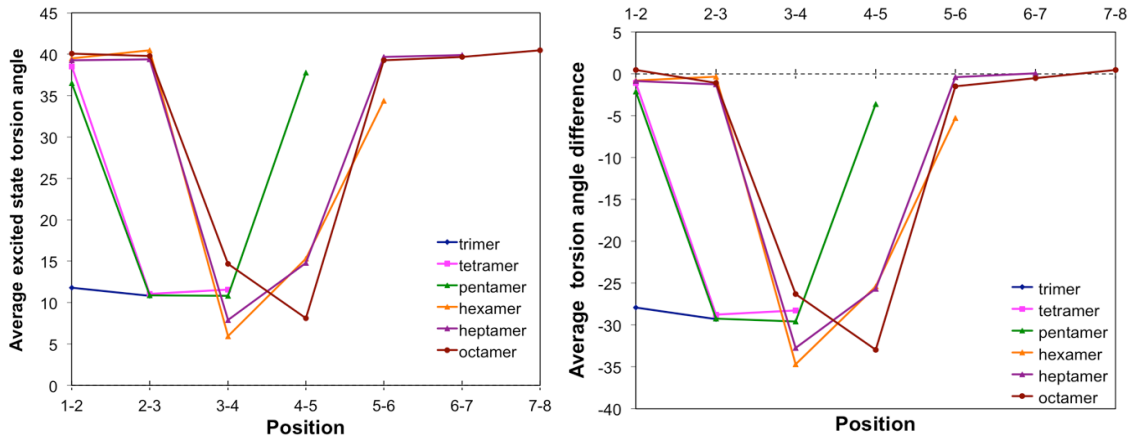

Figure 6.16: Variation of the TD-B3LYP calculated excited state interphenylene torsion angles (left) and ground state-excited state interphenylene torsion angle difference (right) along the oligomer, for the different p-phenylene oligomers.

The distortion in terms of intraphenylene bond distance changes (see Figure 6.17) is limited to the three phenylene units around these torsion angles and does not follow a simple pattern, perhaps because there is no such thing as a *meta-quinone* like distortion.

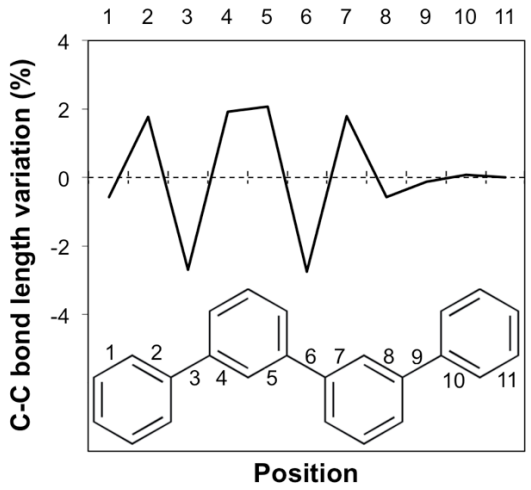

Figure 6.17: Bond length distortion for the m-phenylene tetramer.

6.3.5. Instability of *o*-terphenyl

This brings us to a reflection on the description of excited state relaxation in *o*-terphenyl by TD-DFT and RI-CC2. As the RI-CC2 method is known to struggle with the description of conical intersections due to their inherent multi-reference nature, and as the D1 diagnostic[45] that probes for possible multi-reference issue within the context of RI-CC2 indeed soars at this point to 0.26, one must be careful not to over interpret the RI-CC2 result for *o*-terphenyl. However, *o*-terphenyl is an exception amongst the (*o*-)phenylene oligomers, as it is known experimentally to undergo photocyclisation to *4a,4b*-dihydrotriphenylene (DHT) *via* a conical intersection[46-47] rather than display fluorescence,[8] shedding doubt on the TD-DFT excited state optimisation results for this particular structure.

The observed instability is probably related to the fact that the pattern of bond-length elongations and contractions associated with the excited state *ortho-quinone* like distortion is similar to the bond length pattern in the ground state structure of DHT. The longer *o*-phenylene oligomers also display the same *ortho-quinone* like distortion, but the steric repulsions with the rest of the oligomer means that in these cases, a section of three adjacent phenylene units cannot become approximately coplanar, ruling out cyclisation and explaining why these structures are fluorescent instead.

6.3.6. Understanding the fundamental difference between *o*- and *p*-phenylene

This investigation leaves two pertinent interrelated questions to consider; (i) why, for shorter oligomers, is the fluorescence energy of *p*-phenylene larger than that of *o*-phenylene oligomers, and (ii) why, for *o*-phenylene, does the fluorescence energy increase with oligomer length rather than decrease as generally observed for polymers? Both issues are known, as a result of the RI-CC2 calculations, not to be artefacts of the use of TD-DFT or a particular XC-potential.

Focussing first on the question of the origin of the difference between *o*- and *p*-phenylene, it is clear that this cannot be simply related to the magnitude of the excited state interphenylene torsion angle. Comparing oligomers of similar size, the torsion angles in the excited state structure of *o*-phenylene are consistently significantly larger than that of *p*-phenylene (see Figures 6.4, 6.10 and 6.12). As the excited state for these smaller oligomers is always delocalised, one would thus, based on the link between torsion angle and π-systems overlap, naively have expected the fluorescence energy of *o*-phenylene to be larger than that of *p*-phenylene. Similarly, for short *o*- and *p*-phenylene oligomers, the change in torsion angle between the ground and excited state is similar in magnitude but the Stokes shift (and its ESSE and GSDE components) is much larger in the case of *o*-phenylene than for *p*-phenylene oligomers of the same size. Also, the excited state interphenylene bond distances of *o*- and *p*-phenylene oligomers of the same size are very similar (see Figure 6.18), suggesting no link between this structural degree of freedom and the fact the fluorescence energy of *p*-phenylene is larger than that of *o*-phenylene either. Finally, partial excited state optimisation of dimeric clusters cut from the *o*-phenylene trimer and tetramer excited state minima, where all atoms but the newly added one or two terminating hydrogen atoms are held fixed, have larger fluorescence energies than the fully optimised dimer. The planarity distortions thus also cannot explain the low *o*-phenylene fluorescence energies, at least not for dimer fragments.

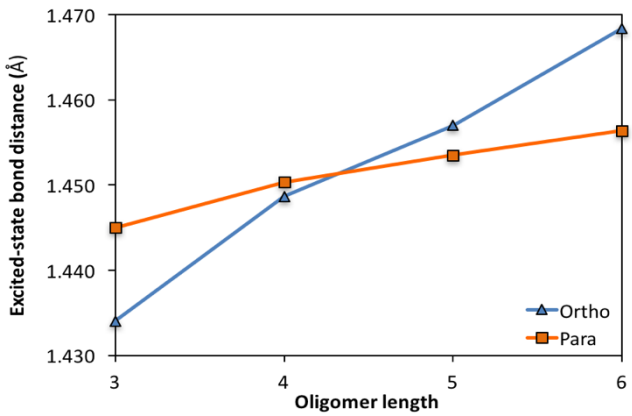

Figure 6.18: Variation in average excited state interphenylene bond length with oligomer length, for o- and p-phenylene.

Having effectively ruled out most structural explanations, it thus stands to reason that the lower fluorescence energies of short *o*-phenylene oligomers relative to their *p*-phenylene counterparts must find its origin in the inherent electronic structure of *o*-phenylene in general, and the presence of an *ortho*- rather than a *para-quinone* like distortion in particular, as the optical gap appears well behaved. Support for this hypothesis comes from the observation that, independent of the XC-potential employed and oligomer length, the difference between the Kohn-Sham orbital energy gap for the pair(s) of orbitals responsible for the lowest energy TD-DFT excitation and its TD-DFT energy is always considerably larger for *o*-phenylene than for *p*-phenylene. For example, in the case of TD-B3LYP, the energy difference between the Kohn-Sham gap and the lowest TD-B3LYP excitation energy is of the order of 0.1 - 0.2 eV for the *p*-phenylene oligomer excited state minima and 0.4 - 0.6 eV for their *o*-phenylene counterparts. In linear response TD-DFT the Kohn-Sham gap is the zeroth-order approximation to the lowest TD-DFT excitation energy, with all higher-order corrections due to a combination of the contributions of the Hartree and XC kernel (f_{xc}, the functional derivative of the XC-potential with respect to the density[48]). The larger difference between the Kohn-Sham gap and lowest TD-DFT excitation energy for *o*-phenylene oligomers thus suggest that the Hartree and f_{xc} correction is much larger for *o*-phenylene than for *p*-phenylene and that the two oligomers indeed fundamentally differ in their many-body electronic structure beyond simply the constituting Kohn-Sham orbitals.

Which brings us, finally, to the question of the origin of the characteristic blue shift of the fluorescence energies of *o*-phenylene oligomers with increasing oligomer length. Focussing on the oligomers with symmetric excited state minima and delocalised excited states, it is clear that the torsion angles of the excited state minima steadily increase with oligomer length for *o*-phenylene (*e.g.* in terms of the average torsion angle for TD-B3LYP+D, an increase from 23° for the trimer to 40° for the hexamer, see Figure 6.4). For *p*-phenylene there is also an increase in the excited state torsion angle with oligomer length but the magnitude of the change is considerably smaller than for *o*-phenylene (*e.g.* in terms of the average torsion angle for TD-B3LYP an increase from 10° for the trimer to 17° for the hexamer, see Figure 6.4). If one assumes that the change of fluorescence energy with oligomer length is a balance between two competing effects (the decrease in excitation energy with increasing oligomer length and the increase in excitation energy with increasing torsion angle), then it appears that different terms dominate for *o*-phenylene and *p*-phenylene. For *p*-phenylene oligomers, the increase in torsion angle with oligomer size is relatively small and the decrease in excitation energy with increasing oligomer length dominates, resulting in the conventional red shift in fluorescence energy with oligomer length, while for *o*-phenylene oligomers, the increase in excitation energy with increasing torsion angle dominates, giving rise to the rather unique blue shift with oligomer length.

The large change in torsion angle with increasing *o*-phenylene oligomer length, finally, is probably related to an increase in steric repulsion due to a growth of the number of intraoligomer close arene-arene π-stacking contacts with increasing oligomer length (*i.e.* 0, 1, 2 and 3 for n = 3, 4, 5 and 6 respectively). Such close arene-arene π-stacking contacts are completely absent in *p*-phenylene oligomers and all other "straight" conjugated polymers, while for helical structures their effect probably decreases with increasing size of the pitch (4 in the case of *o*-phenylene), explaining why a blue shift in fluorescence energy with increasing oligomer length is such a rare phenomenon.

6.4. Conclusions

In conclusion, I showed through a combination of TD-DFT and approximate correlated wavefunction RI-CC2 calculations that the three isomers of oligophenylene, while chemically similar, display quite different absorption and especially fluorescence properties. More specifically, both TD-DFT and RI-CC2 predict that all *m*-phenylene oligomers essentially have the same fluorescence signature, while the fluorescence energy of *p*-phenylene oligomers decreases with oligomer length, and that of *o*-phenylene increases. In the case of *m*-phenylene I discuss that the lack of change in fluorescence energy with oligomer length is a topological feature of the bonding in phenylene, while the difference between *o*- and *p*-phenylene arises from a combination of steric and electronic factors. I further show that these electronic factors, interestingly, result in the fluorescence of small *o*-phenylene oligomers to be significantly red shifted relative to their *p*-phenylene counterparts.

Following on from that, I argue that the rarity of a blue shift in fluorescence energy with increasing oligomer length, as observed for *o*-phenylene oligomers, is probably related to the absence of close intraoligomer arene-arene π-stacking contacts in most other oligomers and polymers. Finally, I hypothesise that the reason that *o*-terphenyl experimentally photocyclises to *4a,4b*-dihydrotriphenylene while the longer *o*-phenylene oligomers do not, and are fluorescent, is due to the fact that the steric bulk of the longer oligomers do not allow for the planarisation required for cyclisation.

6.5. References

1. Seoul, C.; Song, W.-J.; Kang, G.-W.; Lee, C., "Effect of molar mass on electroluminescence of poly(p-phenylene)", *Synthetic Metals* **2002**, *130*, 9-16.
2. Artacho, E.; Rohlfing, M.; Côté, M.; Haynes, P. D.; Needs, R. J.; Molteni, C., *Phys Rev. Lett.* **2004**, *93*, 116401.
3. Lukeš, V.; Aquino, A. J. A.; Lischka, H.; Kauffmann, H.-F., "Dependence of Optical Properties of Oligo-para-phenylenes on Torsional Modes and Chain Length", *The Journal of Physical Chemistry B* **2007**, *111*, 7954-7962.
4. Banerjee, M.; Shukla, R.; Rathore, R., *Journal of the American Chemical Society* **2009**, *131*, 1780-1786.
5. Park, K.; Lee, T.-W.; Yoon, M.-J.; Choe, J.-I., "Calculated and Experimental UV and IR Spectra of Oligo-para-phenylenes", *Bulletin of the Korean Chemical Society* **2014**, *35*, 531-538.
6. He, J.; Crase, J. L.; Wadumethrige, S. H.; Thakur, K.; Dai, L.; Zou, S.; Rathore, R.; Hartley, C. S., "ortho-Phenylenes: Unusual Conjugated Oligomers with a Surprisingly Long Effective Conjugation Length", *Journal of the American Chemical Society* **2010**, *132*, 13848-13857.
7. Mathew, S. M.; Hartley, C. S., "Parent o-Phenylene Oligomers: Synthesis, Conformational Behavior, and Characterization", *Macromolecules* **2011**, *44*, 8425-8432.
8. Hartley, C. S., "Excited-state behavior of ortho-phenylenes", *J Org Chem* **2011**, *76*, 9188-91.
9. Mathew, S. M.; Engle, J. T.; Ziegler, C. J.; Hartley, C. S., "The Role of Arene-Arene Interactions in the Folding of ortho-Phenylenes", *Journal of the American Chemical Society* **2013**, *135*, 6714-6722.
10. Hong, S. Y.; Kim, D. Y.; Kim, C. Y.; Hoffmann, R., "Origin of the Broken Conjugation in m-Phenylene Linked Conjugated Polymers", *Macromolecules* **2001**, *34*, 6474-6481.
11. Grem, G.; Leditzky, G.; Ullrich, B.; Leising, G., "Realization of a blue-light-emitting device using poly(p-phenylene)", *Advanced Materials* **1992**, *4*, 36-37.
12. Yanagida, S.; Kabumoto, A.; Mizumoto, K.; Pac, C.; Yoshino, K., "Poly(p-phenylene)-catalysed photoreduction of water to hydrogen", *Journal of the Chemical Society, Chemical Communications* **1985**, 474-475.
13. Shibata, T.; Kabumoto, A.; Shiragami, T.; Ishitani, O.; Pac, C.; Yanagida, S., "Novel visible-light-driven photocatalyst. Poly(p-phenylene)-catalyzed photoreductions of water, carbonyl compounds, and olefins", *Journal of Physical Chemistry* **1990**, *94*, 2068-2076.
14. Matsuoka, S.; Kohzuki, T.; Pac, C.; Yanagida, S., "Photochemical Reduction of Carbon Dioxide to Formate Catalyzed by p-Terphenyl in Aprotic Polar Solvent", *Chemistry Letters* **1990**, *19*, 2047-2048.
15. Matsuoka, S.; Fujii, H.; Yamada, T.; Pac, C.; Ishida, A.; Takamuku, S.; Kusaba, M.; Nakashima, N.; Yanagida, S., "Photocatalysis of oligo(p-phenylenes): photoreductive production of hydrogen and ethanol in aqueous triethylamine", *The Journal of Physical Chemistry* **1991**, *95*, 5802-5808.

16. Sprick, R. S.; Jiang, J.-X.; Bonillo, B.; Ren, S.; Ratvijitvech, T.; Guiglion, P.; Zwijnenburg, M. A.; Adams, D. J.; Cooper, A. I., "Tunable Organic Photocatalysts for Visible Light-Driven Hydrogen Evolution", *Journal of the American Chemical Society* **2015**, *137*, 3265-3270.
17. Hohenberg, P.; Kohn, W., "Inhomogeneous Electron Gas", *Physical Review* **1964**, *136*, 864-871.
18. Kohn, W.; Sham, L. J., "Self-Consistent Equations Including Exchange and Correlation Effects", *Physical Review* **1965**, *140*, 1133-1138.
19. Runge, E.; Gross, E. K. U., "Density-Functional Theory for Time-Dependent Systems", *Physical Review Letters* **1984**, *52*, 997-1000.
20. Christiansen, O.; Koch, H.; Jørgensen, P., "The second-order approximate coupled cluster singles and doubles model CC2", *Chemical Physics Letters* **1995**, *243*, 409-418.
21. Jorgensen, W. L.; Tirado-Rives, J., "The OPLS [optimized potentials for liquid simulations] potential functions for proteins, energy minimizations for crystals of cyclic peptides and crambin", *Journal of the American Chemical Society* **1988**, *110*, 1657-1666.
22. Kolossváry, I.; Guida, W. C., "Low Mode Search. An Efficient, Automated Computational Method for Conformational Analysis: Application to Cyclic and Acyclic Alkanes and Cyclic Peptides", *Journal of the American Chemical Society* **1996**, *118*, 5011-5019.
23. Mohamadi, F.; Richards, N. G. J.; Guida, W. C.; Liskamp, R.; Lipton, M.; Caufield, C.; Chang, G.; Hendrickson, T.; Still, W. C., "Macromodel—an integrated software system for modeling organic and bioorganic molecules using molecular mechanics", *Journal of Computational Chemistry* **1990**, *11*, 440-467.
24. Vosko, S. H.; Wilk, L.; Nusair, M., "Accurate spin-dependent electron liquid correlation energies for local spin density calculations: a critical analysis", *Canadian Journal of Physics* **1980**, *58*, 1200-1211.
25. Lee, C.; Yang, W.; Parr, R. G., "Development of the Colle-Salvetti correlation-energy formula into a functional of the electron density", *Physical Review B* **1988**, *37*, 785-789.
26. Becke, A. D., "Density-functional thermochemistry. III. The role of exact exchange", *Journal of Chemical Physics* **1993**, *98*, 5648-5652.
27. Stephens, P. J.; Devlin, F. J.; Chabalowski, C. F.; Frisch, M. J., "Ab Initio Calculation of Vibrational Absorption and Circular Dichroism Spectra Using Density Functional Force Fields", *The Journal of Physical Chemistry* **1994**, *98*, 11623-11627.
28. Yanai, T.; Tew, D. P.; Handy, N. C., "A new hybrid exchange-correlation functional using the Coulomb-attenuating method (CAM-B3LYP)", *Chemical Physics Letters* **2004**, *393*, 51-57.
29. Hirata, S.; Head-Gordon, M., "Time-dependent density functional theory within the Tamm-Dancoff approximation", *Chemical Physics Letters* **1999**, *314*, 291-299.
30. Peach, M. J. G.; Williamson, M. J.; Tozer, D. J., "Influence of Triplet Instabilities in TDDFT", *Journal of Chemical Theory and Computation* **2011**, *7*, 3578-3585.
31. Grimme, S.; Antony, J.; Ehrlich, S.; Krieg, H., "A consistent and accurate ab initio parametrization of density functional dispersion correction (DFT-D)

for the 94 elements H-Pu", *The Journal of Chemical Physics* **2010**, *132*, 154104.
32. Grimme, S., "Density functional theory with London dispersion corrections", *Wiley Interdisciplinary Reviews: Computational Molecular Science* **2011**, *1*, 211-228.
33. Grimme, S.; Ehrlich, S.; Goerigk, L., "Effect of the damping function in dispersion corrected density functional theory", *Journal of Computational Chemistry* **2011**, *32*, 1456-1465.
34. Schäfer, A.; Horn, H.; Ahlrichs, R., *Journal of Chemical Physics* **1992**, *97*, 2571.
35. Hehre, W. J.; Ditchfield, R.; Pople, J. A., "Self---Consistent Molecular Orbital Methods. XII. Further Extensions of Gaussian---Type Basis Sets for Use in Molecular Orbital Studies of Organic Molecules", *The Journal of Chemical Physics* **1972**, *56*, 2257-2261.
36. Weigend, F.; Ahlrichs, R., "Balanced basis sets of split valence, triple zeta valence and quadruple zeta valence quality for H to Rn: Design and assessment of accuracy", *Physical Chemistry Chemical Physics* **2005**, *7*, 3297-3305.
37. Ahlrichs, R.; Bär, M.; Häser, M.; Horn, H.; Kölmel, C., "Electronic structure calculations on workstation computers: The program system turbomole", *Chemical Physics Letters* **1989**, *162*, 165-169.
38. van Wüllen, C., "Shared-memory parallelization of the TURBOMOLE programs AOFORCE, ESCF, and EGRAD: How to quickly parallelize legacy code", *Journal of Computational Chemistry* **2011**, *32*, 1195-1201.
39. Valiev, M.; Bylaska, E. J.; Govind, N.; Kowalski, K.; Straatsma, T. P.; Van Dam, H. J. J.; Wang, D.; Nieplocha, J.; Apra, E.; Windus, T. L.; de Jong, W. A., "NWChem: A comprehensive and scalable open-source solution for large scale molecular simulations", *Computer Physics Communications* **2010**, *181*, 1477-1489.
40. Schmidt, M. W.; Baldridge, K. K.; Boatz, J. A.; Elbert, S. T.; Gordon, M. S.; Jensen, J. H.; Koseki, S.; Matsunaga, N.; Nguyen, K. A.; Su, S.; Windus, T. L.; Dupuis, M.; Montgomery, J. A., "General atomic and molecular electronic structure system", *Journal of Computational Chemistry* **1993**, *14*, 1347-1363.
41. Meier, H.; Stalmach, U.; Kolshorn, H., *Acta Polymerica* **1997**, *48*, 379-384.
42. van der Veen, M. H.; Rispens, M. T.; Jonkman, H. T.; Hummelen, J. C., "Molecules with Linear π-Conjugated Pathways between All Substituents: Omniconjugation", *Advanced Functional Materials* **2004**, *14*, 215-223.
43. Trætteberg, M.; Hopf, H., "Cross-Conjugation: A Theoretical and Experimental Study of the Molecular Structure of 2-Ethynyl-1,3-butadiene.", *Acta Chemica Scandinavica* **1994**, *48*, 989-993.
44. Gholami, M.; Tykwinski, R. R., "Oligomeric and polymeric systems with a cross-conjugated pi-framework", *Chemical reviews* **2006**, *106*, 4997-5027.
45. Janssen, C. L.; Nielsen, I. M. B., "New diagnostics for coupled-cluster and Møller–Plesset perturbation theory", *Chemical Physics Letters* **1998**, *290*, 423-430.
46. Kharasch, N.; Alston, T. G.; Lewis, H. B.; Wolf, W., "The photochemical conversion of o-terphenyl into triphenylene", *Chemical Communications (London)* **1965**, 242-243.
47. Molloy, M. S.; Snyder, J. A.; Bragg, A. E., "Structural and Solvent Control of Nonadiabatic Photochemical Bond Formation: Photocyclization of o-

Terphenyl in Solution", *The Journal of Physical Chemistry A* **2014**, *118*, 3913-3925.

48. Marques, M. A.; Maitra, N. T.; Nogueira, F. M.; Gross, E. K.; Rubio, A., *Fundamentals of time-dependent density functional theory*. Springer: 2012; Vol. 837.

CHAPTER 7:

Summary and perspectives

In this thesis, I introduced a new computational approach based on (TD-)DFT that can be used to systematically calculate the standard reduction potentials of target conjugated oligomers and polymers, in order to assess their relevance as water splitting photocatalysts. Unlike other methods based on static DFT, this methodology takes into account electronic excitations, considers both charge carriers and excitons, and is therefore more realistic when modelling processes that involve chemical systems in their excited state. It is computationally simple to implement, tractable for relatively small molecular clusters (up to ~200 atoms), and yields exploitable predictions within short timescales (a few hours to a few days). This approach can be used to rapidly screen for new promising photocatalysts for water splitting, possibly with high throughput. However, as it only takes thermodynamic effects into consideration, and neglects important kinetic processes that happen in materials (*e.g.* exciton dissociation, transport of recombination of charge carriers) as well as some of their intrinsic properties (*e.g.* wettability, porosity, surface area, interfaces, defects), its real strength resides in its ability to consistently rule out materials that are inherently bad choices for such an application, before synthesising and characterising them (*i.e.* that do not and will never, according to our calculations, have sufficient thermodynamic force to drive proton reduction, like poly(*p*-phenylene), or water oxidation, like polypyrrole, on their own). Predictions of the (relative) photocatalytic activity of a material therefore largely remain out of reach. Additionally, one must be careful when employing this computational methodology to study systems where charge-transfer or multiple excitations are likely to occur, situations in which (TD-)DFT is known to struggle.

This methodology was then tested; the calculated standard reduction potentials were compared to experimental results from IP/EA measurements in the literature, and the predicted performance of some oligomers and polymers was confronted to photocatalytic measurements by our collaborators, the Cooper Group, at the University of Liverpool. Overall, despite the lack of consistent and reliable measurements, especially for IP*/EA*, a good fit was found for IP values, and a decent fit for EA values, for samples measured in the solid state, although such accuracy might be due to error-cancellation among the theoretical tools used. A poor fit, however, was found for the potentials of *p*-phenylene and fluorene oligomers in gas phase and solution. Some of the optical properties of *p*-phenylene (absorption onset) were also compared to experimental results from the literature, with a very good fit.

I then applied the methodology to a wide range of cluster models of oligomers. Firstly, for PPP, it confirmed the material's thermodynamic ability for to drive hydrogen evolution, but showed that it is fundamentally unlikely to drive oxygen evolution for thermodynamic reasons. Secondly, for a range of linear oligomers, calculations showed that oligomers can be designed and their shape and chemical functions changed, to tune their optical properties and thermodynamic potentials to desired levels, by adjusting the electron-rich or electron-poor character of its monomers. Thirdly, moving on to 2D and 3D molecular clusters (CTFs and CMPs), it confirmed that the optical/fundamental gaps, intrinsically tied to the positions of IP/IP* and EA/EA* levels, can have a dramatic influence on the overall photocatalytic performance of a system (*e.g.* some materials might absorb a larger part of the visible spectrum than others, or absorb at very different wavelengths, *e.g.* UV *vs.* visible). Finally, considering the particular case of carbon nitride, although it had been experimentally unable to drive overall WS, the computational methodology predicted that carbon nitride had suitable thermodynamic potentials to drive both water splitting half-reactions, which was finally achieved experimentally in the last couple of years.[1-2]

Throughout the thesis, the role of excitons was emphasised, as the computational approach predicted that many oligomers relevant to water splitting had IP* and EA*

values that were well positioned, *i.e.* that excitons themselves could often drive the proton reduction and/or water oxidation half-reactions directly. The observation that excitons in conjugated polymers are so strongly bound (*i.e.* often have high exciton binding energies) that they do not spontaneously fall apart in the bulk, was confirmed through comparison to experimental results. Therefore, in such cases, charge carriers must be generated by the dissociation of excitons at an interface, such as the polymer-solution interface, or a polymer-polymer interface in the case of heterogeneous materials. An area of polymer photocatalysis that deserves special attention and could benefit from a combined computational and experimental effort, is indeed the physics and chemistry that underlie the electron–hole separation in heterostructures and the origin of their activity for the overall splitting of water.

Finally, I studied the optical properties of the three isomers of oligophenylene (and their main conformers) by submitting them to the same computational setup. I shed some light on the relationship between their molecular structure and their absorption and fluorescence energies. Firstly, both *ortho*- and *para*-phenylene are well behaved, to the extent that their absorption onsets decrease with oligomer length, whereas *meta*-phenylene shows no variation in absorption energies, due to "cross conjugation" leading to very localised excitations. Secondly, the three oligomers show very different fluorescence features: *para*-phenylene fluorescence energies unsurprisingly decrease with oligomer length, while for *meta*-phenylene, oligomer length has no influence, still due to cross-conjugation, but interestingly, fluorescence blue-shifts for *ortho*-phenylene, due to increasingly larger interphenylene torsion angles within its molecular backbone, in the excited state.

Computational tools prove to be of critical importance, especially when coupled to experimental techniques; both approaches must go hand-in-hand. They can offer invaluable insight into the molecular structure of materials, which cannot necessarily be accessed by measurement alone (when polymers are challenging to synthesise or characterise, e.g. insoluble, highly cross-linked polymers, which is often the case for materials presented in this thesis), but these computational methods, as attractive as they may be, do require some experimental validation to be tested and improved. The biggest challenge, as often in computational chemistry,

is striking the correct balance between computational cost, the ability to consistently calculate all the desired properties, and accuracy.

1. Liu, J.; Liu, Y.; Liu, N.; Han, Y.; Zhang, X.; Huang, H.; Lifshitz, Y.; Lee, S.-T.; Zhong, J.; Kang, Z., "Metal-free efficient photocatalyst for stable visible water splitting via a two-electron pathway", *Science* **2015**, *347*, 970.
2. Zhang, G.; Lan, Z.-A.; Lin, L.; Lin, S.; Wang, X., "Overall water splitting by Pt/g-C3N4 photocatalysts without using sacrificial agents", *Chemical Science* **2016**, *7*, 3062-3066.

Acknowledgements

I would like to express my sincere gratitude to my PhD supervisor, Martijn, for his availability, support, and guidance throughout my project, both on a technical and psychological level. I hugely benefited from his advice, key insights, and healthy dose of scepticism. Without him, many aspects of the work carried out in this thesis would have been impossible.

I would also like to thank my secondary supervisor, Furio, for his valuable comments especially at the beginning of my project, that helped me redefine part of the focus of my project, and how to best communicate my results.

I am grateful to all past and present members of the Zwijnenburg group. Enrico, with whom I shared many typical aspects of the PhD struggle, for taking me under his wing and helping me make sense of the arcane of quantum and computational chemistry, for the countless philosophical discussions we've had, and all the unforgettable moments spent together. Cristina, for her collaboration, her unwavering optimism and easygoingness, and her geek side to which I happily related. Milena, for stimulating discussions and mutual psychological support. Adriano, for his help and collaboration.

I am also grateful to the following UCL staff: Jörg, for his continuous technical help; Saïd for his friendliness and availability; Martin Vickers and Jeremy Cockcroft for happily helping me print posters at the last minute on several occasions.

I would like to thank all my collaborators at the University of Liverpool, especially Seb, Dave and Andy, from the experimental side, for working with us hand in hand, and for the interesting discussions that helped shape my project. With a special mention to Kim, now at Imperial's College, who broadened my perspectives by

giving me an opportunity to discover new codes, and to sharpen my Python skills. All the best for the future!

To Shereif, Yoshi and Yasmine. To Abdul, Maxime, Alberto, and Ester. To Linda, Larisa, and Pete. To Jürgen, Lucy, Ralph and Jane. To Garoui and Hugo. Thank you guys so much for all the awesome moments! You are the reason why I will never forget my London experience.

Last but not least, I would like to express my deepest gratitude to my love Stephanie, and to my parents Charles and Christine, for their unconditional love, and invaluable support. Thanks for believing in me when I felt helpless, for bearing with me, and for doing all you could to keep me motivated during those four years of ups and downs.

Pierre